

LIGHT SHEET MICROSCOPY FOR IMAGING CELLULAR FEATURES OF
UNSTAINED TISSUES

by

Jingwei Zhao

Copyright © Jingwei Zhao 2024

A Dissertation Submitted to the Faculty of the

JAMES C. WYANT COLLEGE OF OPTICAL SCIENCES

In Partial Fulfillment of the Requirements

For the Degree of

DOCTOR OF PHILOSOPHY

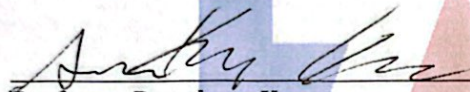
In the Graduate College

THE UNIVERSITY OF ARIZONA

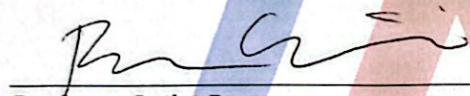
2024

THE UNIVERSITY OF ARIZONA
GRADUATE COLLEGE

As members of the Dissertation Committee, we certify that we have read the dissertation prepared by **Jingwei Zhao**, titled *Light Sheet Microscopy for Imaging Cellular Features of Unstained Tissues* and recommend that it be accepted as fulfilling the dissertation requirement for the Degree of Doctor of Philosophy.



Professor Dongkyun Kang Date: 4/19/24



Professor Leilei Peng Date: 4/19/24



Professor Travis W. Sawyer Date: 4/19/24

Final approval and acceptance of this dissertation is contingent upon the candidate's submission of the final copies of the dissertation to the Graduate College.

I hereby certify that I have read this dissertation prepared under my direction and recommend that it be accepted as fulfilling the dissertation requirement. ®



Professor Dongkyun Kang
Dissertation Committee Chair
Wyant College of Optical Sciences Date: 4/19/24

ACKNOWLEDGMENTS

Firstly and most importantly, I would like to thank my advisor, Dr. Dongkyun Kang. His incredible talent, selfless guidance, and unwavering support have changed my life in ways I never imagined. I deeply appreciate his generosity in sharing his knowledge, skills, and life philosophy whenever I needed it. His patience, kindness, and passion have influenced me to become a more empathetic, positive, and braver person. I will always remember his sense of humor, his hearty laugh, the invaluable conversations we had, and all the challenges we overcame together. It is my true privilege to have him as my advisor and mentor.

I would like to extend my gratitude to my dissertation committee members, Dr. Leilei Peng and Dr. Travis William Sawyer, for their invaluable time and guidance. In particular, I owe a special thanks to Dr. Leilei Peng for introducing me to Dr. Dongkyun Kang in my first year. Without her, I would have missed the opportunity to have such a wonderful mentor and advisor. I also thank Dr. Travis William Sawyer for being an inspiration to many students like me at the Wyant College of Optical Sciences. His talent and dedication to work continuously inspired me to become a better researcher.

I would like to thank our collaborators Dr. Eric Yang, Dr. Michelle Joanne Khan, and Dr. Brooke Liang at Stanford University for our wonderful teamwork on the project discussed in this dissertation. I am grateful for their great effort and passion in pushing

the project forward to help more people. Thank them for being patient and supportive collaborators who set the bar of collaboration so high.

I would like to thank our funding source, the National Institutes of Health (NIH), for the financial support for this project and my research assistantship. I am especially grateful for the funding opportunities provided for international students like me.

I would like to thank my previous and current lab mates Dr. Nachiket Kulkarni, Dr. Zhenye Li, Patrick O'Neal, Cheng Gong, Christopher Nguyen, Andrew Masciola, Raphael Osifeso, Momoka Sugimura, Kenneth Marcelino, Rafael Romero, Yongjun Kim, Paige Sawyers, Kayma Konecny, Alia May Nichols, Shirley Wang Xiang, Ameer Ghasem Nessae, and Maria Carmella Ocaya for their invaluable discussions and friendship. They made our Translational Optical Imaging lab a place of joy amidst the rigorous demands of research. More than colleagues, they have been my support system and mentors, guiding me to grow both personally and professionally. I will remember the games we played, the snacks we shared, the songs we sang, and the laughter we shared.

I would like to express my gratitude to all the faculty members and staff at the Wyant College of Optical Sciences for making the college an exceptional place for learning and research. Special thanks to Dr. Masud Mansuripur and Dr. Jim Schwiegerling for their amazing teaching in fundamental physics and math, for the opportunities to work with them as a teaching assistant, and for their support and guidance in my academic career. Additionally, I am thankful to Dr. Rongguang Liang for his generous life advice, and to his lab members for welcoming me into their social activities. Furthermore, my thanks extend to Jini Kandyil, Mark Rodriguez, and Dr. Brian P. Anderson for their administrative support over the years.

I would like to thank all my friends I met in Tucson, especially my best friends Yuanxin Guan and Shuyuan Guan. I am grateful for the times we studied, laughed, and cried together. Thank you for being there during the good times and the bad.

Finally, I would like to thank my boyfriend Shaobai Li for his continuous love, support, and care. Thank my cat Puck for her companionship and the comfort and joy she brought me. Thank my parents for their endless encouragement and unconditional love. Thank them all for giving me love and peace.

TABLE OF CONTENTS

LIST OF FIGURES	9
LIST OF TABLES	15
ABSTRACT	16
CHAPTER 1 Introduction	18
1.1 Motivation	18
1.2 Anal Cancer	22
1.2.1 Anatomy of Anal Cancer	22
1.2.2 Current Screening Methods for Anal Cancer	25
1.3 Clinically-viable <i>In Vivo</i> Microscopy	28
1.3.1 Reflectance Confocal Microscopy	29
1.3.2 Optical Coherence Tomography	33
1.4 Light Sheet Microscopy	37
1.4.1 Contrast Mechanism	38
1.4.2 Scattering-based Light Sheet Microscopy	39
1.4.3 Working Principle	40
1.4.4 Optical Design Consideration	41

CHAPTER 2 Investigation of different wavelengths for sLSM	55
2.1 Scope	56
2.2 Major Findings	56
2.3 Innovation and Contributions	57
CHAPTER 3 Speckle and Shadow Artifacts Reduction Method for sLSM	59
3.1 Method	60
3.1.1 <i>sLSM Setup</i>	60
3.1.2 <i>Performance Testing</i>	61
3.2 Results	63
3.2.1 <i>System Performance Test</i>	63
3.2.2 <i>Tissue Imaging Results</i>	63
3.3 Discussion	65
CHAPTER 4 Pilot Imaging Study	69
4.1 Scope	69
4.2 Major Findings	71
4.3 Innovation and Contributions	74
CHAPTER 5 Compact sLSM Probe	75
5.1 Method	75
5.1.1 <i>Compact sLSM Probe Design</i>	75
5.1.2 <i>Custom Objective Lens Design</i>	77
5.1.3 <i>Light Sheet Thickness Simulation</i>	79

	8
5.1.4	<i>Custom Objective Lens Performance Test</i> 80
5.1.5	<i>Probe Performance Test</i> 81
5.2	Results 82
5.2.1	<i>Compact sLSM Probe</i> 82
5.2.2	<i>Custom Objective Lens Performance</i> 83
5.2.3	<i>Probe Resolution Measurement</i> 85
5.3	Tissue Imaging Performance 85
5.4	Discussion 88
CHAPTER 6	Conclusion 92
6.1	Summary 92
6.2	Future Work 94
APPENDIX A	Investigation of different wavelengths for sLSM 96
APPENDIX B	Speckle and Shadow Artifacts Reduction Method 108
APPENDIX C	Custom sLSM Probe 111
APPENDIX D	Other Projects 116
REFERENCES 139

LIST OF FIGURES

1.1	Structure of the anal canal [28]	23
1.2	Schematic representation of squamous intraepithelial lesions (SIL) showing histological features of normal epithelium, LSIL with very mild to mild dysplasia, HSIL with moderate to severe dysplasia, and cancer. [29]	24
1.3	Schematic for DARE [30]	25
1.4	Low-grade and high-grade anal cytology [31]	26
1.5	Schematic of HRA [35]	28
1.6	Schematic of reflectance confocal microscopy	30
1.7	(A) Schematic of FCRM optical layout, (B) Photograph of the imaging probe, (C) Confocal image and corresponding H&E image of HSIL, scale bars are 20 μm in the confocal images and 50 μm in the H&E sections [39].	32
1.8	Schematic of OCT [40].	33
1.9	Schematic of (a) TD-OCT, (b) FD-OCT, specifically, the swept-source OCT.	35
1.10	Schematic of the line-field confocal OCT.	37

- 1.11 Schematic of different contrast mechanisms. For single-photon fluorescence excitation (a), molecules absorb photons with frequency ω_i and are excited to a higher electronic energy state. The molecules can return to the electronic ground state through a non-radiative transition and a radiative transition and emit fluorescence light (photons) at a frequency of ω_f . The emitted photons have lower energy and higher wavelength (redshift) than the excitation photons. For two-photon fluorescence (b), the molecules absorb two photons simultaneously, each having roughly half the energy required for single-photon excitation $\omega_i/2$, leading to two-photon fluorescence light that is blue-shifted relative to the incoming light. For light scattering (c), light with frequency ω_i excites the molecules to a virtual state, followed by a return to the ground state either through elastic light scattering (Rayleigh scattering) or inelastic scattering (Raman scattering). For Stokes Raman scattering, the emission light is red-shifted with the loss of energy, while for anti-Stokes Raman scattering, the emission light is blue-shifted with the gain of energy. For CARS (d), three photons from at least two distinct laser sources are involved. A pump photon at frequency ω_p raises the molecules from the ground state to a virtual state. The molecules then emit Stokes photons at frequency ω_s , while an additional photon from the probe beam ω_{pr} elevates the molecules to another higher virtual state. The final emitted photons have the frequency of ω_{as} . The emission light is blue-shifted compared to the incident light. [70] 39
- 1.12 Working principle of LSM. The illumination and detection paths are orthogonal to each other. [72] 40

1.13	Schematic of (a) Cylindrical lens [75], and (b)Key parameters to define light sheet illumination: light sheet length, light sheet width, and light sheet thickness.	42
1.14	Illustration of generating light sheet illumination with a cylindrical lens and a rectangular aperture. [26].	43
1.15	Schematic of Gaussian beam and Bessel beam generation by (a) a spherical lens and (b) a conical lens with the light intensity distribution plot on the focal plane. [79].	44
1.16	Schematic of open-top LSM using a water prism to hold immersion medium in place. The sample is loaded on top of the water prism. The illumination and detection paths are placed underneath the water prism[82].	47
1.17	Angular distributions of Rayleigh scattering and Mie scattering[84].	48
1.18	LSFM image of cultivated cell organoid of mouse intestine cells. Shadow artifacts are visualized as vertical dark lines along the light sheet incident direction. [86].	50
1.19	Schematic of different shadow reduction methods: multi-arm, beam pivoting, and Bessel beam illumination [88].	51
1.20	Image of speckle noise [95].	52

1.21	Speckle reduction method based on time-averaging of uncorrelated speckle patterns. (a) Moving diffuser: A static diffuser cannot reduce the speckle noise, but a moving diffuser is able to reduce the speckle noise. [100]. (b) Multimode fiber vibration: a piezoelectric vibrator is used to scramble the propagation modes of laser in the multimode fiber. As a result, the speckle is reduced when the vibrator is turned on. [102].	54
3.1	Schematic of the bench sLSM setup that can reduced the speckle and shadow artifacts (a) and the illumination path (b), and the workflow to determine the rectangular aperture size (c)	61
3.2	(a) Photo of the bench sLSM setup that can reduce the shadow and speckle artifacts, and (b) Measured axial resolution as a function of imaging depth	64
3.3	sLSM and H&E images of fixed human tissues: (a & b) Normal skin, (c & d) LSIL/Condyloma, (e & f) HSIL, and (g & h) Invasive SCC.	66
3.4	sLSM images of the normal skin acquired with the current sLSM setup (a), and the previous sLSM setup (b). Arrowheads: shadow artifacts	67
3.5	sLSM images of the normal skin acquired at NA of 0.065 (a) and 0.13 (b) along the x-axis. The shadow artifacts visible in (a), arrowheads, are not shown in (b)	68
4.1	(a) The clinical sLSM setup containing a bench sLSM, wide-field imaging module, specimen holder, and multi-axis stage housed in an enclosure, and (b) Schematic of the wide-field imaging module	70

4.2	sLSM and H&E images of normal fresh human biopsies. In the squamous zone (a & b), the cell nuclei are visualized as hyper-reflective round spots with uniform size and shape, the keratinizing layer is hyper-reflective at the top of the epithelial surface, and the dermal papillae are located at the bottom left corner. In the anal transition zone (c & d), nuclei are round with uniform size, shape, and distribution. In the colorectal zone (e & f), colonic glands are visualized as large tubular hyper-reflective structures in the stroma. The stroma is inflamed, characterized by numerous hyper-reflective, disorganized nuclei above the colonic glands. Scale bar: 50 μm . [111]	72
4.3	sLSM and H&E images of fresh anal LSIL. Scale bar: 50 μm . [111]	73
4.4	sLSM and H&E images of fresh anal HSIL. Scale bar: 50 μm . [111]	73
5.1	Schematic of the compact sLSM probe.	77
5.2	Schematic of the custom objective lens (a), wavefront error performance as a function of field (b), and wavefront error performance as a function of defocus (c).	78
5.3	Simulated Huygens PSFs and light sheet illumination for the on-axis field at the focus and at 103.1- μm defocus (a), and light sheet thickness for different fields and defocus locations (b).	79
5.4	Photo of the sLSM probe.	83
5.5	USAF target image (a), custom multi-pinhole target image (b), and measured resolution as a function of field (c) of the custom objective lens.	84

5.6	Custom resolution target image (a) and measured axial resolution as a function of depth (b).	85
5.7	sLSM images of normal anal squamous mucosa obtained with the compact sLSM probe (a, b) and bench sLSM device (c), and histologic image of the same tissue (d). arrows –nuclei.	87
5.8	sLSM images of LSIL obtained with the compact sLSM probe (a, b) and bench sLSM device (c), and histologic image of the same tissue (d).	87
5.9	sLSM images of HSIL obtained with the compact sLSM probe (a, b) and bench sLSM device (c), and histologic image of the same tissue (d). arrows –nuclei.	88
C.1	Custom objective lens performance: (a) MTF vs. spatial frequency. The cutoff frequency is set at the Nyquist frequency determined by the CMOS sensor, 588 cycles/mm; (b) Spot diagram for each field. Black circle: Airy disk.	113
C.2	Custom objective lens tolerance analysis setting	115
C.3	sLSM images of human finger tissues. Circles: sweat glands with helical pattern.	115

LIST OF TABLES

1.1	Refractive index values of different cervical neoplasia from the basal layer to the superficial layer.	46
3.1	Bill of materials for the bench sLSM probe that can reduce the speckle and shadow artifacts	65
5.1	Bill of materials for compact sLSM probe	84
C.1	Custom objective lens prescription (part 1)	112
C.2	Custom objective lens prescription (part 2)	113
C.3	Custom objective lens manufacturer tolerance table	114
C.4	Custom objective lens tolerance yield	114

ABSTRACT

The incidence of anal cancer has been increasing, with an average annual increase of 2.2% over 2010–2019. Anal cancer is predominantly related to Human Papillomavirus (HPV) infections. Recent studies have demonstrated the effectiveness of treating precancer in reducing the risk of anal cancer, highlighting the importance of early detection. However, high-resolution anoscopy (HRA), the current standard for anal cancer screening, has a steep learning curve and lacks widespread availability of skilled practitioners. Additionally, HRA-guided anal biopsies are associated with discomfort and potential complications for patients.

Scattering-based light sheet microscopy (sLSM) is an imaging technology capable of imaging unstained tissues with high resolution and a large field of view (FOV). This dissertation explores the potential of sLSM as an *in vivo* microscopy modality for enhancing anal cancer screening protocols. Through preliminary studies, we have laid the foundational research necessary for the development of sLSM in clinical settings. These investigations have focused on four topics: 1) optimizing the wavelength for sLSM imaging, 2) developing methods to reduce speckle and shadow artifacts, 3) conducting *ex vivo* imaging studies on fresh anal tissues with a bench sLSM setup to evaluate the feasibility of diagnosing anal precancer, and 4) developing a compact, handheld sLSM probe.

Chapter 2 focuses on the investigation of optimal wavelengths for sLSM, revealing that wavelengths around 600 nm strike a balance among imaging depth, resolution, speckle noise, and design complexity, thereby establishing a preferred parameter for sLSM development. In Chapter 3, a solution to reduce the speckle noise and shadow artifacts inherent in earlier sLSM setups is presented. By using a LED, slit, and rectangular aperture to generate the light sheet illumination, speckle noise and shadow artifacts are significantly reduced, resulting in enhanced image quality. Chapter 4 presents a pilot imaging study of fresh anal biopsies using a bench sLSM device. The clear visualization of morphological features distinguishing normal, benign, and precancerous tissues in sLSM images demonstrates the potential of sLSM for accurate anal cancer screening *in vivo*. Building upon this, Chapter 5 explores the feasibility of developing a compact sLSM probe. A custom objective lens design is presented that achieves high resolution, a large FOV, and small field curvature. The imaging performance of the compact probe is demonstrated by imaging fixed human tissues *ex vivo* and fresh human finger tissue *in vivo*, revealing the potential of sLSM technology for future clinical applications.

Chapter 1

Introduction

1.1 Motivation

In recent years, anal cancer incidence has been increasing rapidly, with an average annual increase of 2.2% over 2010–2019 [1]. This rise is predominantly attributed to infections with the Human Papillomavirus (HPV), which accounts for 80–85% of the anal cancer cases, particularly those linked to HPV16 [2]. Factors such as sexual behavior and weakened immune systems play crucial roles in increasing the risk of anal cancer, particularly affecting groups such as men who have sex with men, individuals living with Human Immunodeficiency Virus (HIV), and those with HPV-related gynecological conditions [3, 4, 5]. Squamous cell carcinoma (SCC) is the most common type of anal cancer, with the incidence at 131 per 100,000 person-years among HIV-positive homosexual men [5, 6]. The recent ANCHOR (Anal Cancer HSIL Outcomes Research) study has demonstrated a treatment of high-grade squamous intraepithelial lesion (HSIL), which is the precursor of the SCC, significantly reduces the risk of anal cancer [7].

Current screening techniques for detecting anal precancers include anal cytology and high-resolution anoscopy (HRA) [8]. Anal cytology, which incorporates the major components of cervical cancer cytology (“PAP smear”), has poor sensitivity and specificity for

detecting HSIL and is less reliable compared to cervical cytology [8]. Currently, the standard method for anal cancer screening is the HSA-guided biopsy [9]. However, there are a few challenges associated with HSA. The lack of trained practitioners and the steep learning curve limit the availability of HRA services and training opportunities [9]. In addition, the anal biopsy procedure is painful for the patients and could cause potential complications [10]. Therefore, there is a clear and unmet need to improve the anal cancer screening methods.

In vivo microscopy allows for direct examination of disease-associated cellular morphologic changes from the human tissue without removing the tissue from the patient [11]. Within the context of anal cancer screening, *in vivo* microscopy has the potential to accurately identify precancerous tissues during the HSA procedure and allow high-yield biopsies. This can lead to a reduction in the number of unnecessary biopsies of benign lesions and associated complications. Additionally, *in vivo* microscopy can serve as an educational tool by providing real-time feedback for HRA practitioners during training. Furthermore, the capability for comprehensive scanning of the anal canal using *in vivo* microscopy could improve and potentially complement the role of cytology. Moreover, *in vivo* microscopy could facilitate same-day treatment in low-resource settings (e.g., low- and middle-income countries, remote clinics) or for patients at a greater risk of being lost to follow-up.

Several *in vivo* microscopy technologies have been translated into clinically-viable medical devices in various clinical fields, including reflectance confocal microscopy in ophthalmology, dermatology, and gastroenterology [12, 13, 14], and optical coherence tomography (OCT) in ophthalmology, cardiology, and gastroenterology [15, 16]. However, most of the existing *in vivo* microscopy technologies have challenges in simultaneously achieving a high resolution and a large field of view (FOV). For example, the commercial reflectance confocal

microscopes for skin imaging have a high lateral ($1.25\ \mu\text{m}$) and axial resolution ($5\ \mu\text{m}$) [17] thanks to the use of a high-numerical aperture (NA) objective lens. However, its FOV is limited to $500 - 750\ \mu\text{m}$ [18, 19], which poses challenges in imaging the entire suspicious tissue region. On the other hand, OCT has a larger FOV, approximately $2 - 3\ \text{mm}$, but its resolution is around $10 - 20\ \mu\text{m}$, which is suitable for imaging architectural features rather than cellular and sub-cellular features [20, 21]. High-resolution, large-FOV OCT technologies have been recently developed [22, 23]. However, the use of an expensive broadband coherent light source likely increases the device cost.

Light sheet microscopy (LSM) is a microscopy technique that became popular in basic life science research [24]. LSM uses separate optical paths for illumination and detection, where the lateral resolution is determined by the detection optics, and the axial resolution by both the illumination and detection optics. Most of the previous LSM work was aimed to achieve a sub-cellular resolution, $< 1\ \mu\text{m}$ [25]. If the requirement for the LSM axial resolution could be relaxed to provide an axial resolution used for reflectance confocal microscopy, $\sim 5\ \mu\text{m}$, an illumination optics with a low NA (< 0.1) could be used. The low illumination NA in turn could generate a light sheet over a relatively large depth range, hundreds of μm . If the requirement for the lateral resolution of LSM could be relaxed to achieve a lateral resolution used for reflectance confocal microscopy, $1 - 2\ \mu\text{m}$, a detection objective lens with a moderate NA, ~ 0.3 could be used. The moderate-NA objective lens in turn would provide a FOV of several mm, comparable to a typical FOV of OCT.

Taking this approach of achieving a resolution comparable to the resolution of reflectance confocal microscopy while providing a large FOV, our research group previously demonstrated that LSM can be used to image cellular structures of unstained thick tissues using

intrinsic scattering contrast, which we termed scattering-based light sheet microscopy (sLSM) [26]. sLSM detects scattered light signals generated by the refractive index difference between certain sub-cellular/cellular components and their surroundings. In the previous experiment, sLSM was shown to visualize cellular details of thick, unstained animal tissues *ex vivo* with a high resolution (1.8 μm and 6.7 μm for the lateral and axial resolution, respectively) over a large FOV (~ 2.5 mm). Another potential advantage of sLSM is that the device cost can be low due to the use of a moderate-NA objective lens, an inexpensive light source such as a LED and superluminescent diode (sLED), and a standard complementary metal-oxide semiconductor (CMOS) sensor rather than an expensive scientific CMOS (sCMOS) sensor.

Although the previous experiment showed the potential of conducting cellular imaging with sLSM, the sLSM technology still needs further research and development before it can be tested for imaging human subjects *in vivo*. This dissertation mainly focused on four topics as the pilot study for *in vivo* sLSM applications: (1) Investigation of the optimal wavelength for sLSM; (2) Speckle and shadow artifacts reduction method for sLSM; (3) Fresh anal tissue imaging *ex vivo* and feasibility of anal malignancy diagnosis using sLSM; (4) Development of a handheld compact sLSM probe.

Chapter 1 is divided into three sections. The first section provided an overview of anal cancer regarding its anatomy and screening methods. The second section reviewed the current clinically-viable *in vivo* microscopy approaches, including reflectance confocal microscopy and OCT. The third section discussed the basic principle of LSM and sLSM, and several design considerations for designing sLSMs.

Chapter 2 covers the investigation of different wavelengths for sLSM. A bench multi-wavelength sLSM setup that facilitates the investigation of different wavelengths for sLSM imaging is presented. The key findings are discussed in this chapter.

Chapter 3 covers a speckle and shadow artifacts reduction method for sLSM. The illumination design to achieve reduced speckle and shadow artifacts is presented.

Chapter 4 covers the pilot *ex vivo* imaging study for fresh anal biopsy tissues. The sLSM system that was delivered to the clinical site at Stanford University is presented. The key features of different anal lesions in sLSM images are discussed. A reader study to assess the diagnostic accuracy of sLSM is also presented.

Chapter 5 covers the development of a compact sLSM probe. The imaging performance of the compact probe is compared with the bench setups.

Chapter 6 concludes the dissertation with a summary and potential future directions.

In addition to the sLSM project, I was involved in two other projects during my PhD program: 1) Deep learning-based denoising in high-speed portable reflectance confocal microscopy, and 2) Handheld cross-polarised microscope for imaging individual pigmented cells in human skin *in vivo*. Two first-author manuscripts were published and are included in the Appendix D.

1.2 Anal Cancer

1.2.1 Anatomy of Anal Cancer

Anal cancer occurs in the anal canal. The anal canal connects the rectum to the anal margin, typically measuring 2 - 4 cm in length, as shown in Fig. 1.1 [27]. The dentate line

marks the transition zone between squamous mucosa and columnar rectal mucosa. Cancers located above the dentate line tend to spread to the mesorectal, internal iliac, and obturator lymph nodes, while those found below the dentate line usually spread to the inguinal and external iliac lymph nodes [28].

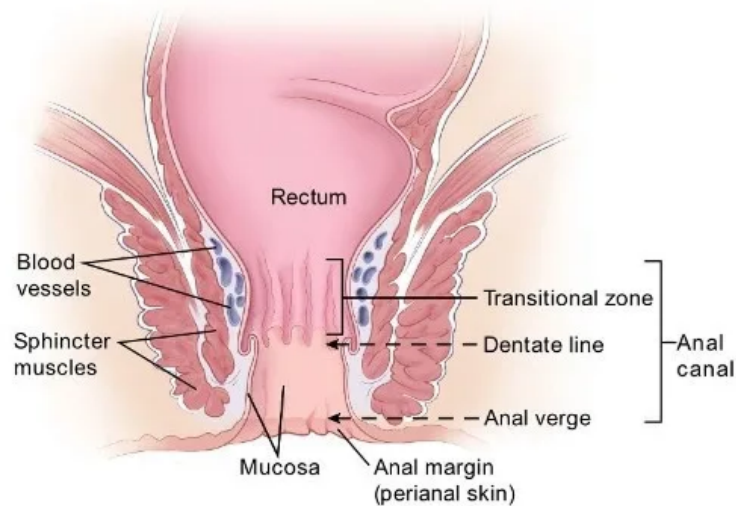


Figure 1.1: Structure of the anal canal [28]

Figure 1.2 illustrates the stepwise histological changes that occur in the development of anal SCC from normal epithelium to invasive carcinoma [29]. In normal anal epithelium, the squamous cells appear uniform and orderly. Low-grade squamous intraepithelial lesion (LSIL) shows mild cellular abnormalities including nuclear enlargement with variation in nuclear size, as well as an increase in the cytoplasmic area, starting from the lower part of the epithelium. HSIL characterized by larger, irregular nuclei and increased nuclear-to-cytoplasmic ratios, extend further up into the epithelium, sometimes involving the full thickness. For both LSIL and HSIL, the basement membrane remains intact, indicating that the lesion is not invasive yet. For SCC, the malignant cell growth disrupts the normal tissue

structure and infiltrates through the basement membrane into the stroma, leading to the formation of irregular masses or tumors that can grow and potentially spread to other parts of the body.

The treatment for different types of lesions depends on the severity of the disease. At-risk patients diagnosed with normal lesions or LSIL need regular follow-ups to monitor the progression of the disease while those with HSIL are treated by surgical excision, commonly performed using the loop electrosurgical excision procedure or destruction of the lesion through cryotherapy [10]. The treatment for patients diagnosed with SCC includes chemotherapy and radiation therapy. According to the recent ANCHOR study, treatment of HSIL can significantly reduce the risk of anal cancer [7]. Therefore, the early detection of HSIL is crucial to prevent the progression to invasive SCC.

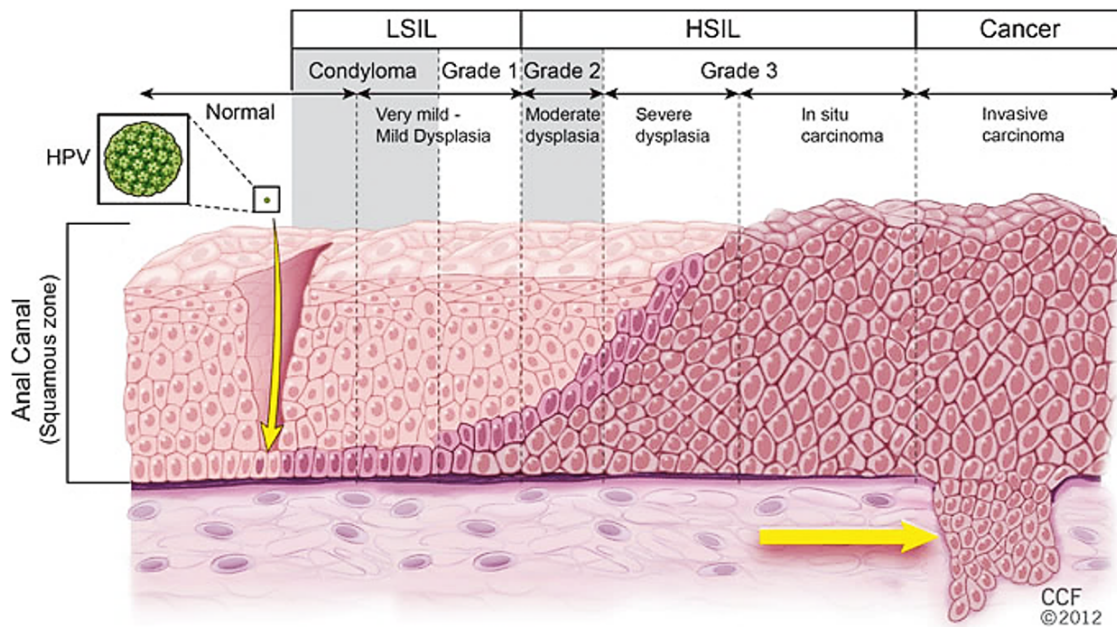


Figure 1.2: Schematic representation of squamous intraepithelial lesions (SIL) showing histological features of normal epithelium, LSIL with very mild to mild dysplasia, HSIL with moderate to severe dysplasia, and cancer. [29]

1.2.2 Current Screening Methods for Anal Cancer

Anal cancer screening primarily employs digital anal rectal examination, anal cytology, and HRA-guided biopsies.

Digital anal rectal examination is a simple clinical procedure to examine the lower rectum and anus [30]. This examination is performed using a lubricated, gloved finger (the "digital" part refers to the physician's finger) to assess the rectal wall for any abnormalities, masses, or tenderness, as shown in Fig. 1.3. It is mainly aimed at detecting cancers at an earlier stage or checking the recurrence after initial treatment, rather than detecting the cancer precursors (HSIL), mainly because of the obvious tumors indicating the presence of cancer [8, 30].

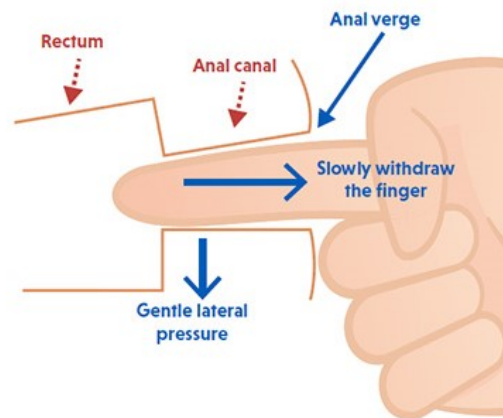


Figure 1.3: Schematic for DARE [30]

Anal cytology involves the collection of cellular material from the anal canal using a moistened polyester swab. The process, similar to cervical Pap smears, is performed by inserting the swab without lubrication into the anal canal, rotating it to collect cells, and then analyzing these cells under the Bethesda nomenclature [10]. An example of anal cytology is

shown in Fig. 1.4 [31]. Anal cytology alone is not reliable enough and is typically used as a preliminary screening tool to identify individuals who may require additional evaluation through HRA mainly due to its limited sensitivity and specificity for anal HSIL [8]. Schofield et al. found that when screening high-risk groups, cytology by itself failed to detect one-third of the histologic HSIL identified on biopsy among a group of 203 HIV-positive and 81 HIV-negative MSM [32].

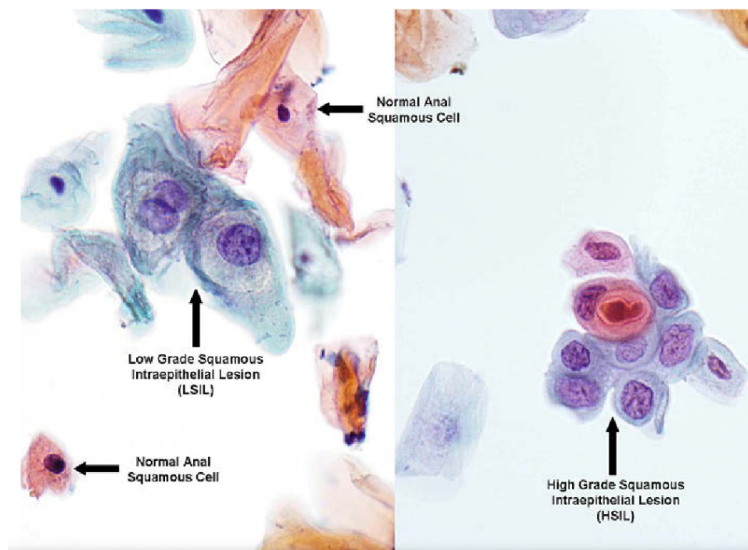


Figure 1.4: Low-grade and high-grade anal cytology [31]

HRA is a technique similar to colposcopy of the cervix, where an anoscopy and a high-powered magnifier are used for the visual inspection of the anal canal. An anoscope is a hollow tube that comes in either plastic or metal, as shown in Fig. 1.5. This tube is slightly larger in diameter than a finger and measures about 10-15mm in length. It is designed with an insert called an obturator, which facilitates the smooth insertion of the anoscope into the anal canal. During the HRA procedure, the anoscope is gently inserted into the patient's anal canal. Once the device is appropriately positioned, the obturator is removed, enabling the

doctor to view the interior surfaces directly. To enhance the visibility of the abnormal area, the anal mucosal surface can be stained with 5% acetic acid and/or Lugol's solution [10]. Acetic acid can temporarily whiten the diseased tissue due to the condensation of chromatin within the cell nuclei, which is known as acetowhitening. Precancerous and cancerous cells tend to have a higher nuclear-to-cytoplasmic ratio compared to normal cells. These abnormal cells produce a larger scatterer, leading to a more pronounced whitening effect. This contrast helps in identifying areas of potential HSIL against the normal epithelial tissue [33]. However, it's worth noting that acetowhitening is not specific to precancerous or cancerous lesions, and benign changes such as inflammation can also cause whitening. Lugol's solution, which contains iodine, can also stain the tissue due to the reaction between iodine and glycogen. Normal squamous epithelium stores glycogen, which absorbs the iodine, staining the tissue a dark brown [34]. In contrast, precancerous and cancerous cells, which are metabolically more active and less differentiated, contain less glycogen. As a result, these areas do not take up the iodine and appear pale or unstained against the dark background of the normal tissue. This stark contrast helps in delineating the margins of lesions and identifying potential HSIL or SCC. However, similar to acetic acid, Lugol's solution staining is not specific to HSIL and SCC. Therefore, in the context of screening of anal precursors, biopsies of suspicious lesions guided by HRA are performed for histological diagnosis. In the histology procedure, the biopsies undergo tissue fixation, processing, embedding, sectioning, and hematoxylin and eosin (H&E) staining to be visualized under a microscope. The diagnosis is conducted based on the cellular morphology illustrated in Fig. 1.2. Currently, the HRA-guided biopsy is the gold standard for the detection of anal HSIL. However, as mentioned in Section 1.1, due to

those limitations of HRA, there is a clear and unmet need to further improve the screening procedure.

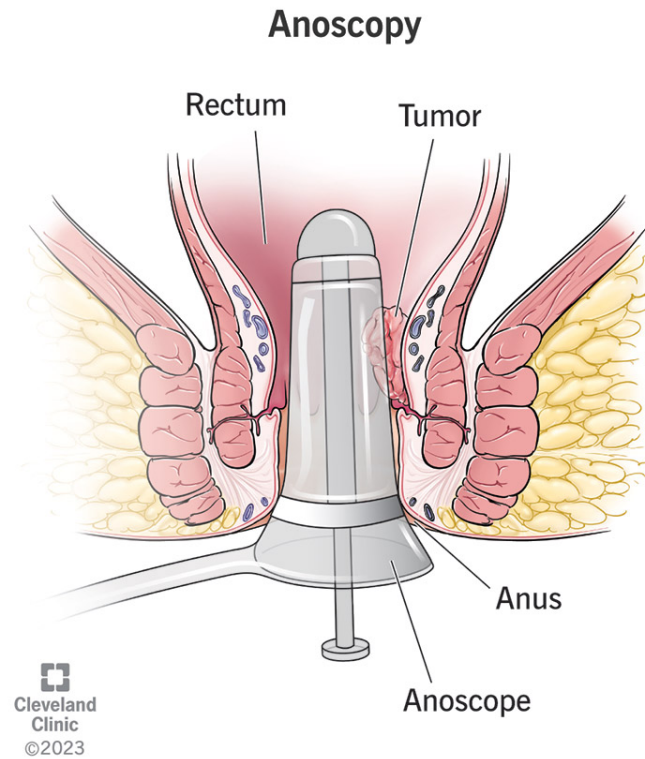


Figure 1.5: Schematic of HRA [35]

1.3 Clinically-viable *In Vivo* Microscopy

As for now, *in vivo* microscopy has yet been assessed for visualizing anal lesions. However, *in vivo* microscopy technologies have been effectively applied to the examination of cervical lesions, which share biological and histomorphological similarities with anal lesions.

1.3.1 Reflectance Confocal Microscopy

Reflectance confocal microscopy is an imaging technique that can image a thin section of thick tissues with high resolution. Figure 1.6 shows the optical layout of a typical reflectance confocal microscopy. Reflectance confocal microscopy typically contains two conjugate pinholes: one is used to generate a point light source, and the other is placed in front of the detector. The light from the point source is collimated, reflected by a beam splitter, and then focused by an objective lens onto the tissue. The backscattered light from different locations of the tissue is collected by the objective lens and focused on the detector. Without conjugate pinholes, light from out-of-focus planes would contribute to background noise and reduce image contrast. With the conjugate pinholes, the in-focus light can pass through the detection pinhole, while most of the out-of-focus light is rejected. As a result, the contrast of the image is improved. This capability, known as optical sectioning, enables the direct imaging of a thin layer of thick, unsectioned tissues with good contrast. In this configuration, the microscope acquires data from the sample on a point-by-point basis. To create a 2D image of the sample, a scanning mechanism, such as galvo mirror, is used to scan the light in lateral 2D dimensions.

For conventional microscopy, the optical resolution is characterized by the point spread function (PSF) in irradiance of the system. The lateral resolution can be defined as the lateral (perpendicular to the optical axis) full-width-half-maximum (FWHM) of the Airy disk at the focus, which is

$$r_{lateral} = 0.51 \frac{\lambda}{NA}, \quad (1.1)$$

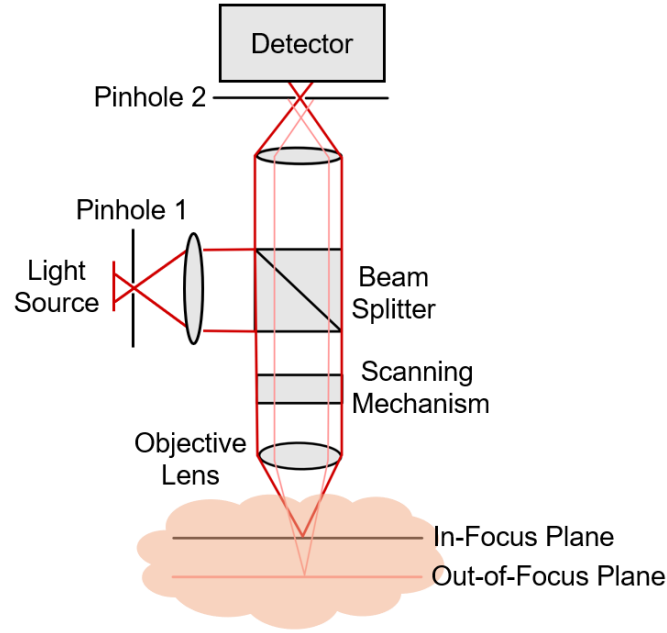


Figure 1.6: Schematic of reflectance confocal microscopy

assuming the system is diffraction-limited and has uniformly illuminated circular aperture. In this equation, NA is numerical aperture of the objective lens, and n is the refractive index in the object space. The axial resolution, on the other hand, is determined by the depth of focus, which is

$$r_{axial} = 2 \frac{n\lambda}{NA^2}. \quad (1.2)$$

For confocal microscopy, the resolution is characterized by the confocal PSF, which is obtained by multiplying the illumination PSF and detection PSF. As a result, the lateral and axial resolution of the reflectance confocal microscopy are [36]

$$r_{lateral,confocal} = 0.37 \frac{\lambda}{NA}, \quad (1.3)$$

and

$$r_{axial,confocal} = 1.52 \frac{n\lambda}{NA^2}. \quad (1.4)$$

To achieve subcellular resolution, confocal microscopes typically use large NA (> 0.5) objective lens.

In a study conducted by Collier et al., the utility of reflectance confocal microscopy for detecting cervical precancer in cervical biopsy samples was investigated [37]. In this research, the cellular morphologic and architectural features were first extracted from the confocal images by an automated segmentation algorithm, specifically focusing on features such as nuclear size, density, and shape. These features were then used to distinguish between normal biopsies and HSIL. The sensitivity and specificity of the method for distinguishing normal biopsies and HSIL was shown to be 100% with histopathological diagnosis serving as the gold standard. However, the quantitative feature distinctions between normal and LSIL and between LSIL and HSIL were not identified in this study due to the limited sample size. Another study conducted by Sheikhzadeh et al. also examined the capability of using confocal microscopy with an automated algorithm based on cellular morphology for cervical malignancy detection [38]. This study demonstrated high sensitivity (86–100%) and specificity (62–100%) in distinguishing HSIL from LSIL.

Reflectance confocal microendoscope were also developed for cervical precancer detection *in vivo*. Sung et al. developed a fiber optic confocal reflectance microscope (FCRM) with subcellular resolution and only 1.0 cm in diameter for examination of the cervix [39], as shown in figure 1.7. The cellular morphologic features visualized by FCRM aligned with the features visualized by histopathology.

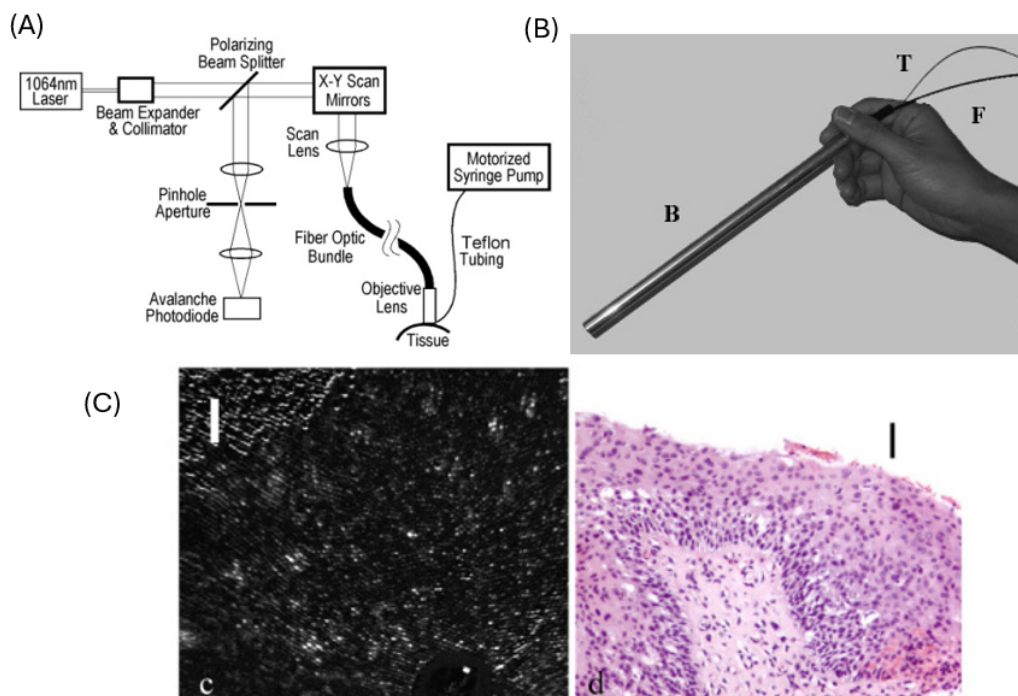


Figure 1.7: (A) Schematic of FCRM optical layout, (B) Photograph of the imaging probe, (C) Confocal image and corresponding H&E image of HSIL, scale bars are 20 μm in the confocal images and 50 μm in the H&E sections [39].

Although reflectance confocal microendoscopy is shown to be promising for *in vivo* imaging, several challenges exist. The limited FOV, as mentioned in Section 1.1, causes challenges in precisely targeting the suspicious lesions and increased time for comprehensive scanning of the large area of interest. Additionally, confocal microscopes typically produce *en face* images (i.e., images captured at a specific depth parallel to the tissue surface), whereas the standard histopathological evaluation of anal lesions involves assessing epithelial maturation across the tissue's thickness via cross-sectional views. Moreover, the device cost of reflectance confocal microscopy is high ($> \$65,000$) mainly due to the expensive scanning devices and their associated electrical components.

1.3.2 Optical Coherence Tomography

OCT is another *in vivo* imaging modality that employs low coherence interferometry to obtain detailed cross-sectional images of tissues. Figure 1.8 shows the basic principle of OCT [40]. In OCT, the light source has low temporal coherence, e.g., LED and supercontinuum laser. The light from the light source is divided into two arms, the reference and the sample arm. The reflected or backscattered light from the sample in the sample arm interferes with the light reflected from the reference arm. The interference signal is detected by a detector to analyze the depth information of the sample.

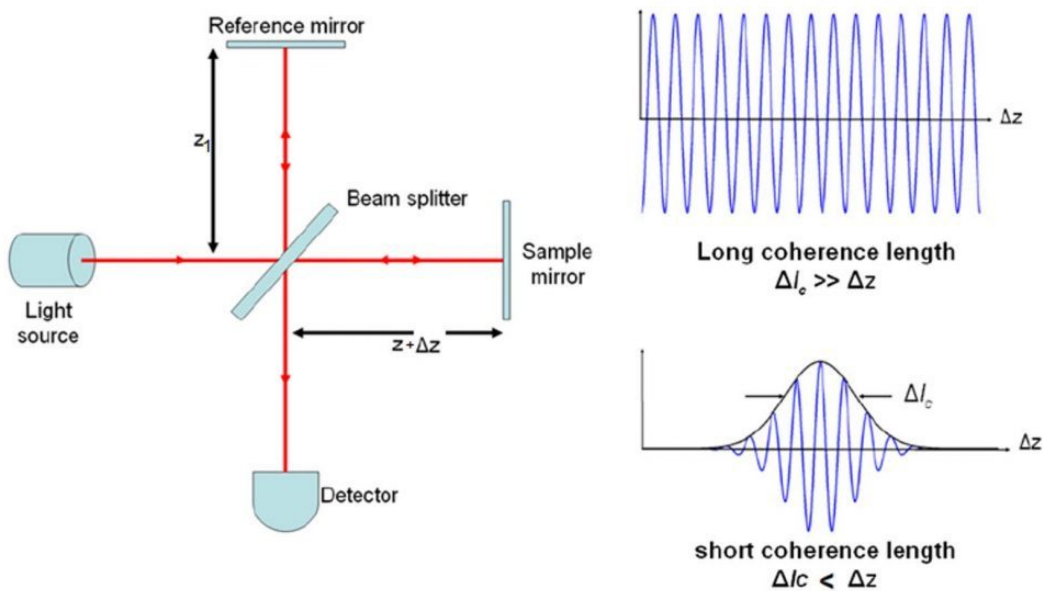


Figure 1.8: Schematic of OCT [40].

The fundamental theory behind OCT is similar to the white light interferometer. For a single wavelength within the source spectrum, the interference between the two arms generates periodic interference fringes across the space with a certain spatial period. The

detector can detect the interference signal at a certain location. Whether the detector detects bright and dark fringes depends on the optical path length difference between the two arms at the detector location. Different wavelengths generate different interference fringes with different spatial periods. The superposition of all interference fringes results in an interference pattern with varied fringe visibility across the space. Fringe visibility, quantified as the contrast of an interference pattern, is a measure of the difference in intensity between the bright and dark fringes relative to their average intensity, indicating the clarity and sharpness of the fringes. The interference pattern of the broadband light has an intensity distribution formed by an envelope and a periodic modulation over space. The location of the fringe with the highest visibility is at the location where the optical path difference between the two arms is zero. As the optical path difference between the two arms increases, the fringe visibility decreases. The FWHM of the envelope is determined by the temporal coherence length of the light source, which also determines the axial resolution of OCT. The temporal coherence length L_c of the light source is

$$l_c = k \frac{\lambda^2}{\Delta\lambda}, \quad (1.5)$$

where the coefficient k is determined by the spectrum shape of the light source.

OCT can be classified into two main categories: time-domain OCT (TD-OCT), and Fourier-domain OCT (FD-OCT). Figure 1.9 shows the difference between TD-OCT and FD-OCT. For TD-OCT, the depth information of the sample is axially measured by translating the reference mirror. This axial scanning is called A-scan. By scanning the detection path laterally with a scanning mirror, a 2D cross-sectional view of the tissue is obtained.

The lateral scanning is called B-scan. For FD-OCT, instead of scanning the reference mirror axially, it achieves the A-scan by scanning the wavelength over time (called Swept-source OCT) or by dispersion with a spectrometer (Spectral-domain OCT). For a single wavelength, the superposition of the interference fringes from all tissue depths is detected by the detector. Conducting Fourier transform on the detected signal as a function of wavelength (or wavenumber) can retrieve the depth information of the sample. The depth and the wavelength (or wavenumber) are two conjugate variables in the Fourier transform because the superposition of the interference fringes for different wavelengths at one depth and the superposition of the interference fringes for different depths at a single wavelength reveals the fringe visibility change as the optical path difference changes are two Fourier transform pairs.

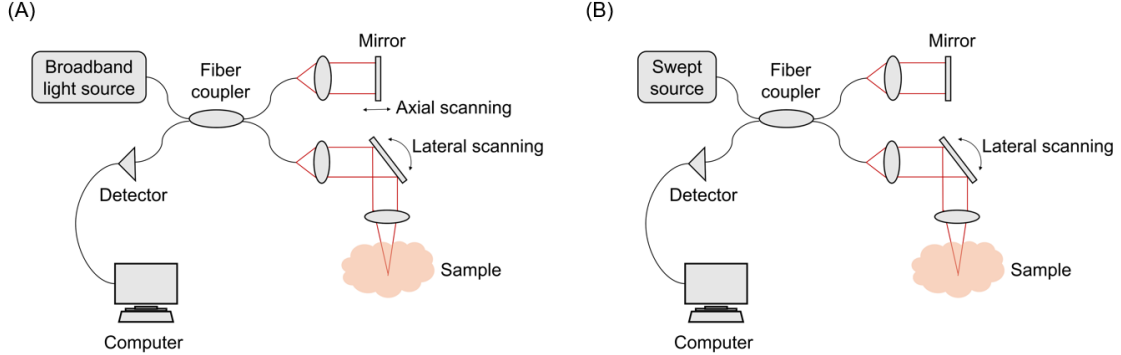


Figure 1.9: Schematic of (a) TD-OCT, (b) FD-OCT, specifically, the swept-source OCT.

Similar to conventional microscopy, the lateral resolution of OCT is determined by the NA of the objective lens,

$$r_{lateral,oct} = \sqrt{2 \ln 2} \frac{\lambda}{\pi NA} = 0.37 \frac{\lambda}{NA}, \quad (1.6)$$

assuming the beam is a Gaussian beam [41]. The axial resolution, however, only depends on the center wavelength and the bandwidth of the light source regardless of the objective lens NA,

$$r_{axial,oct} = \frac{2ln2}{\pi} \cdot \frac{\lambda^2}{\Delta\lambda}, \quad (1.7)$$

assuming the source spectrum is Gaussian [41]. As mentioned in Section 1.1, typical OCT has a large FOV but limited architectural resolution mainly because of the low-NA objective lens. Although high-NA objective lens can be used for OCT, it would result in a tightly focused beam with large divergence and tight depth of focus (DOF), as shown in Eq. 1.2, which limits the cross-sectional imaging of the tissue over a wide depth range [42]. One way to increase the depth range of OCT with a high-NA objective lens is to add additional axial scanning for the entire optics. For example, the line-field confocal OCT invented by Dubois et al. utilized this method to achieve high-resolution, large-FOV OCT imaging, as shown in Fig. 1.10 [43].

OCT has been successfully adapted to endoscopy devices and applied to various parts of the animal or human body for *in vivo* imaging, including cardiovascular system [44, 45], gastrointestinal system [46, 47, 48], lung [49], Urinary tract [50, 51], and cervix [52, 53, 54]. The sensitivity and specificity for detecting cervical precancers with OCT were studied: Gallwas et al. reported a moderate-to-high sensitivity (85–98%) and specificity (39 - 81%) [54] based on the qualitative assessment of the *in vivo* OCT images. Ma et al. reported a high sensitivity (86.7 ± 11.4 %) and specificity (93.5 ± 3.8 %) for distinguishing LSIL and HSIL using a quantitative computer-aided diagnosis method on *ex vivo* optical coherence microscopy images acquired [55].

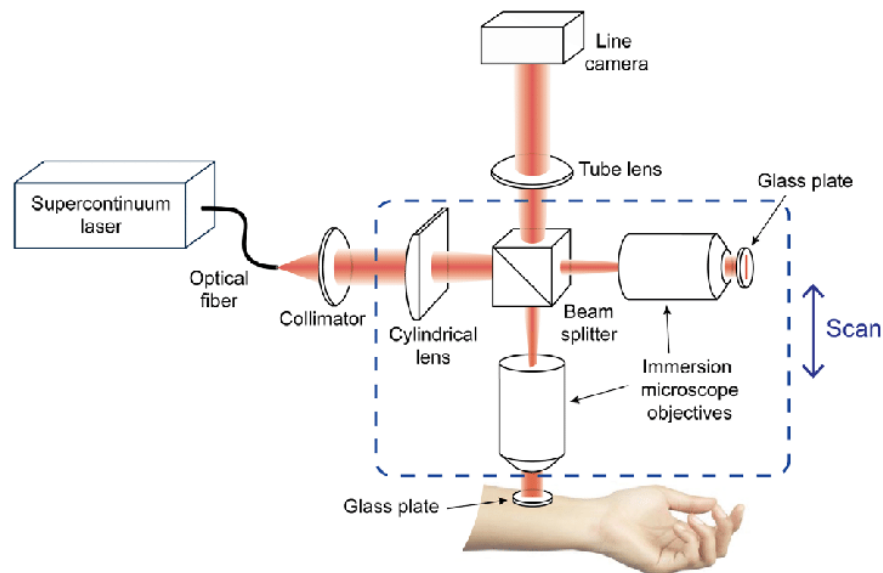


Figure 1.10: Schematic of the line-field confocal OCT.

The capability of diagnosing cervical cancer with OCT indicates the potential for expanding OCT into anal cancer screening. However, the main limitations of OCT are the limited resolution and high device cost, as mentioned in Section 1.1.

1.4 Light Sheet Microscopy

LSM is an imaging technique first introduced in 1902 by Siedentopf and Zsigmondy, termed ultramicroscopy, to visualize gold particles in colloidal gold solutions [56]. Despite this early invention, LSM did not gain significant traction until 1993 when Voie et al. introduced a light sheet microscope technique called orthogonal-plane fluorescence optical sectioning (OPFOS) to study the cochlea’s complex structure [57]. Later, the work about selective plane illumination microscopy (SPIM) by Huisken et al. published in *Science*, 2004 [58], further accelerated the advancements and widespread adoption of LSM techniques in biological research [59]. As the LSM technology evolved, various names and acronyms

emerged to describe systems operating on similar principles. In 2009, the terminology, LSM, particularly, light sheet fluorescence microscopy (LSFM), was eventually standardized by a group of researchers to describe this technology [60].

1.4.1 Contrast Mechanism

Several contrast mechanisms can be used for LSM, including single-photon fluorescence excitation [58, 61], two-photon and multi-photon fluorescence excitation [62, 63], second harmonic generation [64], inelastic scattering (Raman scattering) [65, 66], elastic scattering [67, 68, 26], and coherence anti-stokes Raman scattering (CARS) [69]. The difference between them is illustrated in Fig. 1.11. Currently, most of the LSMs are LSFM, which uses fluorescence excitation as the contrast mechanism. LSFM typically requires external fluorescent markers (fluorophores) to be introduced into the tissue, called fluorescence staining or labeling. Auto-fluorescence imaging, however, is a label-free fluorescence imaging technique that uses intrinsic fluorophores in the tissue. Fluorescence imaging has the challenges of photobleaching and phototoxicity. Photobleaching means the fluorophores become nonfluorescent over time because of the molecular structure altered by exposure to excitation light. Phototoxicity means the damage to biological tissues due to the interaction between cells and fluorescent dye and/or excitation light. Another consideration for LSFM is the signal strength, which is often low and requires sensors with high sensitivity and low noise, such as sCMOS.

Raman scattering, elastic scattering, CARS, and auto-fluorescence excitation all operate as label-free mechanisms and are capable for imaging unstained tissues. Within this group, elastic scattering uniquely does not require illumination at specific wavelengths specified

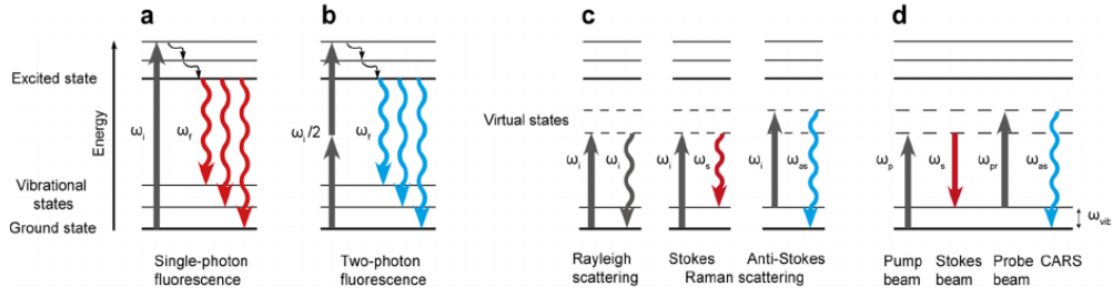


Figure 1.11: Schematic of different contrast mechanisms. For single-photon fluorescence excitation (a), molecules absorb photons with frequency ω_i and are excited to a higher electronic energy state. The molecules can return to the electronic ground state through a non-radiative transition and a radiative transition and emit fluorescence light (photons) at a frequency of ω_f . The emitted photons have lower energy and higher wavelength (redshift) than the excitation photons. For two-photon fluorescence (b), the molecules absorb two photons simultaneously, each having roughly half the energy required for single-photon excitation $\omega_i/2$, leading to two-photon fluorescence light that is blue-shifted relative to the incoming light. For light scattering (c), light with frequency ω_i excites the molecules to a virtual state, followed by a return to the ground state either through elastic light scattering (Rayleigh scattering) or inelastic scattering (Raman scattering). For Stokes Raman scattering, the emission light is red-shifted with the loss of energy, while for anti-Stokes Raman scattering, the emission light is blue-shifted with the gain of energy. For CARS (d), three photons from at least two distinct laser sources are involved. A pump photon at frequency ω_p raises the molecules from the ground state to a virtual state. The molecules then emit Stokes photons at frequency ω_s , while an additional photon from the probe beam ω_{pr} elevates the molecules to another higher virtual state. The final emitted photons have the frequency of ω_{as} . The emission light is blue-shifted compared to the incident light. [70]

to particular chemical compositions, and it generates a stronger signal than the others at equivalent levels of illumination. Therefore, sLSM provides better flexibility in selecting light sources and sensors, along with the possibility of being more cost-effective.

1.4.2 Scattering-based Light Sheet Microscopy

Previously, LSM based on elastic scattering has been demonstrated by several groups. In fact, the world first LSM setup, ultramicroscopy, was based on scattering contrast [56]. The imaging of plant roots [67], zebrafish embryos and tumor spheroids [68], and fibroblasts [71] has been demonstrated. Our group further demonstrated the capability of imaging

cellular features of thick, excised animal tissues *ex vivo* [26], which indicates the potential for imaging unstained human tissue *ex vivo* or *in vivo*.

1.4.3 Working Principle

The working principle of LSM is characterized by separate illumination and detection paths, as illustrated in Fig. 1.12 [72]. The illumination path generates a thin sheet of light, which selectively illuminates a thin section of the sample. The detection path captures images of the illuminated section from a perpendicular [26, 73] or oblique direction [74]. Since the illumination is primarily confined in the light sheet and conjugated to the detection focal plane, LSM offers the advantages of low out-of-focus background noise and reduced photodamage and stress to the living sample, meaning the LSM has good optical sectioning capability. This enables the imaging of thick tissues without the need for physical sectioning.

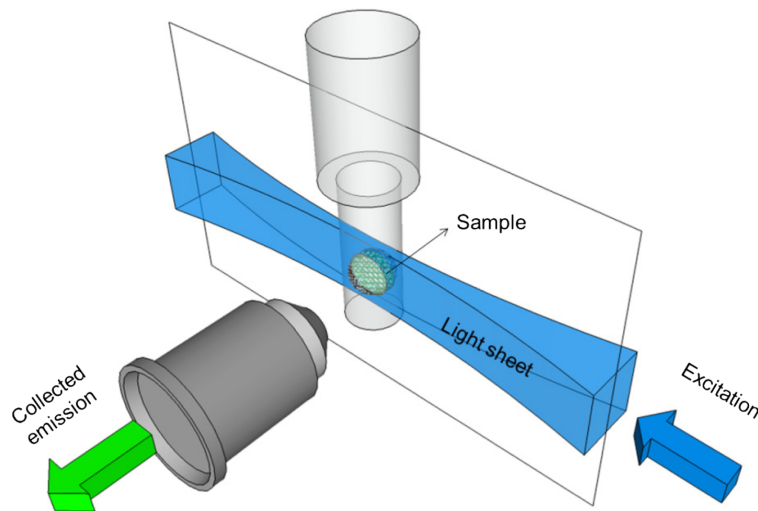


Figure 1.12: Working principle of LSM. The illumination and detection paths are orthogonal to each other. [72]

1.4.4 Optical Design Consideration

(1) Illumination and Detection Optics

In LSM, illumination optics involves more considerations. The most common way to generate light sheet illumination is using cylindrical lenses to focus a collimated laser beam, as shown in Fig. 1.13(a). The cylindrical lens only has power in one direction and focuses the collimated beam into a narrow plane. Three key parameters have to be clarified to describe the light sheet property. We named them: light sheet thickness, light sheet length (or light sheet DOF), and light sheet width, as shown in Fig. 1.13(b).

Light sheet thickness describes the optical sectioning capability of the LSM. Typically, it is defined as the FWHM of the beam's intensity distribution, measured along the direction perpendicular to the light sheet. At the cylindrical lens focus, light sheet thickness is

$$t = 0.44 \frac{\lambda}{NA}, \quad (1.8)$$

assuming the lens is diffraction-limited, and the incoming beam is a uniform rectangular beam. In this equation, NA is the numerical aperture of the cylindrical lens.

Light sheet length or DOF is defined as the range of the defocus that maintains the peak-to-valley (PV) wavefront error less than 0.25,

$$DOF = \frac{n\lambda}{NA^2}. \quad (1.9)$$

Within this range, the divergence of the beam is very small, and the light sheet thickness is approximately the same as the thickness at the illumination focal plane.

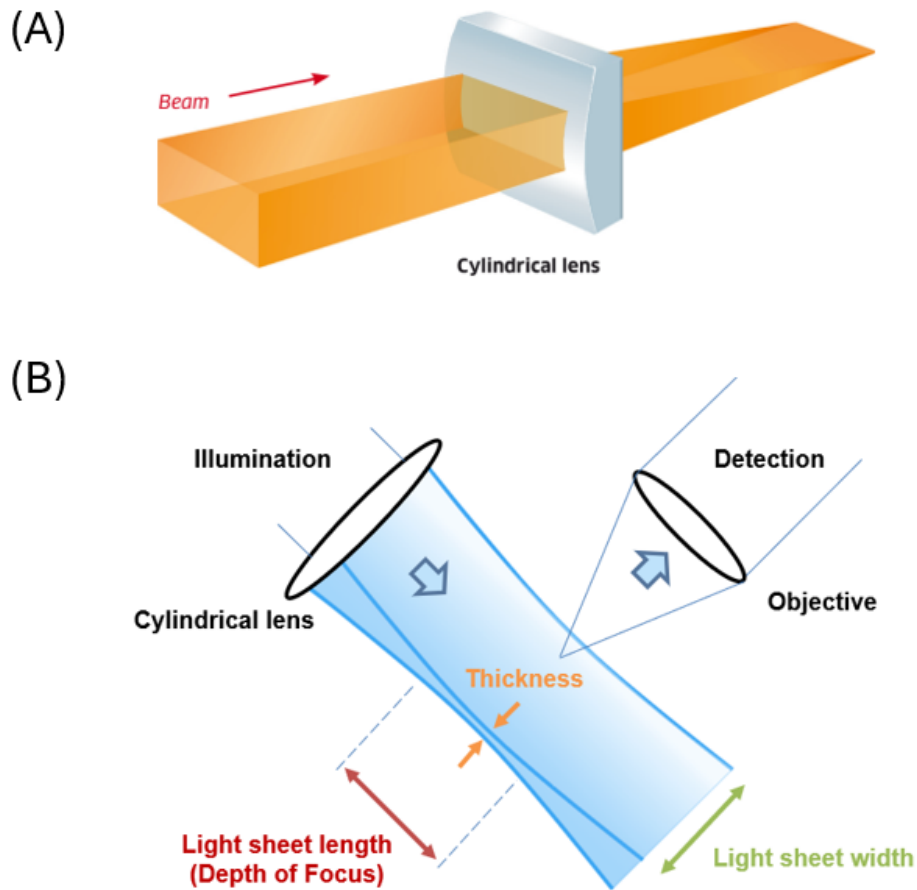


Figure 1.13: Schematic of (a) Cylindrical lens [75], and (b) Key parameters to define light sheet illumination: light sheet length, light sheet width, and light sheet thickness.

Light sheet width, measured along the illumination optical axis, determines the meaningful vertical FOV that has the desired optical sectioning capability. On the other hand, light sheet width, measured perpendicular to the optical axis along the plane of the light sheet, determines the lateral FOV that can be detected.

The lateral resolution of LSM is determined by the detection optics, and the axial resolution is given by the product of the illumination and detection PSFs. Therefore, the light sheet thickness and illumination NA affect the axial resolution. A larger NA results

in higher axial resolution. However, the increase in NA will result in a tighter DOF and a reduced vertical FOV. Thus, the illumination NA should be carefully chosen to balance the vertical FOV and axial resolution. Another tunable factor is the wavelength. A longer wavelength can provide a longer light sheet length than a shorter wavelength given the same illumination NA, but provides a thicker light sheet thickness and a lower axial resolution. When designing an LSM system, the illumination NA and wavelength should be carefully designed according to the application needs.

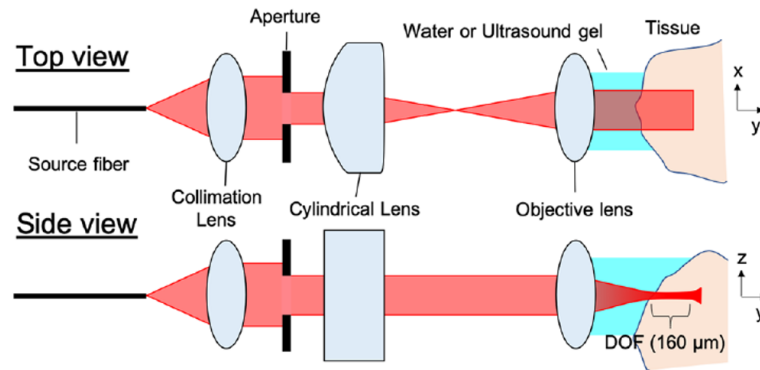


Figure 1.14: Illustration of generating light sheet illumination with a cylindrical lens and a rectangular aperture. [26].

One way to control the illumination NA is to use a rectangular aperture in front of the cylindrical lens to shape a collimated laser beam, as shown in Fig. 1.14 [26]. The dimensions of the rectangular aperture determine both the light sheet thickness and the light sheet width. Along the light sheet width direction, the rectangular aperture size directly determines the light sheet width since the beam is only truncated by the aperture but not focused along this

direction. Along the light sheet thickness direction, the rectangular aperture size determines the illumination NA.

Light sheet illumination can also be generated in other ways, such as beam scanning [76, 77] and Bessel beam [78]. The beam scanning method basically scans a focused beam in the lateral direction to generate a virtual light sheet. This method requires a scanning system, which complicates the system. Bessel beam is one type of shaped beam that has much longer DOF than a regularly focused Gaussian beam, as shown in Fig. 1.15 [79]. It is mainly a result of light interference, for example, the Bessel beam can be generated by a conical lens or an annular aperture [80]. However, the Bessel beam suffers from the strong sidelobe issue and increased out-of-focus background noise, as shown in Fig. 1.15.

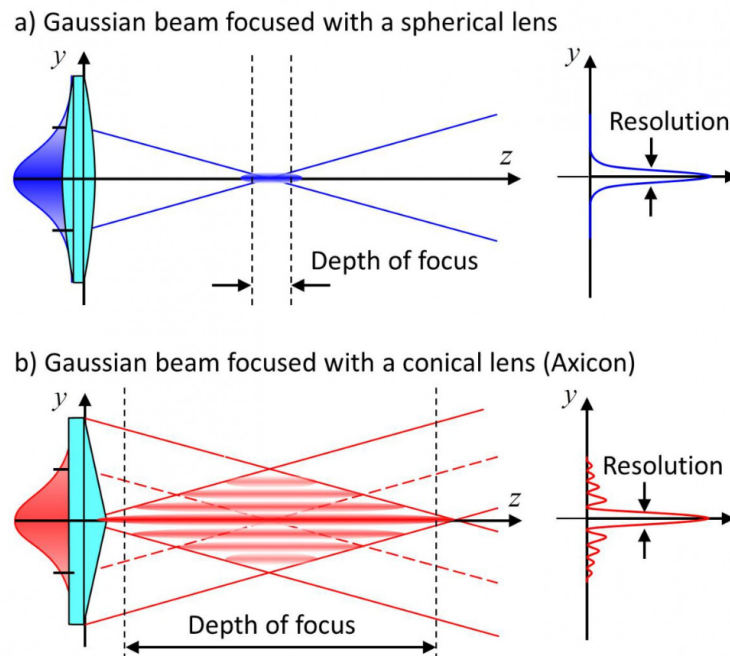


Figure 1.15: Schematic of Gaussian beam and Bessel beam generation by (a) a spherical lens and (b) a conical lens with the light intensity distribution plot on the focal plane. [79].

The detection design is rather simple, similar to a wide-field microscope. For a simple infinite-conjugate microscope design, the lateral resolution is given by Eq. 1.1. If the detection DOF, given by Eq. 1.2, is much larger than the light sheet thickness, the axial resolution would be mainly dominated by the illumination NA. Therefore, the detection NA of LSM can be relaxed to a moderate NA, ~ 0.3 , to achieve high axial and lateral resolutions and large FOV simultaneously.

To determine the minimal lateral and axial resolution requirements for an sLSM device to be used for *in vivo* clinical anal tissue imaging, the cell size and nuclear-to-nuclear distance needed to be taken into account. Anal tissues have similar nuclear morphologic features as cervical tissues. Typical cell nuclear diameter is 6-8 μm for the normal and precancerous cervical epithelia, and the nuclear-to-nuclear distance varies from 28 μm (normal) to 15 μm (Cervical intraepithelial neoplasia (CIN) stage 3 of HSIL) [38]. Considering the cell size, the lateral resolution should be $< 3 \mu\text{m}$ at least to resolve individual cells in LSM images, according to the meet Nyquist sampling theorem. Considering the nuclear-to-nuclear distance of CIN3, 15 μm , the axial resolution of 7.5 μm is expected to be sufficient to sample different layers of cells.

Index-matching should also be considered when designing an LSM for imaging human tissue. Index-matching serves to mitigate the reflection and aberrations caused by the refractive index difference between the sample and its surrounding medium. For human cervix mucosa, which shares similar structure and properties as the anal mucosa, was reported to have a refractive index of 1.37 – 1.43 [81], see Table 1.1. The refractive index of cervical tissues is close to the refractive index of water (1.33). Therefore, an objective lens designed for water immersion could be used for imaging human anal tissue with LSM. In addition,

materials like water or ultrasound gel should fill up the space between the objective lens and the tissue as the immersion medium to provide index-matching.

Table 1.1: Refractive index values of different cervical neoplasia from the basal layer to the superficial layer. The dysplastic cells in LSIL are confined to the basal one-third of the epithelium and gradually expand to the superficial layer as the condition progresses to HSIL. [81]

Cell type	Basal	Midzone	Superficial
Normal	1.387	1.372	1.414
Cancer	1.426	1.404	1.431

One concern associated with liquid immersion mediums is their viscosity. When a microscope using water as the immersion medium is positioned above the tissue, retaining water between the tissue and the objective lens becomes challenging, particularly when the lens has a long working distance. Additionally, the typical LSM, with its unique two path structure oriented at 90 degrees, presents a tightly constrained space between the detection and illumination objective lenses. This makes it more challenging to introduce index-matching material between the tissue and the LSM. To address this issue, McGorty et al. developed an open-top configuration to hold the immersion medium in place for LSM, as illustrated in Fig. 1.16 [82]. In this configuration, a water prism consisting of a glass container filled with water is developed. The sample is held on top of the water prism with the tissue surface facing downward. The LSM microscope is placed underneath the water prism. This unique structure allows the liquid immersion medium to be held stably. Ultrasound gel, unlike water, is a jelly-like substance and has higher viscosity. This feature makes it easier to apply and maintain in place between the microscope and the tissue. However, ultrasound gel tends to trap air bubbles within the optical path and introduce unwanted artifacts in the

images. Overall, effective mechanical control of the immersion medium is still a practical challenge that calls for more sophisticated engineering solutions.

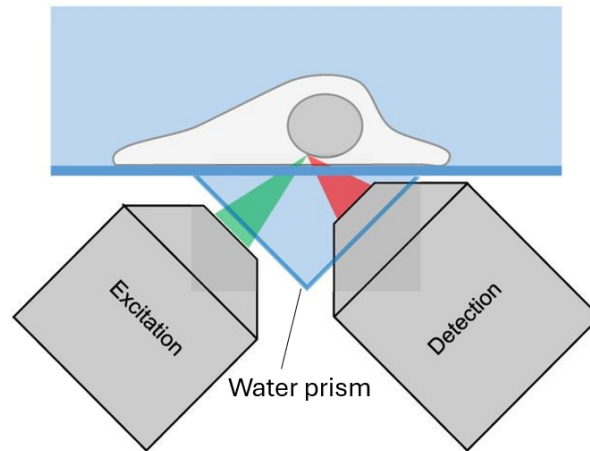


Figure 1.16: Schematic of open-top LSM using a water prism to hold immersion medium in place. The sample is loaded on top of the water prism. The illumination and detection paths are placed underneath the water prism[82].

(2) Scattering and Penetration Depth

The basic contrast mechanism of sLSM is elastic scattering, which includes Rayleigh scattering and Mie scattering [83, 84]. Rayleigh scattering occurs when light is elastically scattered by atomic and molecular particles much smaller than the wavelength of the incident light, typically less than one-tenth the wavelength. Mie scattering occurs when the scattering particles are about the same size as or larger than the light's wavelength.

Rayleigh scattering and Mie scattering have different angular distributions of the scattered light, as shown in Fig. 1.17 [84]. The probability of the scattered light at different directions (denoted by angle θ relative to the incident direction) determines the intensity angular distribution. For Rayleigh scattering, scattering at forward and backward directions

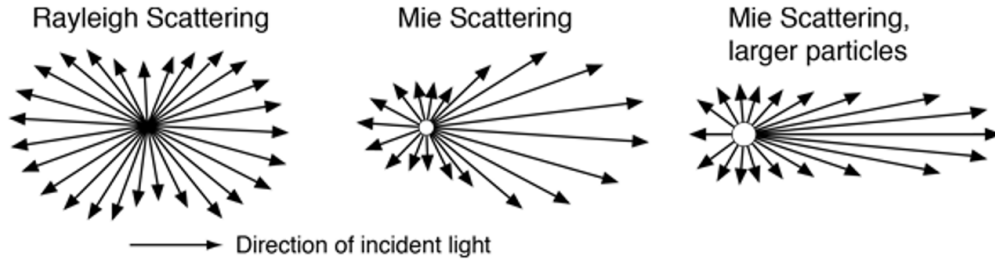


Figure 1.17: Angular distributions of Rayleigh scattering and Mie scattering[84].

are stronger than other directions, according to

$$I = I_0 \frac{8\pi N \alpha^2}{\lambda^4 R^2} (1 + \cos^2 \theta), \quad (1.10)$$

where I_0 is the intensity of the incident unpolarized light, R is the distance between the particle and the observer, N is the number of scatterers, and α is the molecular polarizability. The intensity is proportional to the fourth power of the inverse wavelength of the incident light, meaning a shorter wavelength has stronger scattering. Mie scattering is not strongly dependent on wavelength, and the mathematical description of Mie scattering is more complicated than Rayleigh scattering.

The scattering can be characterized by a coefficient, called reduced scattering coefficient μ'_s , in units of mm^{-1} . Considering the fact that not all scattering events significantly change their light propagation direction, the reduced scattering coefficient characterized the average travel distance of photons inside the medium before losing their original propagation directions after multiple scattering events. A smaller reduced scattering coefficient of a scattering medium results in a longer penetration depth of the light. When imaging thick tissues with scattering-based microscopes, the image contrast at a deeper region of the tissue is lower than

the superficial region mainly due to the multiple-scattering events. A mathematical model can be used to model the reduced scattering coefficient of a scattering medium containing both Rayleigh and Mie scattering [85],

$$\mu'_s(\lambda) = \mu_{ref} \left(f \left(\frac{\lambda}{\lambda_0} \right)^{-4} + (1 - f) \left(\frac{\lambda}{\lambda_0} \right)^{-\alpha} \right), \quad (1.11)$$

where μ'_{ref} is the reduced scattering coefficient at the reference wavelength ($\lambda_0 = 500$ nm), α is the Mie scattering coefficient, and f is the fraction of Rayleigh scattering. Therefore, a longer wavelength can provide a smaller reduced scattering coefficient and a larger imaging depth.

(3) Shadow Artifacts

Shadow artifacts, or stripe artifacts, are common issues in LSM that can degrade the image quality and make it challenging to appreciate cellular details. Shadow artifacts are visualized as dark stripes in the LSM images, as shown in Fig. 1.18 [86], caused by the straight light sheet being partially blocked or scattered by dense or highly scattering particles within the tissue along the light propagation direction. The presence of shadow artifacts especially poses challenges to extracting features of cancer precursors with computational segmentation algorithms.

Various methods have been developed to suppress shadow artifacts [87, 88, 89, 90]. The main concept is to increase the illumination angular diversity. Since the stripe artifacts are mainly caused by the lack of angular diversity of the light sheet on the light sheet plane, introducing additional light sheets with different inclination angles on the same plane can address the shadow artifacts. For example, multi-arm illumination can increase

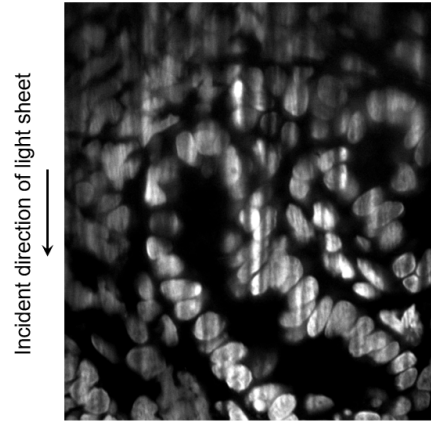


Figure 1.18: LSFM image of cultivated cell organoid of mouse intestine cells. Shadow artifacts are visualized as vertical dark lines along the light sheet incident direction. [86].

angular diversity by simultaneously deploying multiple illumination paths [91], while pivoting the illumination beam, achieved by a scanning system and temporally averaging, offers an alternative approach to increase the angular diversity [87], as shown in Fig. 1.19 [88]. The utilization of Bessel beams is another method to suppress the shadow artifacts mainly because Bessel beams are fundamentally achieved by interference of beams with different propagation direction. The limitation of multi-arm LSM is the increased complexity of the system and limited sample size that can be placed between different arms. The limitation of beam pivoting, in addition to the system complexity, is the increased acquisition time for scanning. As mentioned before, the Bessel beam has the sidelobe issue and reduced contrast.

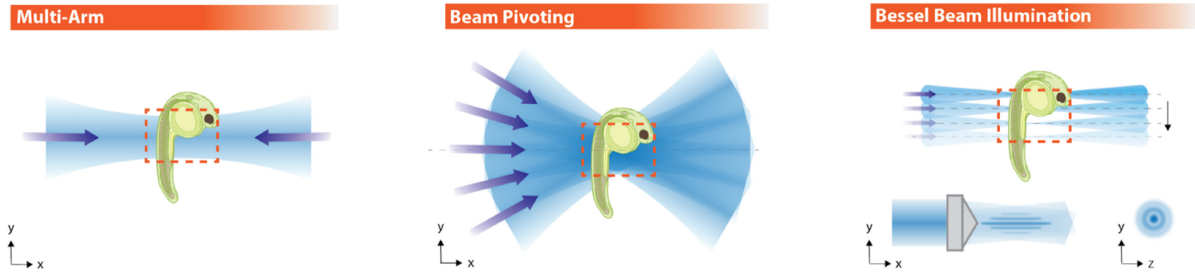


Figure 1.19: Schematic of different shadow reduction methods: multi-arm, beam pivoting, and Bessel beam illumination [88].

(4) Speckle Noise

Speckle noise is a common issue associated with microscopy technologies based on scattering signals [92, 93, 94]. Speckle noise is generated by the random interference of the coherent light when the light is scattered by rough objects or scattered medium [1]. It is observed as a high-contrast granular pattern and can significantly degrade the image quality and produce misleading information, as shown in Fig. 1.20 [95]. Laser is often used as the light source for microscopes given its high power and high spatial coherence. However, it suffers from strong speckle noise, especially for traditional single-wavelength lasers or narrow-band laser diodes. sLED has moderate-to-high coherence because of its high spatial coherence and low temporal coherence. Previously, speckle in the sLSM images with sLED as the light source is also obviously noticed [26]. LED is a relatively low-coherence light source due to its wide spectrum and large emission area. It is a potential light source to reduce the speckle noise for imaging scattering medium. However, LEDs have lower output power compared to lasers and sLEDs, and it is much more difficult to couple light from LEDs into low-throughput optics due to their high angular divergence and large emission area.

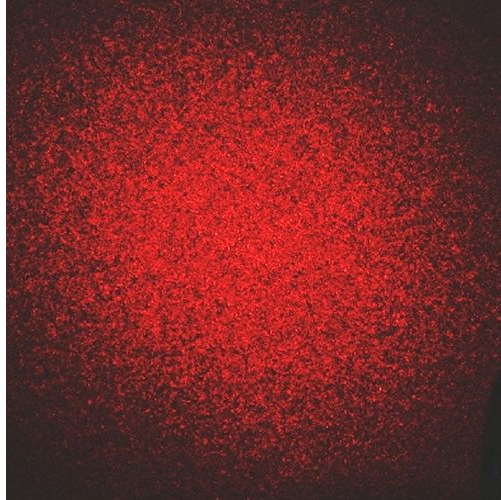


Figure 1.20: Image of speckle noise [95].

Speckle noise is quantitatively characterized by speckle contrast C and signal-to-noise ratio (SNR). Speckle contrast C is related to the light intensity I of a speckle pattern by the following equation, [96]

$$C = \frac{\sigma_I}{\bar{I}} = \frac{\sqrt{\overline{I^2} - \bar{I}^2}}{\bar{I}}, \quad (1.12)$$

where σ_I and \bar{I} are the standard deviation and mean value of I correspondingly. Contrast describes how strong the fluctuations of speckle intensity are compared with the average intensity. The value of contrast C is between 0 and 1. The signal-to-noise ratio of the speckle noise is defined in a reciprocal way

$$SNR = \frac{1}{C} = \frac{\bar{I}}{\sigma_I}, \quad (1.13)$$

For a fully developed speckle, both speckle noise contrast C and SNR are 1. Averaging N fully uncorrelated speckle patterns with equal mean intensities incoherently reduces the

speckle contrast, and the contrast can be expressed by

$$C = \frac{1}{\sqrt{N}}, \quad (1.14)$$

However, coherent additions of speckle patterns do not reduce the speckle contrast. The speckle reduction methods can be grouped into two categories: modifying the coherence property of the laser source, and time-averaging of the uncorrelated speckle patterns. For example, temporal coherence can be reduced by replacing the light source with a wider bandwidth, such as supercontinuum laser [94] or LED. Theoretically, for a scattering surface with a Gaussian shape of height fluctuation, the speckle contrast observed under illumination with a Gaussian-shape spectrum is given by [96]

$$C = \sqrt[4]{\frac{1}{1 + 8\pi^2 \left(\frac{\Delta\lambda}{\lambda}\right)^2 \left(\frac{\sigma_h}{\lambda}\right)^2}}, \quad (1.15)$$

where σ_h is the standard deviation of the rough surface height fluctuation, λ is the central wavelength, and $\Delta\lambda$ is the spectral bandwidth. For the same bandwidth, the spectral averaging of the speckle noise was less effective for light with longer central wavelengths. The spatial coherence of lasers can be reduced by modifying the structure of the laser [97] or using a laser array [98, 99]. In addition, commonly used time-averaging methods include moving diffuser [96, 100] and multimode fiber vibration [101, 102], as shown in Fig. 1.21.

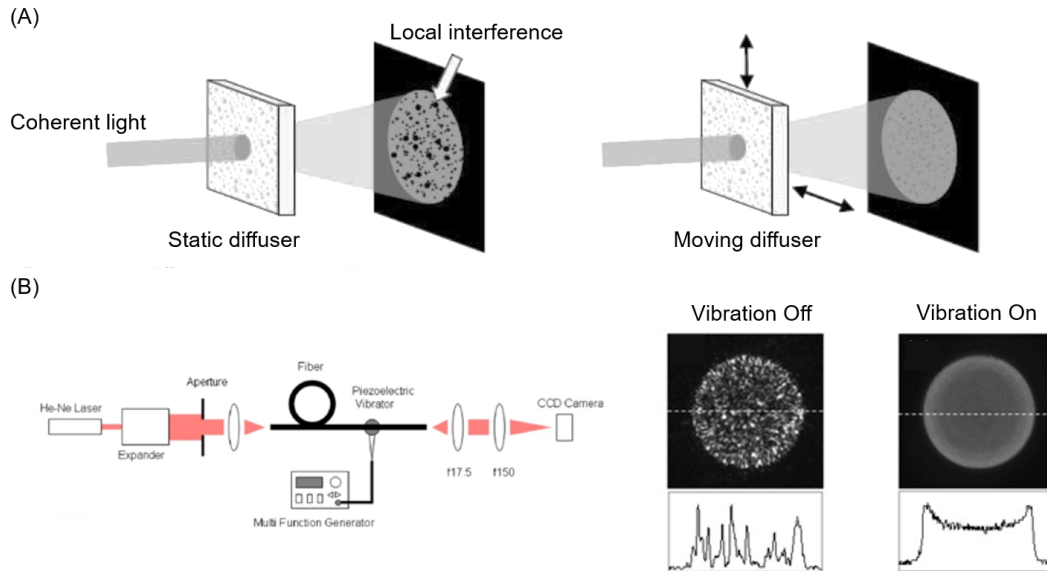


Figure 1.21: Speckle reduction method based on time-averaging of uncorrelated speckle patterns. (a) Moving diffuser: A static diffuser cannot reduce the speckle noise, but a moving diffuser is able to reduce the speckle noise. [100]. (b) Multimode fiber vibration: a piezoelectric vibrator is used to scramble the propagation modes of laser in the multimode fiber. As a result, the speckle is reduced when the vibrator is turned on. [102].

(5) Volumetric imaging

One additional advantage of LSM is the ability to simultaneously image a 2D cross-sectional plane of the tissue without scanning, which allows high-speed 2D imaging. For 3D volumetric imaging, it can be achieved by either translating the sample [73] or sweeping the illumination and detection focal plane optically [74]

Chapter 2

Investigation of different wavelengths for sLSM

The previous sLSM setup developed by our group [26] used a near-infrared spectrum around 834 nm because of its common use in reflectance confocal microscopy and OCT [103, 104]. However, there is a need to investigate the optimal wavelength for the specific tissue imaging application. For instance, a shorter wavelength can be used to achieve the same resolution with a lower NA than a longer wavelength. A low illumination NA can increase the light sheet length, and a low detection NA can make the detection objective lens design easier [105]. On the other hand, a longer wavelength is scattered less and therefore can provide a larger imaging depth. An sLSM setup that can image the same tissue location with several different wavelengths would facilitate the investigation of the optimal wavelength for the specific tissue type. Such a multi-wavelength sLSM setup needs to be carefully designed to allow for easy changes of the wavelength especially when each lens of the sLSM setup has its own chromatic focal shift. This chapter focused on the investigation of the optimal wavelength for sLSM in anal tissue imaging. The published manuscript can be found in Appendix A.

2.1 Scope

In this project, a multi-wavelength sLSM setup was developed that facilitates the investigation of different wavelengths for sLSM imaging. The investigated wavelengths varied from 500 nm to 800 nm with a 100 nm interval and 40 nm bandwidth. The system was carefully engineered to enable imaging of the same tissue region at different wavelengths with minimal adjustments required for switching wavelengths. A custom resolution target was designed to enable easy, quantitative measurement of the lateral and axial resolution for each wavelength as a function of imaging depth. Finally, we tested the system setup for imaging human tissues *ex vivo* with different wavelengths, and the imaging performance was evaluated quantitatively with an edge contrast metric and visually by a pathologist, Dr. Eric Yang from Stanford University. The published manuscript in Appendix A contains the details of the study method and the key findings [106].

2.2 Major Findings

Longer wavelengths provided a larger imaging depth based on both the quantitative image contrast evaluation and the visual assessment by a pathologist. This is not surprising because longer wavelengths experience less scattering. However, the amount of increase in the imaging depth was most notable between 500 and 600nm, and the increase was more moderate after 600 nm. The visual assessment results show that 600 nm allows for the visualization of cellular details up to a depth of $\sim 200 \mu\text{m}$, which can be useful in evaluating epithelial cellular morphologic changes in precancerous diseases. Therefore, a wavelength around 600 nm can be used for further development of a clinically-viable sLSM device. The

use of 600 nm, rather than a near-infrared wavelength around 800 nm, could either increase the light sheet length for the same axial resolution or improve the axial resolution for the same light sheet length.

2.3 Innovation and Contributions

The resolution target uniquely designed for LSM effectively simplified the measurement procedure of characterizing the optical performance of the LSM. The lateral and axial resolution of LSM can be simultaneously measured without the need for 3D scanning to get the PSFs, which is typically not the case for lateral and axial PSFs measurement with microspheres [107]. This property is more valuable for LSM than conventional microscopes. The axial resolution variation within the FOV for LSM is more significant than in conventional microscopes due to the defocus of the illumination. Thus, a comprehensive evaluation of axial resolution across the FOV is needed to characterize the LSM performance, and this custom resolution target makes the comprehensive evaluation easier to perform.

One of the interesting findings was that cellular morphologic details can be visualized from formalin-fixed tissues. This is helpful because the same tissue can be used over time to evaluate different imaging conditions and modalities. Furthermore, excised tissues are discarded in the pathology lab after clinical evaluation is complete, which can be formalin-fixed and stored for future imaging purposes. This is a rich source of tissue samples that are stable and readily available to the broader scientific community for optical image analysis. However, there is a caveat: fixed tissues might scatter differently than fresh tissues. The cell nuclear contrast of fresh animal tissues (hyper-reflective) [26], expected proxy of fresh human tissues, is opposite to the fixed human tissues (hypo-reflective). Evidence showed

that formalin-fixation changes the optical properties of human tissues, including absorption, scattering, and refractive index [108]. The mechanisms causing the changes include dehydration of the tissue [108], leakage of hemoglobin [108], and destroyed or altered cellular [109] and extracellular substances [110]. However, the mechanism that causes the contrast inversion still needs further investigation. A future study is needed to analyze the scattering signal and the visualized cellular details of tissues before and after formalin fixation.

Chapter 3

Speckle and Shadow Artifacts Reduction Method for sLSM

In the previous bench sLSM setups [26, 106], the sLSM images had noticeable speckle noise and shadow artifacts, which pose challenges in appreciating cellular details. As mentioned in Chapter 1.4.4, speckle noise is caused by the random interference of scattered coherent light and manifested as high-contrast random granular patterns. Shadow artifacts are dark stripes visualized in the sLSM images. Since cylindrical lenses produce on-axis light sheets that are collimated along the light sheet width direction, the objects underneath the optically dense structures are illuminated with reduced power. Increasing the angular diversity of the illumination on the light sheet plane would mitigate the shadow artifacts. In this project, we developed an sLSM bench setup that has reduced speckle noise and shadow artifacts. The setup used an LED as the light source and a slit to generate the illumination light sheet. The low coherence of the LED helped mitigate the speckle noise. The slit was incorporated with a carefully designed rectangular aperture to form the light sheet with increased angular diversity. The setup was tested with the same fixed-tissues used for the multi-wavelength sLSM setup that used a spatially-coherent light source and cylindrical lens for illumination. One conference paper was produced from this work, which is included in Appendix B.

3.1 Method

3.1.1 *sLSM Setup*

The schematic diagram LED-based sLSM setup is shown in Fig.3.1(a). Light from a high-power LED (center wavelength = 657 nm; bandwidth = 25 nm) was filtered by a slit (width = 5 μm ; length = 3 mm). The illumination light sheet was generated by imaging the slit onto the sample with two objective lenses: 5 \times objective (MUE12050; $f_1 = 40$ mm; NA = 0.15; dry) and 10 \times objective (MRH07120, Nikon; $f_2 = 20$ mm; NA = 0.3; water immersion), resulting in a magnification of 0.5. A 3D-printed rectangular aperture was placed in front of the second objective lens to form the illumination beam to a light sheet shape. The aperture length along the x-axis and width along the y-axis were set to 10.0 mm and 2.6 mm, respectively, to provide the illumination NA of 0.25 along the x-axis and 0.065 along the z-axis, as shown in Fig. 3.1 (b). This aperture arrangement resulted in an hourglass shape light sheet illumination with a theoretical thickness of 5.0 μm and DOF of 194.6 μm . The aperture size along the z-axis was iteratively determined by convolving the PSF of the illumination optics with the slit image and measuring the FWHM along the z-axis to control the light sheet thickness, as shown in Fig. 3.1(c). Because of the non-zero NA along the x-axis, each point of the tissue was illuminated with multiple angles on the xy-plane. Therefore, even when a bright particle is present in the tissue, it does not completely block the illumination light below the particle, which reduces the shadow artifacts.

In the detection path, a second objective lens (MRH07120, Nikon; $f_2 = 20$ mm; NA = 0.3; water immersion) collected the light scattered from the tissue. A camera lens ($f = 85$ mm; F2) focused light onto a monochromatic CMOS sensor (acA4024-29um, Basler;

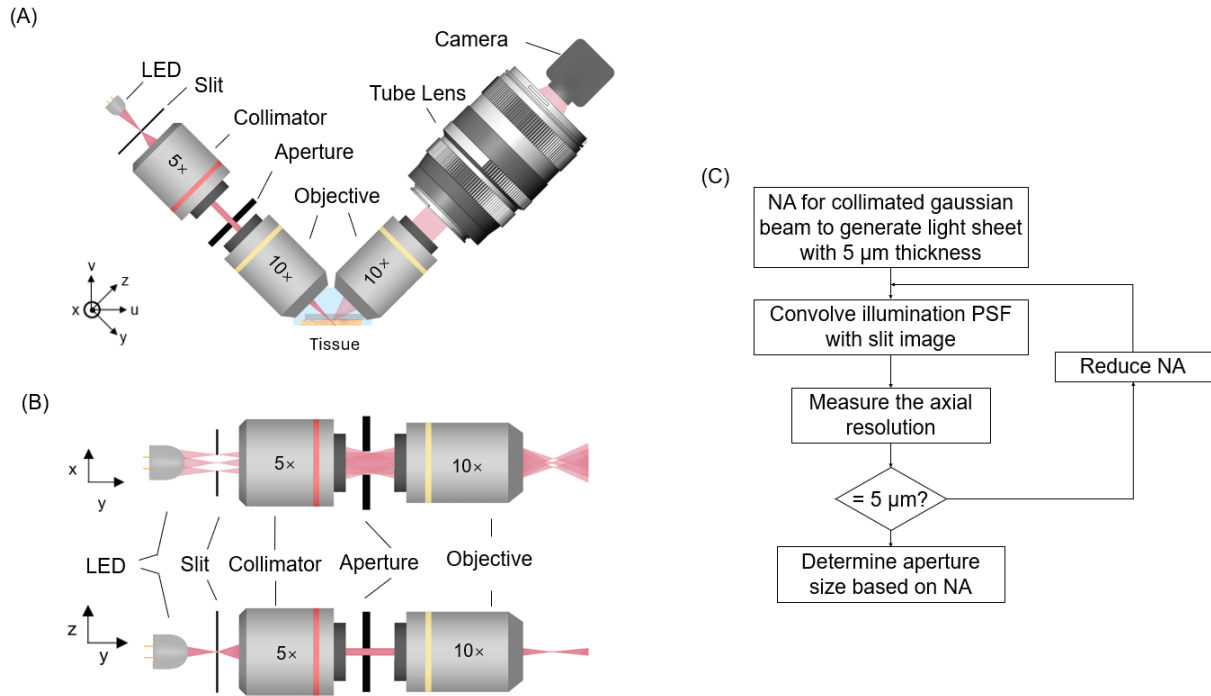


Figure 3.1: Schematic of the bench sLSM setup that can reduced the speckle and shadow artifacts (a) and the illumination path (b), and the workflow to determine the rectangular aperture size (c)

4,024×3,036 pixels; pixel size = 1.85 μm). The resulting pixel size in the tissue space was 0.44 μm , and the field of view was 1.5 mm.

3.1.2 Performance Testing

The lateral and axial resolution was measured by imaging the custom resolution target with a periodic line pattern (line width = 0.5 μm ; period = 30 μm) that we previously developed [106]. The resolution target was translated along the v-axis with a step size of 10 μm to measure the resolution at different imaging depths. The target was placed horizontally with the reflective lines parallel to the u-axis and facing upwards. The exposure time of the CMOS sensor was adaptively adjusted to avoid signal saturation. Index-matching

gel (GenTeal Tears Gel, Alcon, refractive index = 1.34) was placed between the resolution target and the probe as an immersion medium.

Tissue imaging performance was tested by imaging formalin-fixed human anal tissue *ex vivo*, including normal non-dysplasia, LSIL, HSIL, and SCC. The normal non-dysplasia tissue was the same tissue we previously used for investigating the optimal wavelength of sLSM [106]. The epithelial side of the tissue was placed upwards. A fluorinated ethylene propylene (FEP; refractive index = 1.34) film was placed on top of the tissue to flatten the tissue surface. Index-matching gel (GenTeal Tears Gel, Alcon, refractive index = 1.34) was used to fill the gaps between the objectives, the FEP film, and the tissue. The protocol for imaging formalin-fixed human anal tissues *ex vivo* was reviewed and approved by the Stanford University and University of Arizona Internal Review Boards (IRBs). Informed consent was waived by the IRBs for this study imaging discarded fixed tissues. Cellular features visualized in sLSM images were analyzed and compared to the features shown in the histologic images acquired from the same tissues. The assessment was done by an expert pathologist (Dr. Eric Yang at Standford University).

To validate the reduction of speckle and shadow artifacts, we compared the normal tissue images obtained with this setup and the previous setup (at 600 nm with 40 nm bandwidth). The speckle contrast of each image was measured according to Eq. 1.14. The speckle noise needed to be measured at regions where the pixel intensity is nearly uniform to avoid the intensity fluctuation caused by the tissue structure. Therefore, 30 rectangular windows (50×50 pixels, $22 \times 22 \mu\text{m}$) under an imaging depth of $200 \mu\text{m}$ were selected for the contrast measurement. The cellular details and tissue architectural structure were not clearly visualized in those windows due to the multiply scattering. The speckle contact was

evaluated for each window and was averaged to estimate the speckle contrast of the image. We assume the noise from other sources was negligible. Shadow artifacts were visually assessed. The effect of varying illumination NA along the x-axis on the shadow reduction was also assessed. We printed another square aperture with 2.6×2.6 mm in size, resulting in 0.065 NA in both illumination directions. Images were acquired with the rectangular aperture and the square aperture at the same tissue location to demonstrate the effect of shadow reduction with different angular diversity.

3.2 Results

3.2.1 System Performance Test

The sLSM bench device is shown in Fig. 3.2(a). The total material cost of the device was <\$5,000, as shown in Table 3.1. The illumination power on the tissue was $6.5 \mu\text{W}$, resulting in exposure time ~ 0.1 sec. The measured lateral resolution was $1.39 \pm 0.06 \mu\text{m}$. Within the theoretical DOF of $194.6 \mu\text{m}$, the axial resolution maintained smaller than $5.2 \mu\text{m}$, as shown in Fig. 3.2 (b).

3.2.2 Tissue Imaging Results

The sLSM images of formalin-fixed human anal tissues at different disease stages and their corresponding H&E images are shown in Fig. 3.3. In sLSM images, normal epithelium (Fig. 3.3(a)) shows a evenly-spaced honeycomb pattern of squamous epithelial cells. The intercellular borders are hyper-reflective (bright), and areas of cytoplasm and nuclei are hypo-reflective (dark). The dermal papillae are visible as large, dark, circular structures, similar to

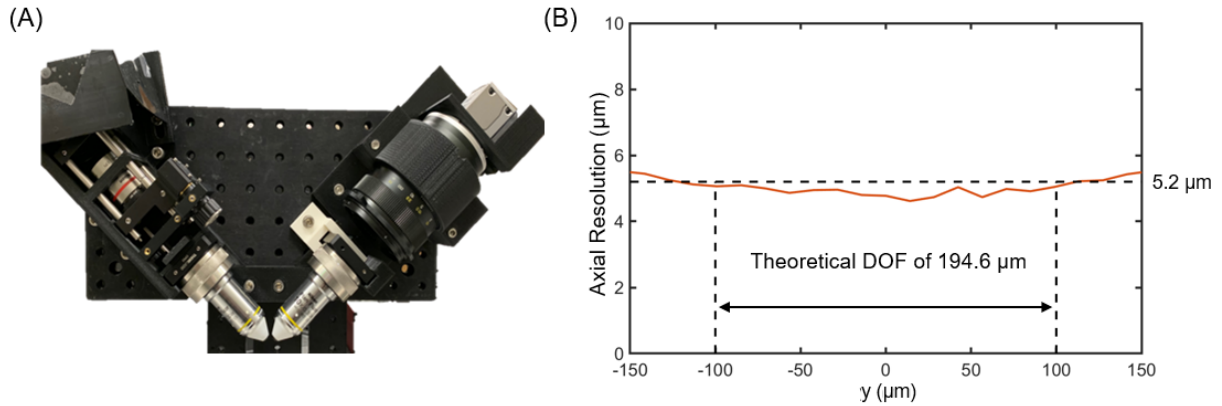


Figure 3.2: (a) Photo of the bench sLSM setup that can reduce the shadow and speckle artifacts, and (b) Measured axial resolution as a function of imaging depth

the H&E image (Fig. 3.3(b)). The image of LSIL (condyloma) (Fig. 3.3(c)) shows the clear distinction between the hyper/parakeratotic layer and the dysplastic epithelium beneath it. While a honeycomb pattern is retained in LSIL, the cells have more variability in the size and shape, reflecting the variation in cell nuclear size and distribution observed in the H&E image (Fig. 3.3(d)). HSIL image (Fig. 3.3(e)) loses the regular honeycomb pattern, which is replaced by a dense, irregular arrangement of dot-like hypo-reflective structures. The dense cell distribution is the key feature of HSIL that is observed in the H&E image (Fig. 3.3(f)). For SCC, similar to HSIL, the regular honeycomb pattern is also lost, but has greater variability in the arrangement and sizes of the dot-like hypo-reflective structures, reflecting a greater degree of nuclear pleomorphism, as shown in (Fig. 3.3(g) and (h)). The stromal invasion of SCC was not visualized due to the limited imaging depth ($\sim 100 - 200 \mu\text{m}$).

Regarding the improvements in speckle and shadow artifacts, a comparison between the current setup and the previous setup is shown in Fig. 3.4. It is clear that both speckle

Table 3.1: Bill of materials

Component	Cost (\$)
Slit	132.5
Nikon 5× objective	885.5
Nikon 10× objective (×2)	2374.2
LED	24.45
Camera lens	170
CMOS sensor	449
Mechanical mounts	639.7
CMOS sensor	199
3D printed materials	100
Total	4974.05

noise and shadow artifacts are reduced in the current setup. For the previous setup, the dark stripes are clearly visualized because there was nearly no illumination angular diversity on the light sheet plane. For the current setup, the Honeycomb pattern is more clearly visualized thanks to the reduction of shadow artifacts and speckle noise. The speckle contrast was reduced by 71% from 0.07 to 0.02 even though the light source bandwidth (25 nm) was narrower than the previous setup (40 nm). When the rectangular aperture was replaced by the square aperture, the dark stripes appeared again due to the reduced angular diversity (arrowheads in Fig. 3.5).

3.3 Discussion

In this project, we developed an sLSM bench setup to reduce the speckle noise and shadow artifacts. Preliminary images of formalin-fixed human anal tissues showed that the current sLSM setup significantly reduced the speckle noise and shadow artifacts compared

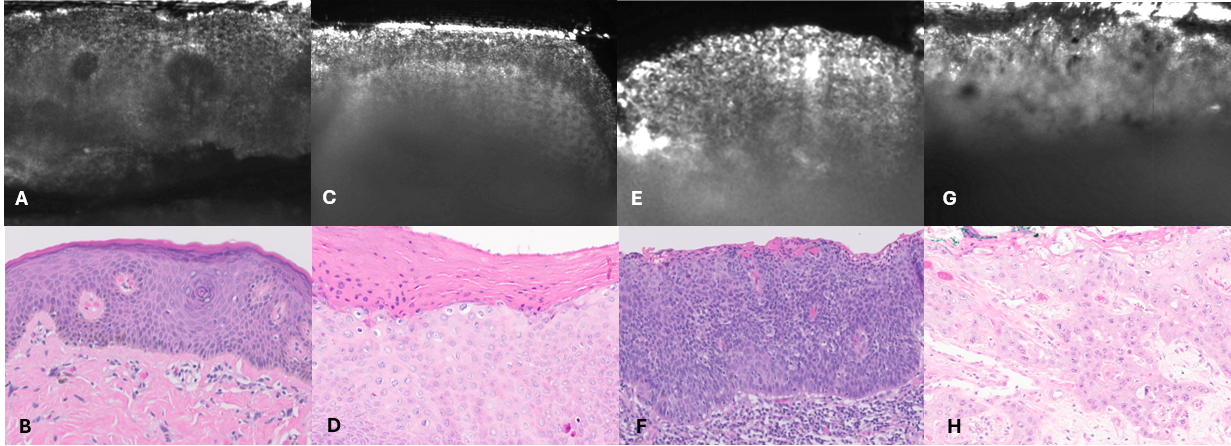


Figure 3.3: sLSM and H&E images of fixed human tissues: (a & b) Normal skin, (c & d) LSIL/Condyloma, (e & f) HSIL, and (g & h) Invasive SCC.

to the sLSM setup based on the laser and cylindrical lens. The cellular features were much easier to appreciate than before. The setup used low-coherence LED as the light source to reduce the speckle noise. The speckle contrast was reduced by 71%. The shadow artifacts were reduced by using a slit to generate the light sheet illumination. The slit was demagnified to form a line illumination at the focus, and the light sheet illumination profile was formed by controlling the size of a rectangular aperture. With a relatively high NA (0.13) along the light sheet width direction, the tissues were illuminated under a wide angular diversity, and thus the shadow artifacts were also reduced.

One challenge associated with this method is the low illumination power and the long exposure time (~ 0.1 msec). Even though we carefully chose an LED with a high output power, the radiance of the light source is still low compared to a laser or sLED. Since the throughput (étendue) of the system was also small, determined by the illumination area and subtended angle, the output power on the tissue was too low ($6.5 \mu\text{W}$) to allow real-time imaging.

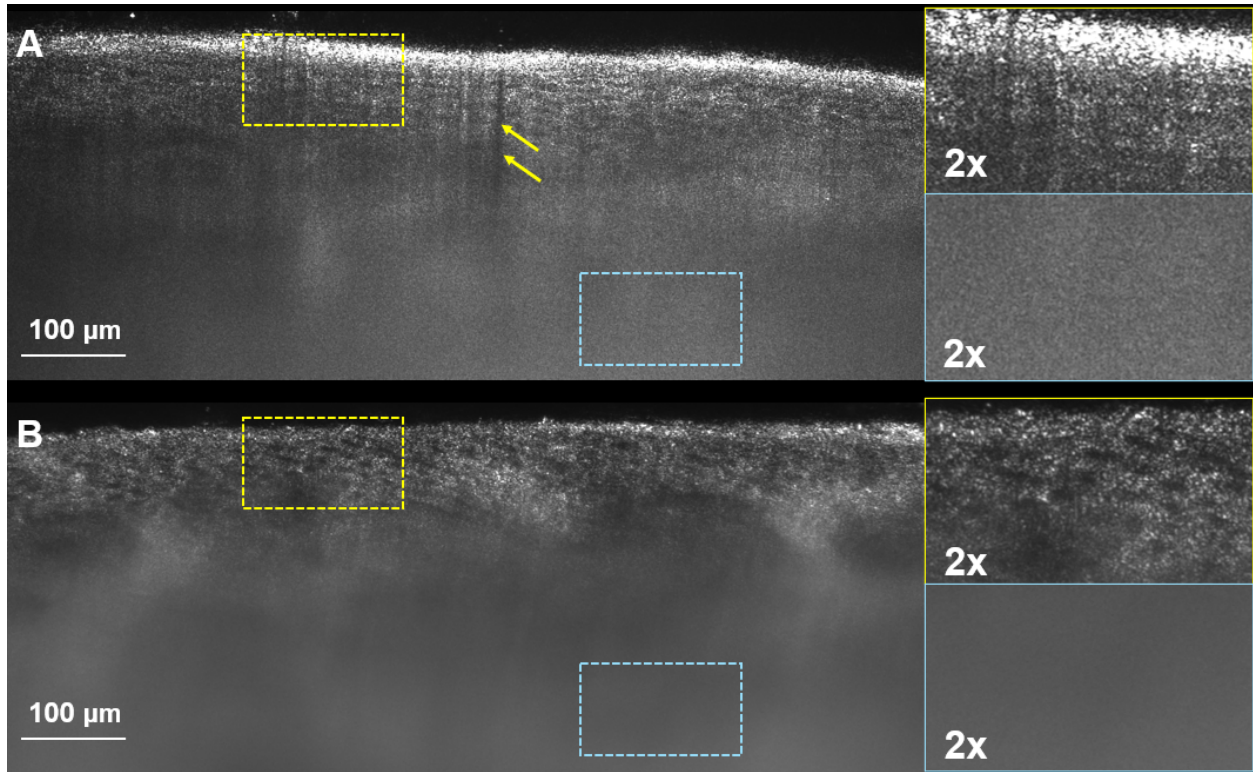


Figure 3.4: sLSM images of the normal skin acquired with the current sLSM setup (a), and the previous sLSM setup (b). Arrowheads: shadow artifacts

The sLSM images of the formalin-fixed human tissue clearly demonstrated the cellular morphologic distinctions among normal skin, LSIL, HSIL, and invasive SCC. The key features marking the progression of dysplasia visualized in sLSM matched those in histology images. Given these promising results, the next step is to validate the imaging capability of sLSM and its diagnostic potential for fresh anal tissues.

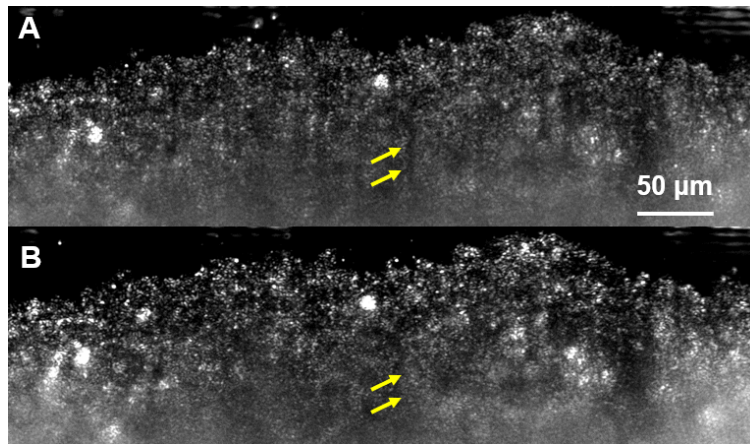


Figure 3.5: sLSM images of the normal skin acquired at NA of 0.065 (a) and 0.13 (b) along the x-axis. The shadow artifacts visible in (a), arrowheads, are not shown in (b)

Chapter 4

Pilot Imaging Study

Following our promising pilot study on imaging formalin-fixed human tissues, we conducted a prospective clinical study focused on imaging fresh anal biopsies. This was to establish a proof-of-principle demonstrating that our sLSM device can accurately replicate the diagnostic features of squamous dysplasia and thus serve as an effective tool for screening anal cancer. A manuscript was published containing the details of the study [111].

4.1 Scope

This project involves the development of an sLSM setup for a clinical imaging study. The sLSM setup development was performed at the University of Arizona. The clinical imaging study was performed at Stanford University.

The clinical setup consists of a bench sLSM, a wide-field imaging module, and a specimen holder, and a multi-axis stage, as shown in Fig. 4.1(a). The bench sLSM was the one presented in Chapter 3. The wide-field imaging module was placed underneath the specimen holder to image the entire specimen holder and help locate the region of interest. It consisted of two white LEDs to illuminate the specimen, a micro video lens, and a CMOS sensor, as shown in Fig. 4.1. The white LEDs were turned off during the sLSM data acquisition. The

specimen holder (CoverWell imaging chambers, Grace Bio-Labs; Diameter = 20 mm; Depth = 0.9, 1.7, or 2.5 mm) was mounted on the multi-axis stage. The stage had four degrees of freedom: a rotation around the v-axis, and translation along the x, v, and u-axis. The specimen location was manually adjusted by the rotation stage and the translation stages. The 3D volumetric imaging of the specimen was achieved by scanning the specimen holder with the motorized stage. The entire setup was housed inside an enclosure made of black acrylic sheets. The enclosure had dimensions of $58 \times 33 \times 28 \text{ cm}^3$. A software was developed in LabVIEW to control the imaging acquisition procedure.

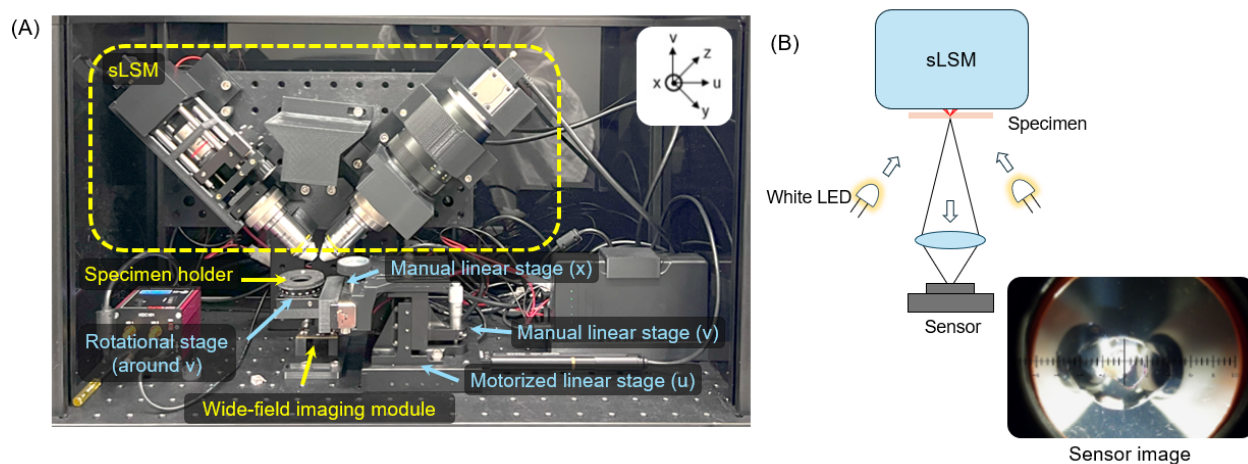


Figure 4.1: (a) The clinical sLSM setup containing a bench sLSM, wide-field imaging module, specimen holder, and multi-axis stage housed in an enclosure, and (b) Schematic of the wide-field imaging module

The clinical imaging study involved the biopsy imaging procedure, diagnostic accuracy reader study, and statistical analysis. The fresh anal biopsies were collected per routine clinic protocols. They were temporarily placed in 3-5% acetic acid to enhance the nuclear contrast and then imaged under the sLSM. The biopsies were then prepared for routine histopathology. The sLSM images were compared with the histology images to identify

the features for distinguishing among normal epithelium, LSIL, and HSIL. The diagnostic accuracy reader study involved 11 pathologists, who were trained with a training set first, and tested for the diagnostic accuracy. The statistical analysis was performed to analyze the diagnostic accuracy data.

In this project, my main contribution was the development of the clinical setup, with assistance from Yongjun Kim and guidance from Dr. Dongkyun Kang. The other authors of the manuscript [111] contributed to the clinical study.

4.2 Major Findings

A total of 3904 sLSM images of fresh anal biopsy tissue were acquired from a total of 110 anal biopsies of 31 patients. Final pathology reports revealed 27.2% of non-dysplastic, 36.4% of LSIL, and 36.4% of HSIL [111].

In sLSM images of fresh anal biopsies [111], the image contrast was contrary to the fixed tissues, as we expected. The cell nuclei were bright (hyper-reflective), while the cytoplasm was dark (hypo-reflective). The normal non-dysplastic tissues showed similar features as the H&E images (Fig. 4.2), e.g. the epithelium cells in the anal transformation zone epithelium had round cell nuclei with uniform size, shape, and distribution. For LSIL (Fig. 4.3), sLSM and H&E images both showed enlarged, variably sized cell nuclei in the superficial epithelial layers and decreased nuclear-to-cytoplasmic ratio of the cells in the superficial layer. What was uniquely observed in sLSM images for LSIL was the obvious hyper-reflective cytoplasmic borders, which were indistinct for normal tissue and LSIL. For HSIL (Fig. 4.4), the key feature was the significantly increased nuclear density. The cell nuclei were enlarged, unevenly sized, and spanning the full thickness of the epithelium.

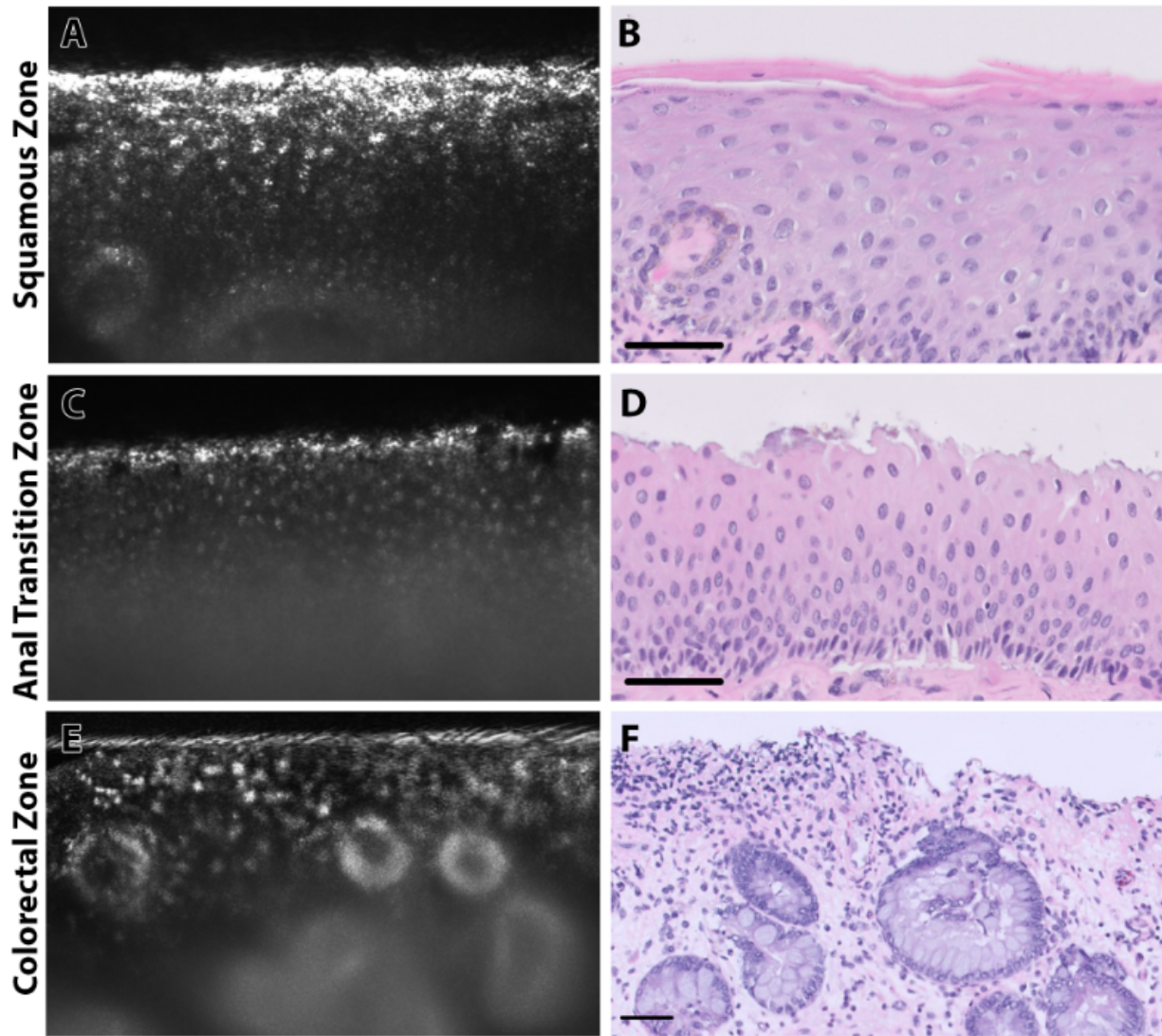


Figure 4.2: sLSM and H&E images of normal fresh human biopsies. In the squamous zone (a & b), the cell nuclei are visualized as hyper-reflective round spots with uniform size and shape, the keratinizing layer is hyper-reflective at the top of the epithelial surface, and the dermal papillae are located at the bottom left corner. In the anal transition zone (c & d), nuclei are round with uniform size, shape, and distribution. In the colorectal zone (e & f), colonic glands are visualized as large tubular hyper-reflective structures in the stroma. The stroma is inflamed, characterized by numerous hyper-reflective, disorganized nuclei above the colonic glands. Scale bar: 50 μm . [111]

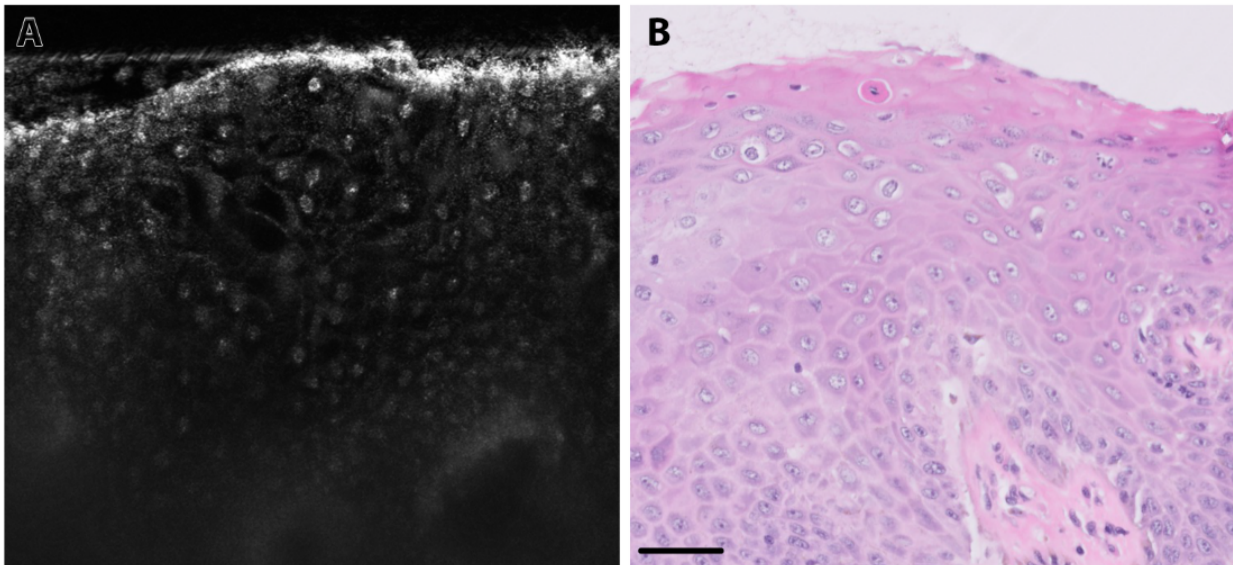


Figure 4.3: sLSM and H&E images of fresh anal LSIL. Scale bar: 50 μm . [111]

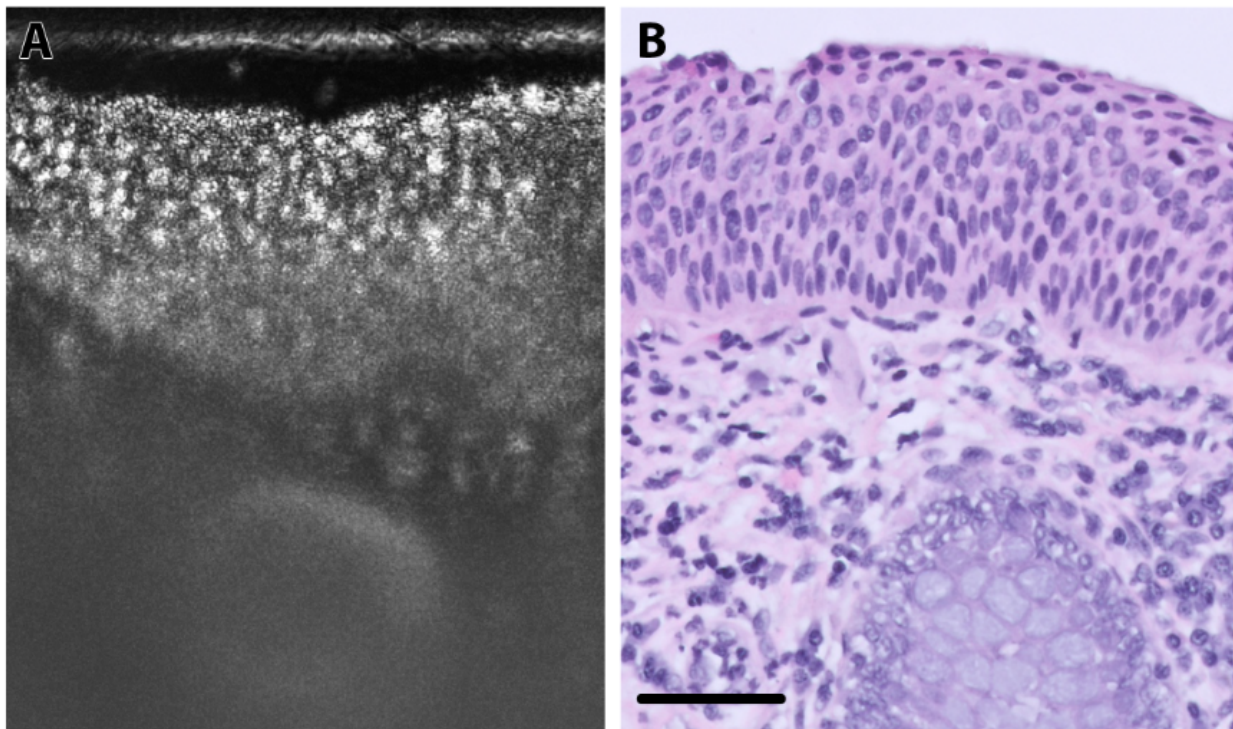


Figure 4.4: sLSM and H&E images of fresh anal HSIL. Scale bar: 50 μm . [111]

Regarding the diagnostic accuracy study [111],

1. The diagnostic accuracy for non-plastic images was significantly higher for H&E than for sLSM, 0.82 for sLSM versus 0.89 for H&E ($p = 0.021$).
2. The diagnostic accuracy for LSIL was significantly higher for sLSM than for H&E, 0.87 for sLSM versus 0.65 for H&E ($p = 0.020$).
3. The diagnostic accuracy for HSIL had no significant difference between sLSM and H&E, 0.91 for sLSM versus 0.85 for H&E ($p = 0.400$).
4. The overall diagnostic accuracy had no significant difference between sLSM and H&E, 0.87 for sLSM versus 0.80 for H&E ($p = 0.066$).

4.3 Innovation and Contributions

This project demonstrated that the key morphological features distinguishing among normal non-dysplasia, LSIL, and HSIL tissues were clearly visualized in sLSM images and were similar to those observed in corresponding the H&E images. sLSM gave a cross-section view of the tissue with a sub-cellular resolution, which is similar to the H&E images. This similarity in visual format eases the interpretation of sLSM images for pathologists, thus facilitating pathologists to analyze sLSM images for diagnosis. This study shows the great promise of sLSM for *ex vivo* pathological study and the potential for *in vivo* anal cancer screening applications. To our knowledge, we were the first ones to demonstrate the imaging capability of sLSM for fresh human tissues *ex vivo*.

Chapter 5

Compact sLSM Probe

The pilot study imaging fresh human anal biopsies *ex vivo* with the bench sLSM demonstrated promising diagnostic accuracy on the distinction of normal anal non-dysplasia, LSIL, and HSIL. The next important step is to evaluate the feasibility of developing a compact sLSM probe.

In this chapter, the design and development of a compact sLSM probe are presented. Instead of using an off-the-shelf objective lens, we developed a custom miniature objective lens to achieve high resolution, large field of view, and small field curvature. The optical performance of the custom objective lens and the compact sLSM probe were tested with standard and custom resolution targets. Tissue imaging performance was tested by imaging formalin-fixed human anal epithelial tissues *ex vivo*.

5.1 Method

5.1.1 Compact sLSM Probe Design

Figure 5.1 shows a schematic of the compact sLSM probe. In the illumination path, light from a laser (B073H21NJP, Sunshine electronics; wavelength = 638 nm; output power = 1.0 W) was coupled into a multimode fiber (02-511, Edmund optics; fiber diameter =

2.0 mm; core diameter = 1.96 mm; NA = 0.5). In between the laser and fiber, a rotating diffuser (DG10-1500, Thorlabs; grit = 1500; rotation speed = 600 rpm) was used to reduce the speckle noise. Light from the distal end of the fiber passed through an illumination slit (2-2.5-3+HS+M-0.5, National aperture; width = 2.5 μm ; length = 3.0 mm) and collimated by an achromatic doublet (49-926, Edmund optics; $f = 15$ mm). The collimated light passed through a 3D-printed rectangular aperture and focused by another achromatic doublet (49-927, Edmund optics; $f = 22.5$ mm). The illumination beam was folded by a dielectric mirror (87-367, Edmund optics; reflectivity > 99%) and transmitted through a plastic imaging window (material = polymethyl methacrylate (PMMA); thickness = 250 μm) to form a light sheet on the tissue.

In the detection path, scattered light from the tissue was collected by a custom objective lens ($f = 14.9$ mm; NA = 0.25) and focused by a micro-video lens (66-896, Edmund optics; $f = 35$ mm; F/2) onto a monochromatic CMOS sensor (daA3840-45um, Basler; $3,840 \times 2,160$ pixels; pixel size = 2.0 μm ; imaging speed = 45 fps). The detection optics had a magnification of 2.35, resulting in the pixel size of 0.85 μm and the FOV of 3.26 mm \times 1.84 mm on the tissue xy-plane.

Mechanical holders were custom-designed and fabricated using a 3D printer (Form 3+, Formlabs) and biocompatible material (Biomed Black resin, Formlabs). Most of the optical elements were passively aligned using tight fit with the mechanical holders to ensure concentricity, while some optical components were actively aligned.

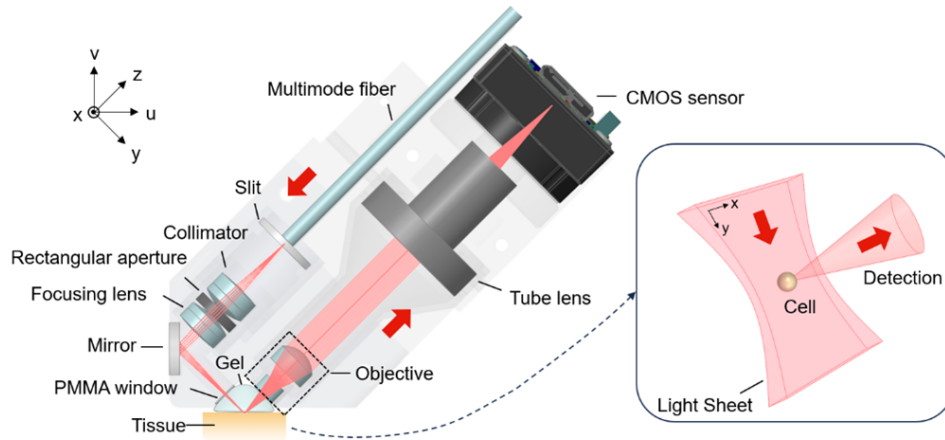


Figure 5.1: Schematic of the compact sLSM probe.

5.1.2 Custom Objective Lens Design

The custom objective lens was designed using OpticsStudio (Zemax). The objective lens was composed of an aspheric convex lens (material = PMMA) and an aspheric bi-concave lens (material = PMMA) as shown in Fig. 5.2(a). An immersion medium (refractive index = 1.34) was used between the distal surface of the bi-concave lens and tissue. The aspheric convex lens had an aspheric surface on the proximal side (farther from the tissue) and a nearly flat surface on the distal side (closer to the tissue). The lens stop was located on the proximal side. The bi-concave lens had an aspheric surface on the proximal side and a spherical surface on the distal side. The two aspheric lenses were fabricated by diamond turning. The convex lens had the clear aperture of 7.4 mm in diameter and center thickness of 5.0 mm. The bi-concave lens had the clear aperture of 4.6 mm in diameter and center thickness of 2.9 mm. The distance between the two lens elements was designed as 3.0 mm. During the alignment procedure, the distance between the two lenses was actively adjusted

to minimize the FWHM of the measured PSF. A stainless-steel washer (thickness = 0.05 mm, outer diameter = 4.7 mm, inner diameter = 3.2 mm) was placed on the distal flange of the bi-convex lens to block stray light. During the optimization process, both the working distance and the diameter of the bi-concave lens were regulated to prevent mechanical interference between the lens and tissue when the objective lens is angled at 45° relative to the tissue surface. The effective focal length and NA of the objective lens were 14.9 mm and 0.25, respectively. The theoretical resolution at 638 nm was $1.32 \mu\text{m}$. The lens was designed to have a diffraction-limited FOV of ± 1.0 mm in the tissue space, as shown in the root-mean-square (RMS) wavefront error plot as a function of field (Fig. 5.2(b)). The field curvature of the lens was controlled to have diffraction-limited performance within the defocus range of $\pm 2.5 \mu\text{m}$, corresponding to the theoretical thickness of the light sheet illumination, as shown in Fig. 5.2(c). A Monte-Carlo tolerance analysis was conducted on the objective lens based on the lens manufacturing tolerances. The tolerance analysis showed that more than 72% of the objective lenses would provide diffraction-limited performance.

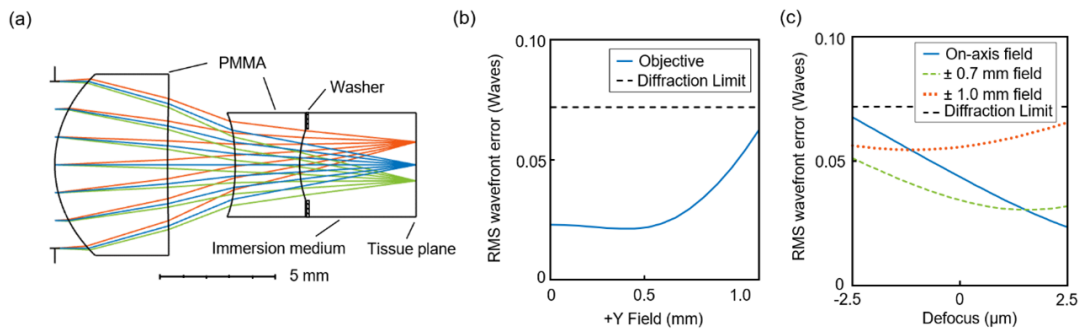


Figure 5.2: Schematic of the custom objective lens (a), wavefront error performance as a function of field (b), and wavefront error performance as a function of defocus (c).

5.1.3 Light Sheet Thickness Simulation

For sLSM imaging, it is critical to maintain a thin light sheet thickness over a large depth range (along the y -axis in Fig. 5.1). This can be achieved by using a small NA for illumination. In the compact sLSM probe, the aperture length along the x -axis and width along the y -axis were set to 9.0 mm and 2.9 mm, respectively, to provide the illumination NA of 0.2 along the x -axis and 0.06 along the z -axis (after 90° reflection by the fold mirror). This aperture arrangement resulted in hourglass-shape light sheet illumination with a theoretical thickness of $5.0 \mu\text{m}$ and DOF of $206.2 \mu\text{m}$.

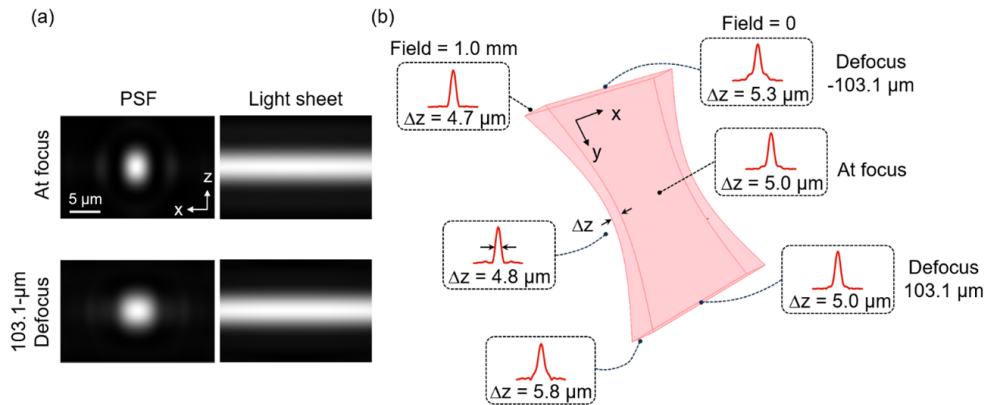


Figure 5.3: Simulated Huygens PSFs and light sheet illumination for the on-axis field at the focus and at $103.1\text{-}\mu\text{m}$ defocus (a), and light sheet thickness for different fields and defocus locations (b).

The choice of lenses in the illumination optics was initially based on first-order geometric optics. Therefore, the illumination performance degradation caused by aberrations was not initially considered. Due to the larger NA along the x -axis and smaller NA along the z -axis, aberrations were mainly expected along the x -axis, as shown in the simulated Huygens PSF (Fig. 5.3(a)). The light sheet illumination, determined by the convolution between the PSF

and image of the slit (longer along the x-axis), therefore maintains a narrow thickness, as shown in Fig. 5.3(a). We evaluated the light sheet thickness for different fields (along the x-axis) and different defocus locations (along the y-axis) to ensure the light sheet thickness was consistently small across the entire imaging FOV and depth range. The light sheet thickness for different fields ($x = 0$ and ± 1.0 mm) and defocus locations ($y = 0$ and ± 103.1 μm) was simulated using the extended diffraction image analysis function in OpticsStudio, which considered both diffraction and aberration effects of the illumination optics. As shown in Fig. 5.3(b), the theoretical light sheet thickness was maintained small, ~ 5.0 μm , even though aberrations were present along the x-axis.

5.1.4 Custom Objective Lens Performance Test

Optical performance of the objective lens was evaluated by imaging a UASF resolution target and a custom multi-pinhole target. The UASF resolution target image was used to identify the smallest resolvable line period. The image of the custom multi-pinhole target was used to measure the FWHM of the PSF across the entire field of view. The custom multi-pinhole target had pinholes periodically spaced along horizontal and vertical directions (pinhole diameter = 0.67 μm ; period = 20 μm). The multi-pinhole target was fabricated by etching the pinhole pattern on a glass substrate (thickness = 1.5 mm) deposited with reflective chrome coating. We conducted simulation of the effect of the pinhole size by convolving the theoretical PSF of the objective lens with the pinhole geometry and calculating the FWHM of the convolved profile. The simulation results showed that only a small amount of measurement error (5%) was expected when measuring the expected resolution of 1.32 μm . The period of the pinhole pattern, 20 μm , was set significantly larger than the pinhole

diameter so that the image of each pinhole does not affect the image of neighboring pinholes. In order to evaluate the performance of the objective lens alone, the detection optics were assembled and mounted vertically facing downwards. The USAF resolution target or the multi-pinhole target was placed horizontally under the objective lens and was trans-illuminated from below the target. Light transmitted through the target was collected by the objective lens and imaged by the tube lens onto the CMOS sensor.

5.1.5 Probe Performance Test

The axial and lateral resolution of the sLSM probe was measured simultaneously by imaging a custom resolution target with a periodic line pattern (line width = $0.5 \mu\text{m}$; period = $30 \mu\text{m}$) we previously developed [106]. The line pattern was made on a chrome-coated glass substrate (thickness = 1 mm) by photolithography and etching. The target was placed horizontally with the reflective lines parallel to the u-axis and facing upwards. Only a small portion of each line was illuminated by the light sheet, with the illumination width determined by the thickness of the light sheet. The lines reflected the illumination light towards the detection optics, producing an image that showed multiple partial lines. In the sLSM image of the line pattern, the FWHM of the line height along the y-axis was measured as the axial resolution of sLSM. The FWHM of the line width was measured as the line-spread function (LSF) or the lateral resolution of the detection optics. Therefore, both lateral and axial resolution was measured from a single sLSM image of the line pattern at a given depth. The target was placed horizontally with the reflective lines parallel to the u-axis and facing upwards. The resolution target was translated along the v-axis with a step size of $10 \mu\text{m}$ to measure the resolution at different imaging depths. The exposure time of

the CMOS sensor was adaptively adjusted to avoid the signal saturation. Index-matching gel (GenTeal Tears Gel, Alcon) was placed between the resolution target and the probe as an immersion medium.

Tissue *ex vivo* imaging performance was tested by imaging formalin-fixed human anal tissues. The sLSM images acquired by the compact probe were compared with the images previously acquired with the bench sLSM device[112] using off-the-shelf objective lenses (N10XW-PF, Nikon; $f = 20$ mm; $NA = 0.3$; water immersion) and H&E-stained histologic images. The epithelial side of the tissue was placed upwards. The index-matching gel was placed between the tissue and probe. The protocol for imaging formalin-fixed human anal tissues *ex vivo* was the same as the previous experiments [112]. The cellular features visualized in sLSM images were analyzed in comparison with the features shown in the corresponding histologic images by our clinical collaborators at Stanford University.

5.2 Results

5.2.1 Compact sLSM Probe

A photograph of the compact sLSM probe is shown in Fig. 5.4. Overall dimensions of the prototype were 4 cm in height and width, and 10 cm in length. The illumination power on the tissue was 0.14 mW. The exposure time was set at ~ 0.5 msec, resulting in a real-time imaging speed with a frame rate of 45 fps, which is the highest frame rate the CMOS sensor supported. The material cost of the compact sLSM probe was low, $<2,000$, as shown in the Table 5.1. The unit price of the custom objective lens was relatively high, $<1,200$, due

to the cost associated with diamond turning and anti-reflection coating. The objective lens cost can be reduced significantly by using injection molding in the future.



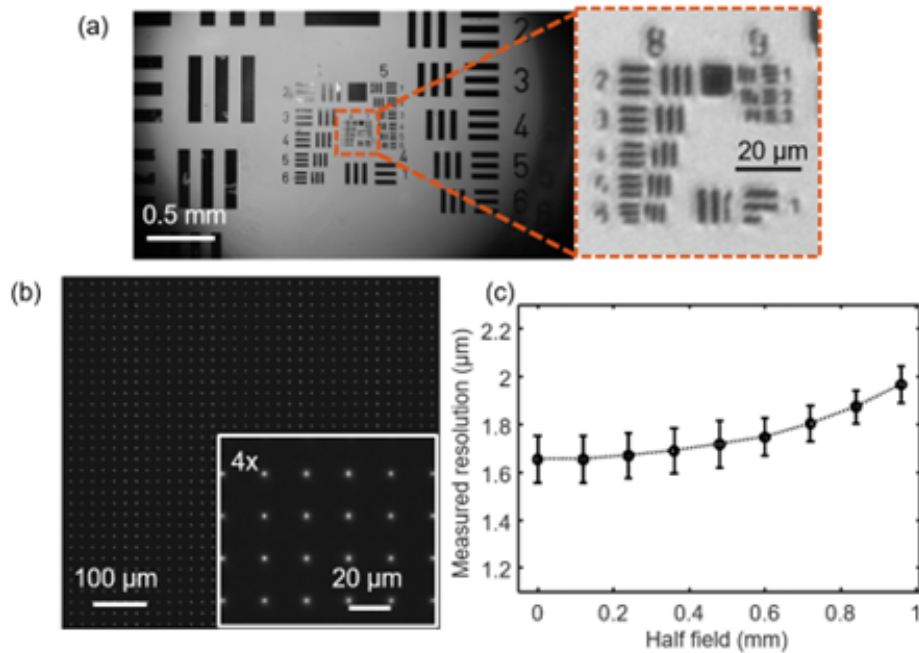
Figure 5.4: Photo of the sLSM probe.

5.2.2 Custom Objective Lens Performance

A representative image of the USAF resolution target is shown in Figure 5.5(a). The smallest line pattern resolvable by the custom objective lens was group 9, element 1 (linewidth = $0.97 \mu\text{m}$) along both the horizontal and vertical directions, as shown in the inset of Fig.5.5(a). However, the USAF image exhibited obvious side lobes surrounding the line pattern, indicating the presence of aberrations. A representative image of the custom multipinhole target is shown in Fig. 5.5(b). The measured PSF FWHM of the custom objective lens as a function of field (Fig. 5.5(c)) shows that the custom objective lens provides the resolution of $1.65 - 1.97 \mu\text{m}$ across the FOV of $\pm 1.0 \text{ mm}$.

Table 5.1: Bill of materials

Component	Cost (\$)
Slit	115
Achromatic doublets ($\times 2$)	134
Mirror	75
PMMA window	0.1
Objective lens - Aspheric convex	621.7
Objective lens - Aspheric bi-concave	561.3
Tube lens	67
CMOS sensor	199
3D printed materials	30
Mechanical mounts	55
Total	1858.1

**Figure 5.5:** USAF target image (a), custom multi-pinhole target image (b), and measured resolution as a function of field (c) of the custom objective lens.

5.2.3 Probe Resolution Measurement

Figure 5.6(a) shows a representative image of the custom line pattern target captured by the compact sLSM probe. The measured lateral resolution was $1.90 \pm 0.07 \mu\text{m}$. The axial resolution at the center of the imaging depth range was measured to be $5.2 \mu\text{m}$. Within the theoretical DOF of $206.2 \mu\text{m}$, the light sheet maintained a thickness smaller than $5.6 \mu\text{m}$.

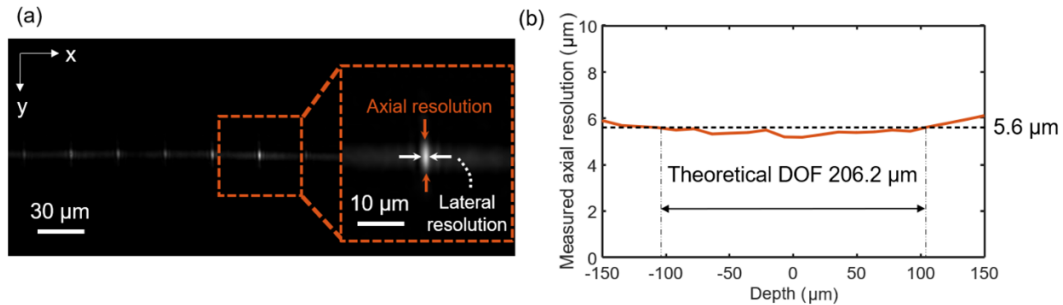


Figure 5.6: Custom resolution target image (a) and measured axial resolution as a function of depth (b).

5.3 Tissue Imaging Performance

Figure 5.7 shows representative sLSM and histologic images of fixed normal anal squamous mucosa. The image acquired by the compact sLSM probe (Figure 5.7(a)) visualizes tissue details over a width of 2 mm. The epithelium and stroma are clearly delineated. A magnified view of the same image (Figure 5.7(b)) visualizes a honeycomb pattern of squamous epithelial cells with hypo-reflective nuclei (arrows) and hyper-reflective cytoplasm and cell membranes, in a similar manner to the image obtained with the bench sLSM device (Figure 5.7(c)) and with a similar nuclear size and spacing to the histologic image (Figure 5.7(d)).

Figure 5.8 shows representative sLSM and histologic images of LSIL. The image obtained with the compact sLSM probe (Figure 5.8(a)) clearly distinguishes the layer of parakeratosis from the underlying epithelium, which is thickened compared to normal squamous epithelium. The higher-magnification view of the compact sLSM probe image (Figure 5.8(b)) shows that the honeycomb pattern of the squamous epithelial cells is still retained but the cellular features have more variability in size and shape than normal squamous epithelium. A similar trend is shown in the image obtained with the bench sLSM device (Figure 5.8(c)) and the histologic image (Figure 5.8(d)).

Figure 5.9 shows representative sLSM and histologic images of fixed HSIL. A large-area sLSM image obtained with the compact sLSM probe (Figure 5.9(a)) shows the lack of clear distinction between the epithelium and stroma. The increased epithelial thickness and stronger scattering in HSIL might have degraded the resolution at the base of the epithelium more in HSIL than in normal squamous epithelium, making the epithelium-to-stroma interface less distinctive. A higher-magnification view (Figure 5.9(b)) and its inset visualize dense and irregular arrangement of small hypo-reflective nuclei (arrows) with a varying size and shape. The trend of crowded nuclei is also shown in the image obtained with the bench sLSM device (Figure 5.9(c)) and the histologic image (Figure 5.9(d)).

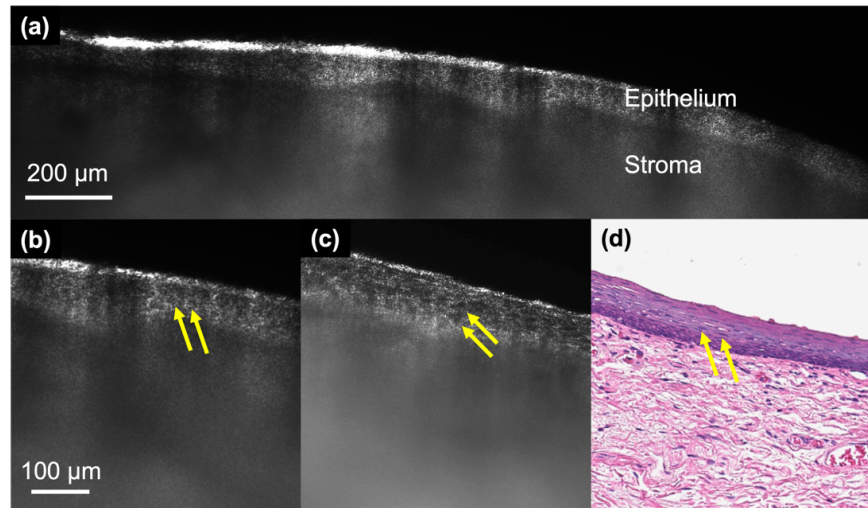


Figure 5.7: sLSM images of normal anal squamous mucosa obtained with the compact sLSM probe (a, b) and bench sLSM device (c), and histologic image of the same tissue (d). arrows –nuclei.

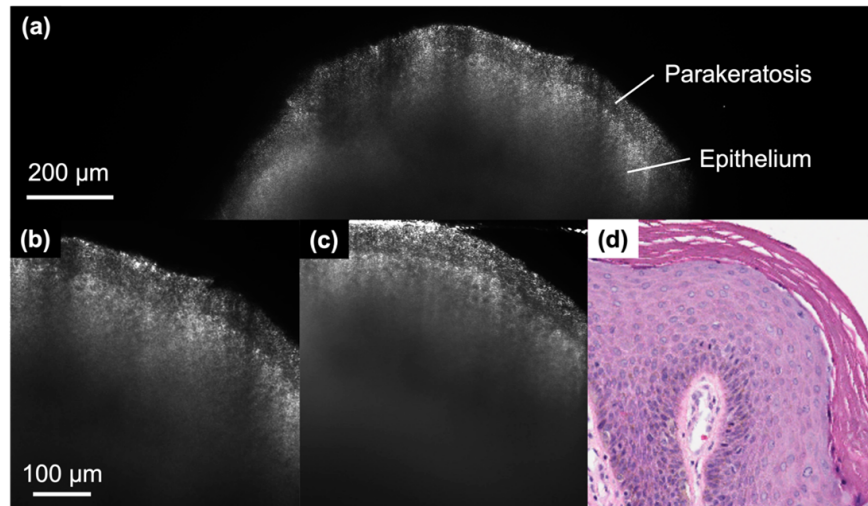


Figure 5.8: sLSM images of LSIL obtained with the compact sLSM probe (a, b) and bench sLSM device (c), and histologic image of the same tissue (d).

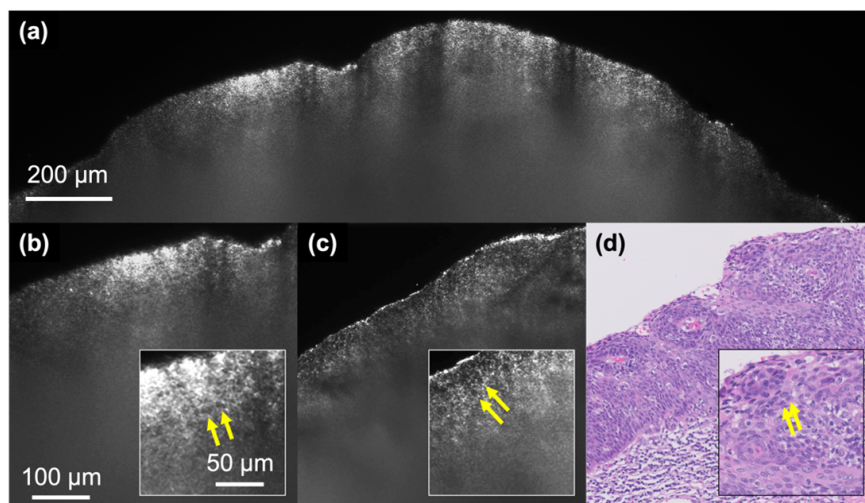


Figure 5.9: sLSM images of HSIL obtained with the compact sLSM probe (a, b) and bench sLSM device (c), and histologic image of the same tissue (d). arrows –nuclei.

5.4 Discussion

In this Chapter, the development of a compact sLSM probe that can visualize cellular details of unstained tissues just using the intrinsic scattering contrast was presented. We designed a custom miniature objective lens to achieve the NA of 0.25 with a diffraction-limited FOV of ± 1.0 mm. The field curvature of the custom objective lens was made small to ensure the detection focal plane coincided with the illumination plane within the target FOV. The compact probe achieved the lateral resolution of $1.90 \pm 0.07 \mu\text{m}$ and axial resolution better than $5.6 \mu\text{m}$ over a depth range of $206.2 \mu\text{m}$. The illumination power on the tissue of 0.14 mW allowed for a short exposure time even when imaging fixed human anal tissues. Preliminary results showed that the compact sLSM probe was able to visualize cellular features in formalin-fixed human anal tissues *ex vivo* in a similar manner to the bench sLSM device. Differences in morphologic features between normal squamous epithelium, LSIL, and HSIL were clearly visualized by the compact sLSM device. The preliminary results indicate

that the compact sLSM probe might be promising for imaging epithelial cellular features in unstained human tissues *ex vivo* in a pathology lab or for directly imaging human patients *in vivo*. Formalin-fixed anal tissues provided a negative nuclear contrast (nuclei were dark). This is contrary to fresh anal biopsy tissues stained with low-concentration acetic acid, where sLSM images exhibited bright cell nuclei [113]. While the negative nuclear contrast made sLSM imaging of fixed tissues more challenging than fresh tissues, fixed tissues were used for comparing the compact sLSM probe to the bench sLSM device, because the cellular features were fixed and did not degrade over time.

Several limitations were found in the compact sLSM probe. The measured resolution of the custom objective lens was slightly worse than the theoretical one. This discrepancy was mainly caused by the manufacturing and alignment errors. Additionally, there was a difference between the PSF FWHM of the custom objective lens alone (1.65-1.97 μm) and the LSF FWHM of the whole probe (1.90 μm). Broadening of the LSF might have been caused by the side lobes in the objective lens PSF. Further desensitization of the objective lens during the design process and more accurate alignment might reduce the measured PSF FWHM and reduce the side lobes.

Over the imaging depth of 100-200 μm , cellular features were readily visible. While this imaging depth is significantly smaller than the imaging depth of OCT, it is likely adequate for visualizing nuclear changes associated with squamous intraepithelial lesions, as shown in the sLSM images of the fixed anal tissues in this paper, the sLSM images of fresh anal biopsy tissues [113], and confocal microscopy images of cervical squamous intraepithelial lesions [37, 38]. However, tissue structures in deeper tissue regions such as tumor nests might be helpful in determining the tumor invasion. In a future sLSM probe, a longer wavelength can be

coupled into the illumination fiber along with 638 nm used in this paper to provide a larger imaging depth albeit the reduced resolution [106].

The image contrast was slightly degraded in the imaged obtained with the compact sLSM probe when compared with those obtained with the bench sLSM device. The contrast degradation might have been caused by stray light. Although we used a stainless-steel washer in the custom objective lens to block the stray light, there were two limitations: the washer did not completely cover the distal flange of the bi-concave lens due to the size error of the washer, and the washer was not blackened and was highly reflective. An example showing the stray light issue is the bright signals observed on the lines at group 4, element 2 of the USAF target image (Fig. 5.5(a)). More careful control of stray light during the design process, and use of better light-blocking material for the washer might mitigate this issue in future development.

The size of probe would need to be miniaturized for certain clinical applications such as imaging of anatomically hidden areas (e.g., anal canal, cervix). The size of the current sLSM probe was mainly limited by the size of the CMOS sensor. By replacing the current sensor with a sensor in a more compact packaging, the dimension of the probe can be further reduced. Additionally, a custom objective lens with a similar NA but with a shorter focal length can be used to reduce the probe size, albeit the small FOV.

The compact sLSM probe in this paper was evaluated to capture scattering signals. However, there are no fundamental limitations in using the compact sLSM probe for fluorescence imaging. It would be of interest to implement an illumination scheme of using two different spectral bands (one for fluorescence excitation and the other for scattering) and an

emission filter in the detection optics, which could provide both fluorescence and scattering images with a compact LSM probe.

Chapter 6

Conclusion

6.1 Summary

This dissertation explored the potential of adapting scattering-based light sheet microscopy (sLSM) as an *in vivo* microscopy technology to enhance screening procedures for anal cancer. Four studies were designed and executed to provide the necessary groundwork for introducing sLSM into clinical practice: 1) investigation of the optimal wavelength for imaging anal tissues with sLSM using a multi-wavelength bench sLSM setup; 2) design and development of a method to reduce speckle and shadow artifacts in sLSM, as well as the evaluation of a bench sLSM setup based on this method; 3) assessment of the *ex vivo* imaging capabilities of sLSM on fresh human anal biopsies and investigation into the diagnostic accuracy for identifying precancerous conditions; 4) development of a compact, handheld sLSM probe and demonstration of its capability for *ex vivo* imaging of human anal tissues.

Chapter 2 concentrated on optimizing the imaging wavelength for sLSM. A multi-wavelength bench setup that facilitates this investigation was created. *Ex vivo* imaging of formalin-fixed human anal tissues at different wavelengths was conducted and analyzed, finding that approximately 600 nm is well-suited for balancing imaging depth and cellular contrast necessary for visualizing cellular morphological features indicative of anal diseases.

This study helped set the parameter for future development of clinically-viable sLSM devices. In addition, a custom resolution target was designed and developed to facilitate the optical performance measurement of sLSM.

Chapter 3 introduced a method to mitigate speckle noise and shadow artifacts in sLSM imaging. The presence of these artifacts complicates the visualization of cellular details. A bench sLSM setup employing an LED, slit, and rectangular aperture for light sheet illumination was developed, which significantly reduced the speckle noise (by 72%) and shadow artifacts, thus enhancing the clarity for observing cellular details.

Chapter 4 presented a pilot study on imaging fresh human anal tissues with the bench sLSM and evaluating the diagnostic accuracy using sLSM images. It was demonstrated that sLSM can replicate the diagnostic features of squamous dysplasia in fresh anal biopsies that were previously observed in the H&E images. This study not only validates sLSM as a potential tool for imaging cellular features associated with the anal disease progression on fresh human tissues, but also showed the diagnostic accuracy of anal dysplasia close to the traditional histology methods, demonstrated the great potential for applying sLSM to guide the anal cancer screening.

Finally, Chapter 5 focused on the development of a compact, handheld sLSM probe, showing the feasibility of translating this technology from bench scale to handheld scale without significant degradation of the imaging performance. A custom miniature objective lens was designed to have high resolution, large FOV, and minimal field curvature. This compact sLSM achieved similar imaging performance as the bench sLSM for *ex vivo* imaging of formalin-fixed human anal tissues. While this probe is not yet small enough for direct imaging of tissues within the human anal canal, we learned valuable lessons regarding the

engineering challenges anticipated for future *in vivo* endoscopy development through the development of this probe. Additionally, this probe may be employed in future pathology studies to facilitate the volumetric imaging of large surgical tissues, potentially reducing the need for extensive tissue preparation for histologic imaging [114].

6.2 Future Work

In the future, a sLSM endoscope will be developed for *in vivo* imaging of human anal tissues in clinical settings. Developing a miniaturized LSM for cross-sectional view of the human tissues requires thoughtful careful design considerations due to the two separated optical paths involved. The efforts and thoughts we put into developing the compact sLSM probe will guide the future development of the *in vivo* sLSM devices. At present, the engineering considerations for miniaturizing LSMs as endoscope devices have not been widely studied yet, especially for imaging human organs non-invasively. Only a few studies have demonstrated the miniaturization of LSMs. Engelbrecht et al. reported a miniaturized LSFM device using a cylindrical gradient-index (GRIN) lens and a right-angle microprism, and evaluated its *in vivo* imaging capability on mouse brain. However, this device is invasive because it requires the insertion of the microprism into the tissue for illumination, and it collects en face images of the tissue, not cross-sectional views [115]. Roldan-varona et al. reported a LSFM endoscopy device introduced the plane illumination with an annular mirror at the endoscopy distal tip using an end-cap structure, and collected en face images of the tissue with the central multimode fibers [116]. However, this method also provided en face images instead of cross-sectional images. Additionally, it required tissues to be deformed to fill the space of the endcap, and air gap due to the insufficient tissue deformation can

reduce the illumination quality. Patel et al. reported a LSM with a handheld (2.2 cm in diameter) probe that can image tissues *in vivo* using auto-fluorescence signals and can provide cross-sectional view of the tissue [114]. However, the size of the probe is still not ideal for imaging human anal canal. In the future, an *in vivo* sLSM probe will be carefully designed to better adapt to the applications in anal canal or other organs.

Another potential direction to improve the sLSM technology is the computer-aided diagnosis. Artificial intelligence techniques could be used for sLSM image analysis and disease classification. For example, convolutional neural networks (CNN) can help extract the diagnostic features shown in sLSM images and conduct quantitative diagnosis with high speed and potentially high accuracy. This could potentially lead to real-time diagnosis and early treatment interventions. Additionally, through the learning process with vast amounts of imaging data, CNN is also potential to extract subtle tissue morphology features that might indicate early disease stages but are undetectable/difficult to detect by the human eye, thus increasing the diagnostic accuracy. Additionally, the computer-aided diagnosis could serve as a valuable tool for initial screenings, particularly in settings where direct access to pathology expertise is limited.

Appendix A

Investigation of different wavelengths for sLSM

This section includes the published manuscript for evaluating different wavelengths for sLSM. The publication can be found at the Optica Publishing Group. The full citation is listed below.

Jingwei Zhao, Nachiket Kulkarni, Erika Dobo, Michelle J. Khan, Eric Yang, and Dongkyun Kang, "Investigation of different wavelengths for scattering-based light sheet microscopy," *Biomed. Opt. Express* 13, 3882-3892 (2022). <https://doi.org/10.1364/BOE.459823>



Investigation of different wavelengths for scattering-based light sheet microscopy

JINGWEI ZHAO,¹ NACHIKET KULKARNI,¹ ERIKA DOBO,² MICHELLE J. KHAN,² ERIC YANG,² AND DONGKYUN KANG^{1,3,*}

¹James C. Wyant College of Optical Sciences, University of Arizona, Tucson, Arizona 85721, USA

²School of Medicine, Stanford University, Stanford, California 94305, USA

³Department of Biomedical Engineering, University of Arizona, Tucson, Arizona 85721, USA

*dkkang@email.arizona.edu

Abstract: Scattering-based light sheet microscopy (sLSM) is a microscopy technique that can visualize cellular morphologic details based on the scattering signal. While sLSM was previously shown to image animal tissues *ex vivo* at a cellular resolution, the wavelength used was chosen based on other *in vivo* microscopy technologies rather than through a comparison of the sLSM imaging performance between different wavelengths. In this paper, we report the development of a multi-wavelength sLSM setup that facilitates the investigation of different wavelengths for sLSM imaging. Preliminary results of imaging human anal tissues *ex vivo* showed that the sLSM setup allowed for comparisons of the cellular imaging performance at the same tissue location between different wavelengths. Both the quantitative analysis of the image contrast and the visual assessment by a pathologist showed that the imaging depth increased with wavelength, and the imaging depth increase was most notable around 600 nm. The preliminary results showed that the multi-wavelength sLSM setup could be useful in identifying the optimal wavelength for the specific tissue type.

© 2022 Optica Publishing Group under the terms of the [Optica Open Access Publishing Agreement](#)

1. Introduction

In vivo microscopy allows for direct examination of disease-associated cellular morphologic changes from the human tissue without removing the tissue from the patient [1]. Several *in vivo* microscopy technologies have been translated into clinically-viable medical devices in various clinical fields, including reflectance confocal microscopy in ophthalmology, dermatology, and gastroenterology [2–4], and optical coherence tomography (OCT) in ophthalmology, cardiology, and gastroenterology [5–7]. However, most of the existing *in vivo* microscopy technologies have challenges in simultaneously achieving a high resolution and a large field of view (FOV). For example, the commercial reflectance confocal microscopes for skin imaging have a high lateral (1.25 μm) and axial resolution (5 μm) [8] thanks to the use of a high-numerical aperture (NA) objective lens. But its FOV is limited to 500–750 μm [9,10], which poses challenges in imaging the entire suspicious tissue region. On the other hand, OCT has a larger FOV, approximately 2–3 mm, but its resolution is around 10–20 μm , which is suitable for imaging architectural features rather than cellular and sub-cellular features [11,12]. High-resolution, large-FOV OCT technologies have been recently developed [13,14]. However, the use of an expensive broadband coherent light source likely increases the device cost.

Light sheet microscopy (LSM) is a microscopy technique that became popular in basic life science research [15,16]. LSM uses separate optical paths for illumination and detection, where the lateral resolution is determined by the detection optics, and the axial resolution by both the illumination and detection optics. Most of the previous LSM work was aimed to achieve a sub-cellular resolution, < 1 μm [16]. If the requirement for the LSM axial resolution could be relaxed to provide an axial resolution used for reflectance confocal microscopy, $\sim 5 \mu\text{m}$, an illumination optics with a low NA (< 0.1) could be used. The low illumination NA in turn could

generate a light sheet over a relatively large depth range, hundreds of μm . If the requirement for the lateral resolution of LSM could be relaxed to achieve a lateral resolution used for reflectance confocal microscopy, 1-2 μm , a detection objective lens with a moderate NA, ~ 0.3 could be used. The moderate-NA objective lens in turn would provide a FOV of several mm, comparable to a typical FOV of OCT.

Taking this approach of achieving a resolution comparable to the resolution of reflectance confocal microscopy while providing a large FOV, we recently demonstrated scattering-based light sheet microscopy (sLSM) of thick, unstained tissues [17]. sLSM detects scattered light signals generated by the refractive index difference between certain sub-cellular/cellular components and their surroundings. In fact, the first LSM setup was based on scattering contrast [18], and several groups successfully demonstrated sLSM imaging of plant roots [19], zebrafish embryos and tumor spheroids [20], and fibroblasts [21]. In our previous experiment, sLSM was shown to visualize cellular details of thick, unstained animal tissues *ex vivo* with a high resolution (1.8 μm and 6.7 μm for the lateral and axial resolution, respectively) over a large FOV (~ 2.5 mm). Another potential advantage of sLSM is that the device cost can be low due to the use of a moderate-NA objective lens, an inexpensive light source such as a LED and superluminescent diode, and a standard CMOS sensor rather than an expensive scientific CMOS sensor.

The previous sLSM setup used a near-infrared spectrum around 834 nm because of its common use in reflectance confocal microscopy and OCT [22,23]. However, there is a need to investigate the optimal wavelength for the specific tissue imaging application. For instance, a shorter wavelength can be used to achieve the same resolution with a lower NA than a longer wavelength. A low illumination NA can increase the light sheet length, and a low detection NA can make the detection objective lens design easier [24]. On the other hand, a longer wavelength is scattered less and therefore can provide a larger imaging depth [25,26]. An sLSM setup that can image the same tissue location with several different wavelengths would facilitate the investigation of the optimal wavelength for the specific tissue type. Such a multi-wavelength sLSM setup needs to be carefully designed to allow for easy changes of the wavelength especially when each lens of the sLSM setup has its own chromatic focal shift.

In this paper, we report the development of a multi-wavelength sLSM setup that facilitates the investigation of different wavelengths for sLSM imaging. We also developed a custom resolution target that enables easy, quantitative measurement of the lateral and axial resolution for each wavelength as a function of imaging depth. Finally, we tested the sLSM setup for imaging human tissues *ex vivo* with different wavelengths, and the imaging performance was evaluated quantitatively with an edge contrast metric and visually by a pathologist.

2. Method

2.1. Multi-wavelength sLSM setup

The schematic of the multi-wavelength sLSM setup is shown in Fig. 1. In the illumination path, light from a supercontinuum laser (SC-5, YSL Photonics; wavelength range = 470–2400 nm) was coupled into a single-mode fiber (P3-630A-FC-1, Thorlabs; core diameter = 9.0 μm ; NA = 0.1 - 0.14). Light from the other end of the fiber was collimated by an achromatic doublet ($f = 40$ mm). The collimated beam was filtered by a bandpass filter to generate a narrow spectral band (full-width-half maximum, FWHM = 40 nm). Different bandpass filters were used to change the center wavelength from 500 nm to 800 nm with a 100 nm interval. The illumination light was further transmitted through a 3D-printed rectangular aperture and focused by a cylindrical lens ($f = 75$ mm) and an objective lens (MRH07120, CFI60 Plan Fluor 10x, Nikon; $f = 20$ mm; NA = 0.3; water immersion) to form a light sheet on the tissue. The width of the aperture along the x-axis was 6.8 mm, which resulted in the light sheet width of 1.68 mm on the tissue. The height of the aperture along the z-axis was adjusted for each wavelength to generate the light

sheet thickness of 5 μm (e.g., the aperture height was 1.5 mm for 500 nm, and 1.8 mm for 600 nm). A uniform beam profile was assumed in this theoretical calculation.

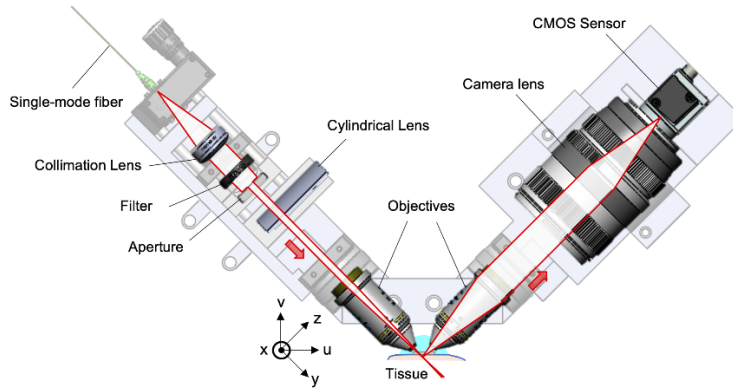


Fig. 1. Schematic of the multi-wavelength sLSM setup.

The chromatic focal shift of the objective lens was experimentally measured, and the measured chromatic focal shift was 38.4 μm for the spectral range of 500–800 nm. An apochromat objective lens might provide a smaller chromatic focal shift than the current fluorite objective lens. But apochromat, water-dipping objective lenses are not available with the long focal length used in this paper, 20 mm, which is important in achieving a large FOV. The focal length of the objective lens increased as a function of wavelength. If a collimation lens were selected without careful consideration of its own chromatic focal shift, the overall chromatic focal shift could be increased, making it challenging to make the light sheets of different wavelengths overlap with each other. For instance, if an achromatic doublet designed for the visible and near-infrared spectra (49354, Edmund) were used as the collimation lens, it would result in the overall chromatic focal shift of 102 μm . We evaluated several off-the-shelf achromatic doublets and triplets using OpticsStudio (ZEMAX) to find the lens that best compensates for the chromatic focal shift of the objective lens. The chosen achromatic doublet (AC254-040-C, Thorlabs) reduced the overall chromatic focal shift to 24.6 μm .

In the detection path, scattered light from the tissue was collected by a second objective lens (MRH07120, CFI60 Plan Fluor 10x, Nikon) and focused by a camera lens ($f = 85$ mm; F/2) onto a monochromatic CMOS sensor (acA4024-29um, Basler; $4,024 \times 3,036$ pixels; pixel size = 1.85 μm). A camera lens rather than a tube lens or achromatic doublet was used because tube lenses typically have a long focal length (180–200 mm), which would generate an image larger than the sensor's active area, and camera lenses generally have a better correction for field curvature than achromatic doublets with the same focal length. The detection optics had a magnification of 4.25, resulting in the pixel size of 0.44 μm and the FOV of 1.75 mm \times 1.32 mm on the tissue xy -plane. The chromatic focal shift of the objective lens, 38.4 μm , was difficult to reduce to a level smaller than the depth of focus (DOF) of the objective lens, 7.4–11.8 μm , using an off-the-shelf camera lens. Therefore, when the wavelength was changed, the focus of the detection objective lens was manually adjusted based on the image sharpness.

2.2. Custom resolution target

The lateral resolution can be measured by imaging standard resolution targets with sharp edges (e.g., USAF resolution target), and the axial resolution can be measured by imaging a mirror. This standard approach, however, requires changes of the specimen between the resolution target and mirror. Microspheres can be used to measure both the lateral and axial resolution, but

their distribution is not always uniform, and this approach requires acquisition of volumetric image data with a precise translation of the specimen. When evaluating the multi-wavelength sLSM setup, multiple resolution measurements are required at different depths and for different wavelengths. We developed a custom resolution target (Fig. 2) that allows for direct measurement of the lateral (x -axis) and axial (y -axis) resolution from a single sLSM image.

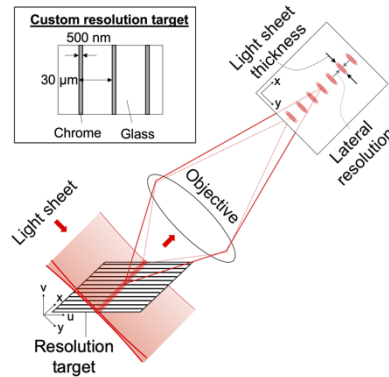


Fig. 2. Schematic of the custom resolution target and its use for measuring the lateral and axial resolution of sLSM.

The custom resolution target was made of a periodic pattern of thin reflective chrome lines (width = 500 nm, period = 30 μm). The target was placed horizontally with the line length parallel to the u -axis. Only a small portion of the target was illuminated by the light sheet, and the illumination width was determined by the light sheet thickness or the axial resolution of sLSM. The portion of the chrome lines within the illuminated region reflected light towards the detection objective lens. The image of the custom resolution target visualized multiple partial lines. The height of each partial line was mainly determined by the light sheet thickness or the axial resolution of sLSM. The width of each partial line image was primarily determined by the line-spread function or lateral resolution of the detection optics. Therefore, both the lateral and axial resolution was measured from a single sLSM image at a given imaging depth. In order to evaluate the resolution at a different depth, the resolution target was translated along the v -axis, which in turn changed the location of the illuminated area on the resolution target. The width of the line pattern, 500 nm, was chosen to keep the measurement error for the lateral resolution small. Using Matlab (Mathworks), we conducted simulation of the measured resolution by convolving the line-spread function of the detection optics with the width of the line pattern and calculating the FWHM of the convolved profile. The simulation results showed that a 10-14% error was expected when measuring the lateral resolution of 0.85 - 1.36 μm , the resolution expected for 0.3 NA and the wavelength of 500–800 nm. The period of the line pattern, 30 μm , was set significantly larger than the line width so that the image of each line does not affect the image of neighboring lines.

The custom resolution target was fabricated by photolithography and etching (Front Range Photomask). The line pattern was made on a glass substrate (thickness = 1 mm) with a chrome coating (optical density = 5). The line pattern width and etching process were iteratively optimized to generate the target line width of 500 nm. The custom resolution target was examined by scanning electron microscopy (Fig. 3(a)) and white light interferometry (Fig. 3(b)). The line width measured by electron microscopy, ~ 560 nm, closely matched the design width, 500 nm. There was a broader dark area around the thin line in the electron microscopy image with a width of ~ 3 μm . The white light interferometry image (Fig. 3(b)) confirmed that the dark area on the

electron microscopy image was not optically reflective, and the strong reflectance signal was confined to the thin line region with a width of ~ 560 nm.

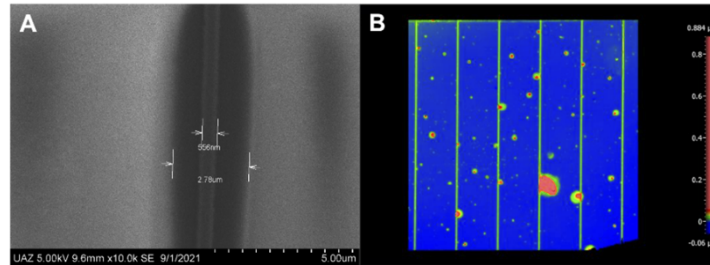


Fig. 3. Images of the custom resolution target obtained with scanning electron microscopy (A) and white light interferometry (B).

2.3. Performance test

The axial and lateral resolution was measured using the custom resolution target. Images of the resolution target were acquired, while the resolution target was translated vertically (along the v -axis) with a step size of $10 \mu\text{m}$. In each image, the partial lines with a sufficient signal level were analyzed to measure the axial and lateral resolution. When the wavelength was changed, the detection objective focus was manually adjusted to match the detection focal plane to the illumination light sheet.

Tissue imaging performance was evaluated by imaging formalin-fixed human anal tissues. The *ex vivo* tissue imaging protocol was reviewed and approved by the Stanford Internal Review Board. Index-matching gel (GenTeal Tears Gel, Alcon) was placed on the tissue surface, and a transparent plastic film (material = fluorinated ethylene propylene; refractive index = 1.34; thickness = $250 \mu\text{m}$) was placed on the tissue surface. The tissue was then placed under the sLSM setup, and additional index-matching gel was placed between the plastic film and the two objective lenses. The tissue surface was located $80 \mu\text{m}$ above the illumination focal point of 800 nm along the y -axis so that the illumination DOF for 800 nm , $\pm 80 \mu\text{m}$, was used to image the superficial region of the tissue. For each wavelength, twenty-five sLSM images were acquired, while the tissue was translated along the u -axis with a step size of $10 \mu\text{m}$. The exposure time of the CMOS sensor was set as 1 second. The illumination power on the tissue was 0.19 , 0.57 , 0.91 , and $1.51 \mu\text{W}$ for 500 , 600 , 700 , and 800 nm , respectively. The gain of the CMOS sensor was adaptively adjusted to provide a similar intensity level for all wavelengths.

2.4. Imaging depth analysis

The imaging depth was evaluated by i) using an edge contrast metric and ii) visual assessment by a pathologist. Since images of the squamous mucosa exhibited multiple layers of squamous cells throughout the epithelium, these images were used for the imaging depth analysis. A flowchart of the quantitative imaging depth analysis is shown in Fig. 4. Each image was convolved with a Gaussian filter with sigma of 5 pixels to reduce the speckle noise while maintaining the image contrast for epithelial cells. The Gaussian-filtered image was convolved with a Laplacian filter with a kernel size of $1(x) \times 21(y)$ pixels. The kernel size of 21 pixels was used because a typical cell-to-cell distance was $\sim 9 \mu\text{m}$ or ~ 20 pixels. The Laplacian filter was applied along the y -axis to disregard the intensity variation along the x -axis caused by shadowing effects (bright particles on the tissue surface reducing the intensity below). The Laplacian-filtered image was normalized by a smoothed image generated by convolution of the Gaussian-filtered image with an ones vector with a kernel size of $1(x) \times 21(y)$ pixels. The resulting image visualized edges along the vertical

direction. The edge-enhanced image was further divided into tall segments with a width of 100 pixels along the x-axis. For each segment, the edge contrast values were averaged along the x-axis at each y coordinate, which generated a curve showing the edge contrast as a function of depth. The contrast curve was fitted with an exponential decay function, $e^{-y/\alpha}$, with α being the decay factor in the unit of μm . The average and standard deviation of the decay factor were calculated for each wavelength.

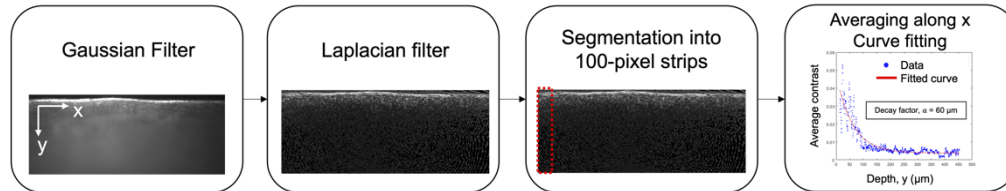


Fig. 4. Flowchart of the quantitative imaging depth analysis.

Visual assessment of the imaging depth was performed by a pathologist (EY). Each sLSM image was presented to the pathologist without any information about the wavelength used. For each wavelength, five sLSM images obtained from different tissue locations were used for the analysis. The images were presented to the pathologist in a random order for the wavelength and tissue location. Before being presented to the pathologist, the speckle noise of sLSM images was reduced by using a median filter in ImageJ (kernel radius = 2). Ten tick marks equally spaced along the x-axis were imposed on the top of each sLSM image, and the pathologist marked the deepest location where cellular details were observable at each tick marked x location. This resulted in 50 locations examined for each wavelength. The average and standard deviation of the visually-assessed imaging depth were calculated for each wavelength.

3. Results

3.1. Resolution measurement

The measured lateral and axial resolution for different wavelengths is shown in Fig. 5. The measured lateral resolution (Fig. 5(a)) was 1.06 μm , 1.20 μm , 1.37 μm , and 1.58 μm , for 500 nm, 600nm, 700nm, and 800nm, respectively. The lateral resolution was better for shorter wavelengths as expected. The difference between the measured and theoretical lateral resolution was small, 0.18-0.22 μm . The plot for the measured axial resolution (Fig. 5(b)) shows that the foci of the four wavelengths well coincide with each other. When the focus of the 800 nm light sheet was used as the reference, the measured axial resolution for 800 nm was 6.09 μm on average over the theoretical DOF of $\pm 80 \mu\text{m}$. The measured axial resolution was 5.04 μm , 5.55 μm , and 5.90 μm for 500 nm, 600 nm, and 700 nm over their respective theoretical DOF ($\pm 128 \mu\text{m}$, $\pm 107 \mu\text{m}$, and $\pm 91 \mu\text{m}$). The measured axial resolution was slightly larger than the target axial resolution, 5 μm , because of the dimensional errors in the 3D-printed apertures and aberrations of the illumination optics.

3.2. Tissue imaging results

Figure 6 shows representative sLSM and histologic images of the anal squamous mucosa. The sLSM images were processed for speckle noise reduction, by applying a gamma value of 0.7 and a median filter with a kernel radius of 2 pixels in ImageJ. In the superficial region of the sLSM images (epithelium or EP in Figs. 6(a)-(d)), layers of stratified squamous epithelial cells are visualized with hypo-reflective (dark) nuclei and hyper-reflective (bright) cytoplasm and cell membranes in a regular honeycomb pattern. The cellular features visualized in the sLSM images

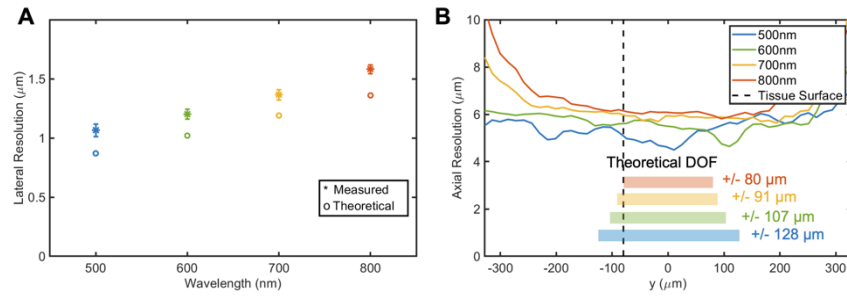


Fig. 5. Theoretical and measured lateral resolution as a function of wavelength (A) and measured axial resolution for different wavelengths as a function of y coordinate (B).

were similar to those shown in high-resolution (lateral resolution = 2 μm ; axial resolution = 1 μm) OCT images of the cervical epithelium [27], which is known to be histologically similar to the anal epithelium. The cell-to-cell distance in the sLSM images (insets, Figs. 6(a)-(d)) was similar to the distance shown in the histologic image of the same tissue (inset, Fig. 6(e)). Speckle noise is more noticeable in the sLSM images obtained with longer wavelengths, because the same spectral band of 40 nm was used for all the wavelengths, and the spectral averaging of the speckle noise was less effective for longer wavelengths. In deeper regions (lamina propria or LP in Figs. 6(a)-(d)), large and blurry hypo-reflective areas are noticed (arrows in Figs. 6(a)-(d)), which appear to correspond to blood vessels shown in the histologic image (arrow in Fig. 6(e)). The blood vessels were more easily observable in the sLSM images obtained with longer wavelengths.

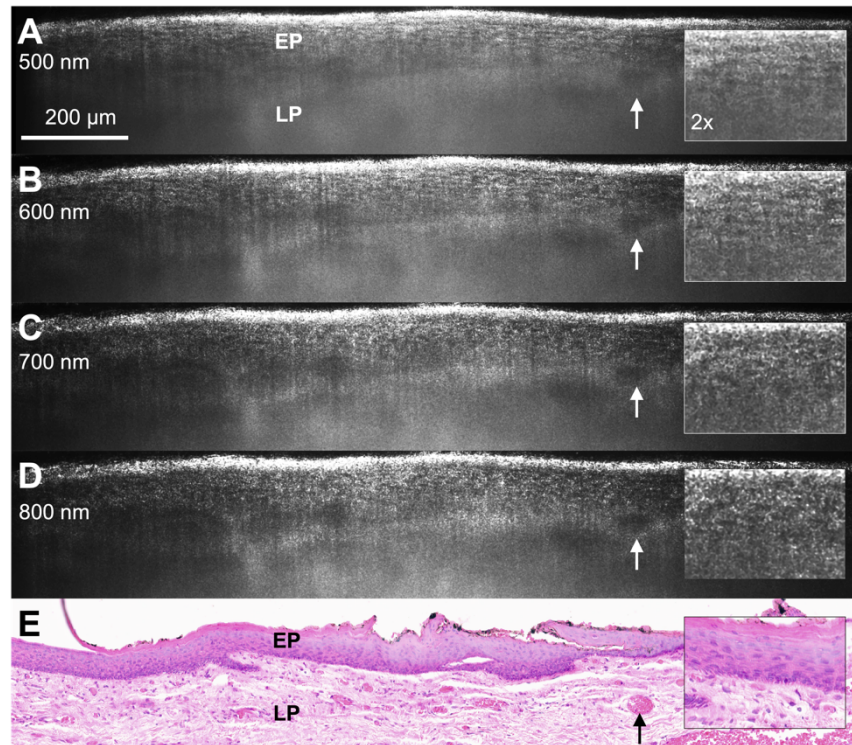


Fig. 6. sLSM (A-D) and histologic image (E) of the human anal squamous mucosa. EP – epithelium; LP – lamina propria; and arrows - blood vessel.

Figure 7 shows representative sLSM and histologic images of the anal columnar mucosa. The columnar epithelium (EP) was visualized as a hypo-reflective layer in sLSM images (Figs. 7(a)-(d)), which is consistent with the previous reflectance confocal microscopy studies of visualizing goblet cells in the columnar epithelium as hypo-reflective voids [28,29]. Crypts (asterisks) were visualized as dark openings in sLSM images. The junction between the epithelium and lamina propria exhibited a strong signal (arrows in Fig. 7(a)-(d)) in sLSM images, probably due to the light scattering by the basement membrane (arrow in Fig. 7(e)).

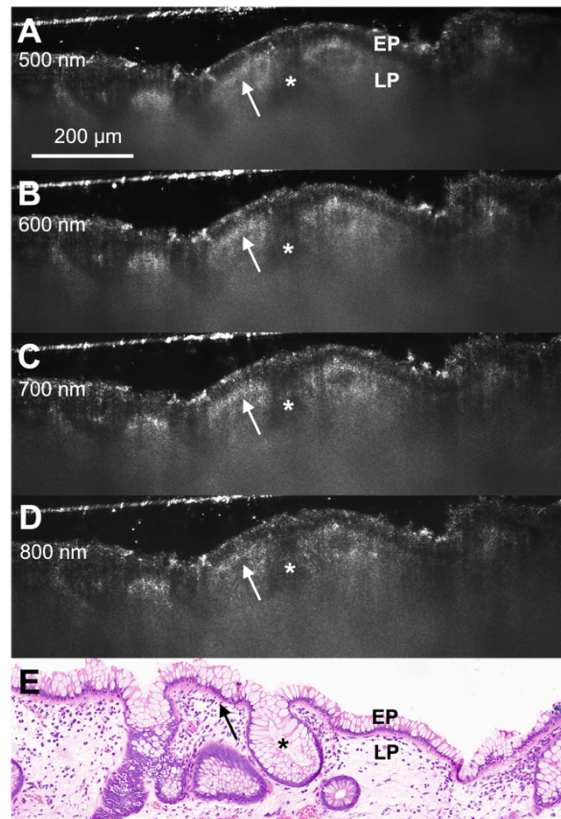


Fig. 7. sLSM (A-D) and histologic image (E) of the human anal columnar mucosa. asterisks – crypts; and arrows - junctions between the epithelium and lamina propria.

3.3. Analysis of imaging depth

Representative image contrast curves as a function of imaging depth for different wavelengths are shown in Fig. 8(a). The image contrast decreased as the imaging depth increased. Longer wavelengths showed a slower decrease of the image contrast. The image contrast was higher for longer wavelengths even in superficial imaging depths (left side of Fig. 8(a) curves). Multiply-scattered photons in shorter wavelengths can increase the background signal even at a shallow depth, which is noticeable as a reduced contrast between the hypo- and hyper- reflective regions in Fig. 6(a). The decay factors for different wavelengths are shown in Fig. 8(b). The decay factor increased as a function of wavelength, and the increase was most notable between 500 and 600 nm.

A representative sLSM image manually marked by the pathologist for the deepest imaging depth is shown in Fig. 9(a). The imaging depth and the corresponding tissue surface are marked

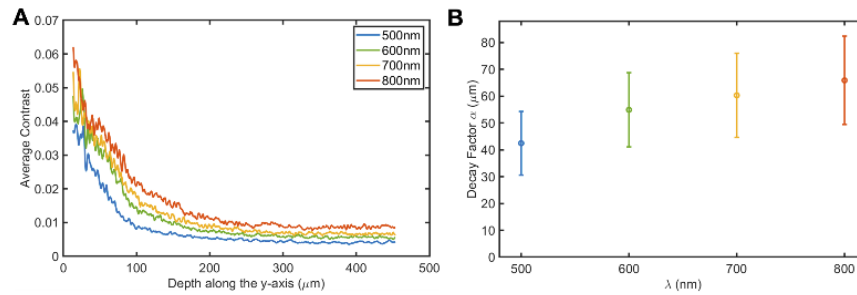


Fig. 8. Representative image contrast curves (A) and decay factors (B) for different wavelengths.

with red dots. The visually-assessed imaging depth (Fig. 9(b)) showed a similar trend to the quantitatively-calculated decay factor (Fig. 8(b)): the imaging depth increased as a function of wavelength. The visual assessment also showed that an imaging depth of 165–208 μm is useable for examining cellular details of the squamous epithelium.

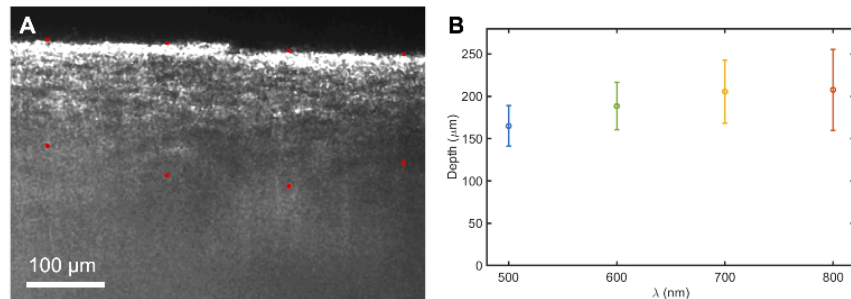


Fig. 9. Representative sLSM image with red markings for the tissue surface and the deepest tissue depth with visible cellular features (A) and visually-assessed imaging depths for different wavelengths (B).

4. Discussion

In summary, we developed a multi-wavelength sLSM setup to evaluate the sLSM imaging performance for different wavelengths. While we still needed to adjust the detection focus, such adjustment was not needed for the illumination optics thanks to the careful selection of the collimation lens. This facilitated imaging of the same tissue with different wavelengths, and enabled reliable comparisons of different wavelengths. An expensive, supercontinuum laser was used in the current sLSM setup because it delivered different wavelengths through a small-core fiber. However, once the optimal wavelength is determined for the specific tissue imaging application, a clinically-viable sLSM device can be developed using a much cheaper light source such as an LED. A relatively long exposure time, 1 second, was used due to the low illumination power, $<1.5 \mu\text{W}$. The exposure time can be significantly reduced in future sLSM devices with a single spectral band by optimizing the illumination optics, which can enable real-time imaging, as demonstrated in previous sLSM work [17].

One of the interesting findings was that cellular morphologic details can be visualized from formalin-fixed tissues. This is helpful because the same tissue can be used over time to evaluate different imaging conditions and modalities. Furthermore, there is an abundance of fixed tissue with histopathologic abnormalities that are discarded in the pathology lab after clinical evaluation

is complete. This is a rich source of tissue samples that are stable and readily available to the broader scientific community for optical image analysis. However, there is a caveat: fixed tissues might scatter differently than fresh tissues. A future study is needed for analyzing the scattering signal and the visualized cellular details of tissues before and after formalin fixation.

In sLSM images of the columnar mucosa, details of the columnar epithelial cells were not well visualized. This is because the homogenous internal structure of goblet cells did not generate a strong scattering signal. sLSM can be still useful in differentiating between the squamous mucosa and columnar mucosa, and in identifying the transformation zone.

Structures in the lamina propria such as blood vessels and crypts were visualized as hypo-reflective voids. However, the details of these structures were not clear due to the increased light sheet thickness and the resolution degradation at deeper tissue regions. While the capability to discern hypo-reflective structures in the lamina propria even with a degraded resolution could be potentially useful in identifying tumor nodules, its feasibility and utility need to be evaluated in future studies.

Longer wavelengths provided a larger imaging depth based on both the quantitative image contrast evaluation and the visual assessment by a pathologist. This is not surprising because longer wavelengths experience less scattering. However, the amount of increase in the imaging depth was most notable between 500 and 600 nm, and the increase was more moderate after 600 nm (Figs. 8 and 9). The visual assessment results show that 600 nm allows for the visualization of cellular details up to a depth of $\sim 200\ \mu\text{m}$, which can be useful in evaluating epithelial cellular morphologic changes in malignant diseases. Therefore, a wavelength around 600 nm can be used for further development of a clinically-viable sLSM device. The use of 600 nm, rather than a near-infrared wavelength around 800 nm, could either increase the light sheet length for the same axial resolution or improve the axial resolution for the same light sheet length. However, further studies will be needed for imaging fresh human tissues with different wavelengths to determine the optimal wavelength for the specific application.

Funding. National Institute of Biomedical Imaging and Bioengineering (R21EB030079).

Disclosures. The University of Arizona has a technology-licensing agreement with ArgosMD on the portable confocal microscopy technology. DK has the rights to receive royalties as a result of this licensing agreement. DK serves as a scientific advisor to ArgosMD.

Data availability. The data that support the findings of this study are available from the corresponding author upon reasonable request.

References

1. W. A. Wells, M. Thrall, A. Sorokina, J. Fine, S. Krishnamurthy, A. Haroon, B. Rao, M. M. Shevchuk, H. C. Wolfsen, G. J. Tearney, and L. P. Hariri, "In vivo and ex vivo microscopy: moving toward the integration of optical imaging technologies into pathology practice," *Arch. Pathol. Lab. Med.* **143**(3), 288–298 (2019).
2. M. Tavakoli, P. Hossain, and R. A. Malik, "Clinical applications of corneal confocal microscopy," *Clin. Ophthalmol.* **2**(2), 435–445 (2008).
3. S. González, K. Swindells, M. Rajadhyaksha, and A. Torres, "Changing paradigms in dermatology: confocal microscopy in clinical and surgical dermatology," *Clin. Dermatol.* **21**(5), 359–369 (2003).
4. R. Kiesslich, M. Goetz, M. Vieth, P. R. Galle, and M. F. Neurath, "Confocal laser endomicroscopy," *Gastrointest. Endosc. Clin. N. Am.* **15**(4), 715–731 (2005).
5. W. Drexler and J. G. Fujimoto, "State-of-the-art retinal optical coherence tomography," *Prog. Retin. Eye Res.* **27**(1), 45–88 (2008).
6. T.-H. Tsai, C. L. Leggett, A. J. Trindade, A. Sethi, A.-F. Swager, V. Joshi, J. J. Bergman, H. Mashimo, N. S. Nishioka, and E. Namati, "Optical coherence tomography in gastroenterology: a review and future outlook," *J. Biomed. Opt.* **22**(12), 1–17 (2017).
7. T. Yonetsu, B. E. Bouma, K. Kato, J. G. Fujimoto, and I.-K. Jang, "Optical coherence tomography," *Circ. J. advpub* **2**(1-2), 9–25 (2013).
8. E. Cinotti, L. Gergelé, J. L. Perrot, A. Dominé, B. Labeille, P. Borelli, and F. Cambazard, "Quantification of capillary blood cell flow using reflectance confocal microscopy," *Ski. Res. Technol.* **20**(3), 373–378 (2014).
9. L. E. Meyer, N. Oberg, W. Sterry, and J. Lademann, "In vivo confocal scanning laser microscopy: comparison of the reflectance and fluorescence mode by imaging human skin," *J. Biomed. Opt.* **11**(4), 044012 (2006).

10. G. Peterson, D. K. Zaroni, M. Ardigo, J. C. Migliacci, S. G. Patel, and M. Rajadhyaksha, "Feasibility of a video-mosaicking approach to extend the field-of-view for reflectance confocal microscopy in the oral cavity *in vivo*," *Lasers Surg. Med.* **51**(5), 439–451 (2019).
11. J. Welzel, "Optical coherence tomography in dermatology: a review," *Ski. Res. Technol.* **7**(1), 1–9 (2001).
12. R. A. Leitgeb, "En face optical coherence tomography: a technology review [Invited]," *Biomed. Opt. Express* **10**(5), 2177–2201 (2019).
13. L. Liu, J. A. Gardecki, S. K. Nadkarni, J. D. Toussaint, Y. Yagi, B. E. Bouma, and G. J. Tearney, "Imaging the subcellular structure of human coronary atherosclerosis using micro-optical coherence tomography," *Nat. Med.* **17**(8), 1010–1014 (2011).
14. A. Dubois, O. Levecq, H. Azimani, D. Siret, A. Barut, M. Suppa, V. del Marmol, J. Malveyh, E. Cinotti, P. Rubegni, and J.-L. Perrot, "Line-field confocal optical coherence tomography for high-resolution noninvasive imaging of skin tumors," *J. Biomed. Opt.* **23**(10), 1–9 (2018).
15. R. M. Power and J. Huiskens, "A guide to light-sheet fluorescence microscopy for multiscale imaging," *Nat. Methods* **14**(4), 360–373 (2017).
16. J. M. Girkin and M. T. Carvalho, "The light-sheet microscopy revolution," *J. Opt.* **20**(5), 053002 (2018).
17. C. D. Nguyen, P. K. O'Neal, N. Kulkarni, E. Yang, and D. Kang, "Scattering-based light-sheet microscopy for rapid cellular imaging of fresh tissue," *Lasers Surg. Med.* **53**(6), 872–879 (2021).
18. H. Siedentopf and R. Zsigmondy, "Über Sichtbarmachung und Größenbestimmung ultramikroskopischer Teilchen, mit besonderer Anwendung auf Goldrubingläser," *Ann. Phys.* **315**(1), 1–39 (1902).
19. Z. Yang, H. Downie, E. Rozbicki, L. X. Dupuy, and M. P. MacDonald, "Light Sheet Tomography (LST) for in situ imaging of plant roots," *Opt. Express* **21**(14), 16239–16247 (2013).
20. D. Di Battista, D. Merino, G. Zacharakis, P. Loza-Alvarez, and O. E. Olarte, "Enhanced light sheet elastic scattering microscopy by using a supercontinuum laser," *Methods Protoc.* **2**(3), 57 (2019).
21. M. Lin, X. Qiao, Q. Liu, C. Shao, and X. Su, "Light-sheet-based 2D light scattering cytometry for label-free characterization of senescent cells," *Biomed. Opt. Express* **7**(12), 5170–5181 (2016).
22. K. S. Nehal, D. Gareau, and M. Rajadhyaksha, "Skin imaging with reflectance confocal microscopy," in *Semin. Cutaneous Med. Surg.* (WB Saunders, 2008), pp. 37–43.
23. Y. Wang, J. S. Nelson, Z. Chen, B. J. Reiser, R. S. Chuck, and R. S. Windeler, "Optimal wavelength for ultrahigh-resolution optical coherence tomography," *Opt. Express* **11**(12), 1411–1417 (2003).
24. Y. Zhang and H. Gross, "Systematic design of microscope objectives. Part I: System review and analysis," *Adv. Opt. Technol.* **8**(5), 313–347 (2019).
25. P. Taroni, A. Pifferi, A. Torricelli, D. Comelli, and R. Cubeddu, "*In vivo* absorption and scattering spectroscopy of biological tissues," *Photochem. Photobiol. Sci.* **2**(2), 124–129 (2003).
26. S. L. Jacques, "Optical properties of biological tissues: a review," *Phys. Med. Biol.* **58**(11), R37–R61 (2013).
27. H. M. Leung, M. L. Wang, H. Osman, E. Abouei, C. MacAulay, M. Follen, J. A. Gardecki, and G. J. Tearney, "Imaging intracellular motion with dynamic micro-optical coherence tomography," *Biomed. Opt. Express* **11**(5), 2768–2778 (2020).
28. D. Kang, M. J. Suter, C. Boudoux, H. Yoo, P. S. Yachimski, W. P. Puricelli, N. S. Nishioka, M. Mino-Kenudson, G. Y. Lauwers, B. E. Bouma, and G. J. Tearney, "Comprehensive imaging of gastroesophageal biopsy samples by spectrally encoded confocal microscopy," *Gastrointest. Endosc.* **71**(1), 35–43 (2010).
29. D. Kang, S. C. Schlachter, R. W. Carruth, M. Kim, T. Wu, N. Tabatabaei, A. R. Soomro, C. N. Grant, M. Rosenberg, N. S. Nishioka, and G. J. Tearney, "Large-area spectrally encoded confocal endomicroscopy of the human esophagus *in vivo*," *Lasers Surg. Med.* **49**(3), 233–239 (2017).

Appendix B

Speckle and Shadow Artifacts Reduction Method

This section includes the conference paper about the speckle and shadow artifacts reduction method for sLSM. The publication can be found at the Optica Publishing Group. The full citation is listed below.

J. Zhao, B. Liang, E. Dobo, M. J. Khan, E. Yang, and D. Kang, "Speckle and Shadow Artifacts Reduction in Scattering-Based Light Sheet Microscopy," in Biophotonics Congress: Optics in the Life Sciences 2023 (OMA, NTM, BODA, OMP, BRAIN), Technical Digest Series (Optica Publishing Group, 2023), paper DTu2A.3.

Speckle and Shadow Artifacts Reduction in Scattering-Based Light Sheet Microscopy

J. Zhao¹, B. Liang², E. Dobo², M. J. Khan², E. Yang², D. Kang^{1,3,*}

¹James C. Wyant College of Optical Sciences, University of Arizona, Tucson, Arizona, 85721, USA.

²School of Medicine, Stanford University, Stanford, California, 94305, USA.

³Department of Biomedical Engineering, University of Arizona, Tucson, Arizona, 85721, USA.

*dkkang@email.arizona.edu

Abstract: Scattering-based light sheet microscopy (sLSM) using a laser had challenges with speckle noise and shadow artifacts. We developed an LED-based sLSM setup that significantly reduces speckle noise and shadow artifacts. © 2023 The Author(s)

1. Introduction

Scattering-based light sheet microscopy (sLSM) can conduct microscopy imaging of unstained tissues at high resolution (1-2 μm) over a large field-of-view (a few mm) [1]. However, the previous sLSM setup suffered from two issues, speckle noise and shadow artifacts, which can significantly degrade the image quality and make it challenging to appreciate cellular morphologic details. Speckle noise is caused by the random interference of scattered coherent light and manifested as high-contrast random granular patterns [2]. Shadow artifacts are dark stripes generated by bright particles attenuating the illumination power below the particle [3]. The previous sLSM setup generated the illumination light sheet by focusing collimated laser light with a cylindrical lens into a single line. The use of laser light with high spatial coherence caused noticeable speckle noise even when a relatively large bandwidth of 40 nm was used for sLSM. The previous illumination optics of using a cylindrical lens resulted in parallel illumination with a small angular divergence along the light sheet width direction, which made the shadow artifacts prominent [1]. In this paper, we present the development of an LED-based sLSM setup that reduces speckle noise and shadow artifacts.

2. Methods

The LED-based sLSM setup is shown in Fig. 1a. Light from a high-power LED (center wavelength = 640 nm; bandwidth = 25 nm) was filtered by a slit (width = 5 μm ; length = 3 mm). The illumination light sheet was generated by imaging the slit onto the sample by two objective lenses: 5x objective ($f_1 = 40$ mm; NA = 0.15; dry) and 10x objective ($f_2 = 20$ mm; NA = 0.3; water immersion), resulting in a magnification of 0.5. A 3D-printed aperture (length \times width = 10 mm \times 2.6 mm) was placed in front of the second objective lens to generate the desired light sheet thickness of ~ 5 μm . The LED had low spatial and temporal coherence, which produced low speckle noise. With this illumination method, each point of the tissue was illuminated with multiple angles in the xy-plane. Therefore, even when a bright particle is present in the tissue, it does not completely block the illumination light below the particle, which reduces the shadow artifacts. In the detection path (Fig. 1b), a second objective lens ($f_2 = 20$ mm; NA = 0.3; water immersion) collected the light scattered from the tissue. A camera lens ($f = 85$ mm; F/2) focused light onto a monochromatic CMOS sensor (acA4024-29um, Basler; 4,024 \times 3,036 pixels; pixel size = 1.85 μm). The resulting pixel size in the tissue space was 0.44 μm , and the field of view was 1.5 mm.

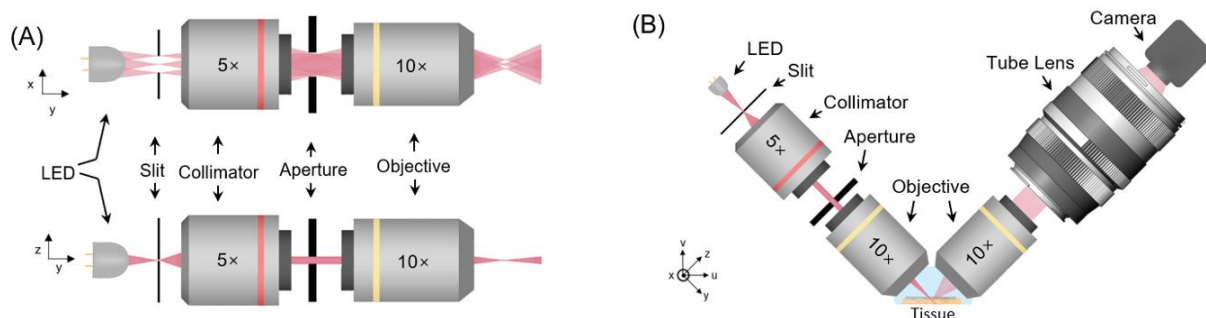


Fig. 1. Schematic diagram of (A) the illumination optics and (B) the sLSM setup.

We imaged formalin-fixed human anal tissues with the LED-based sLSM setup and the previous laser-based sLSM setup (center wavelength = 600 nm; bandwidth = 40 nm). [1]. A fluorinated ethylene propylene (FEP;

refractive index = 1.34) film was placed on top of the tissue to flatten the tissue surface. Index-matching gel (refractive index = 1.34) was used to fill the gaps between the objectives, the FEP film, and the tissue.

3. Results

Fig. 2 shows representative sLSM images of human anal tissue acquired with the previous laser-based sLSM setup [1] and the present LED-based sLSM setup. The speckle noise was significantly reduced in the image obtained with the LED-based sLSM setup (insets, Figs. 2a,b). Shadow artifacts were readily visible as dark, vertical stripes below the tissue surface in the image obtained with the laser-based sLSM setup (Fig. 2a) but were not noticeable in the image obtained with the LED-based sLSM system (Fig. 2b). As a result, the squamous epithelial cells were more clearly visualized with the characteristic honeycomb pattern in the image obtained with the LED-based sLSM setup.

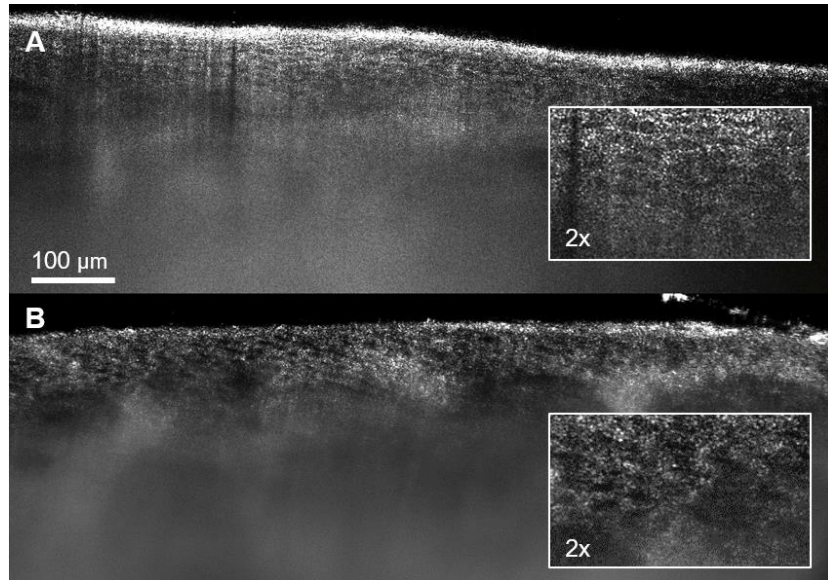


Fig. 2 Representative sLSM images of formalin-fixed human anal tissue acquired with (A) laser-based sLSM and (B) LED-based sLSM.

4. Conclusion

We developed an LED-based sLSM setup that reduces speckle noise and shadow artifacts. Preliminary images of formalin fixed human anal tissues showed that the LED-based sLSM setup significantly reduced speckle noise and shadow artifacts, making cellular features much easier to appreciate. In the future, we will build a low-cost, handheld sLSM device based on the LED-based sLSM approach.

5. Acknowledgement

Research reported in this publication was supported by the National Institute Of Biomedical Imaging And Bioengineering of the National Institutes of Health under Award Number R21EB030079. The content is solely the responsibility of the authors and does not necessarily represent the official views of the National Institutes of Health. The University of Arizona has a technology-licensing agreement with ArgosMD on the portable confocal microscopy technology. DK has the rights to receive royalties as a result of this licensing agreement. DK serves as a scientific advisor to ArgosMD.

6. References

- [1] Jingwei Zhao, Nachiket Kulkarni, Erika Dobo, Michelle J. Khan, Eric Yang, and Dongkyun Kang, "Investigation of different wavelengths for scattering-based light sheet microscopy," *Biomed. Opt. Express* 13, 3882-3892 (2022)
- [2] J. W. Goodman, "Speckle Phenomena in Optics: Theory and Applications," in (2020).
- [3] P. Ricci, V. Gavryusev, C. Müllenbroich, L. Turrini, G. de Vito, L. Silvestri, G. Sancataldo, and F. S. Pavone, "Removing striping artifacts in light-sheet fluorescence microscopy: a review," *Prog. Biophys. Mol. Biol.* 168, 52–65 (2022).

Appendix C

Custom sLSM Probe

Details of the custom objective lens are presented in this section, including the lens prescription, tolerance analysis data, and other performance metrics. The result of human finger tissue imaging *in vivo* with the sLSM probe is also presented to demonstrate the *in vivo* imaging capability.

The MTF plot of the custom objective lens is shown in Fig. C.1 (a). The through-focus spot diagram of the custom objective lens within the light sheet thickness range is shown in Fig. C.1(b).

The tolerance analysis was conducted based on the lens manufacturing capability of Diverse Optics (as shown in C.3) and the 3D-printed holder error ($0.05mm$). Two 3D-printed holders, designed for aligning the custom objective lens, were tightly fitted with the lens and had a smooth fit with each other. Two compensators are the lens-to-lens distance and the working distance.

The *in vivo* imaging capability of the probe was tested on the fingerprint area of the fifth metacarpal of a human subject. The finger was directly put under the sLSM probe with immersion medium filling the gap between the finger and the sLSM. As shown in Fig. C.3,

keratinized epidermal cells are shown on the left half of the image, and the helical patterns of sweat glands are clearly visible indicated by the yellow dotted regions.

Table C.1: Custom objective lens prescription (part 1)

Surf Glass	Type Clear Semi-Diam	Radius Mech Semi-Diam	Thickness
OBJ	STANDARD Inf	Inf Inf	Inf
STOP	STANDARD 3.68	INF 3.68	0
2 PMMA	EVEN ASPHERE 4.0	5.10 4.0	5.00
3	STANDARD 3.10	86.8 4.0	3.00
4 PMMA	EVEN ASPHERE 2.3	-11.5 2.3	2.86
5 WATER	STANDARD 1.54	4.67 2.3	5.17
IMG WATER	STANDARD 1.02	Inf 2.3	

Table C.2: Custom objective lens prescription (part 2)

Surf 6th Order	Type 8th Orderm	Conic	4th Order
2	EVEN ASPHERE	-2.62	2.17e-3
-3.13e-5	1.03e-6		
4	EVEN ASPHERE	-3.53	-4.65e-3
7.55e-5	-2.15e-5		

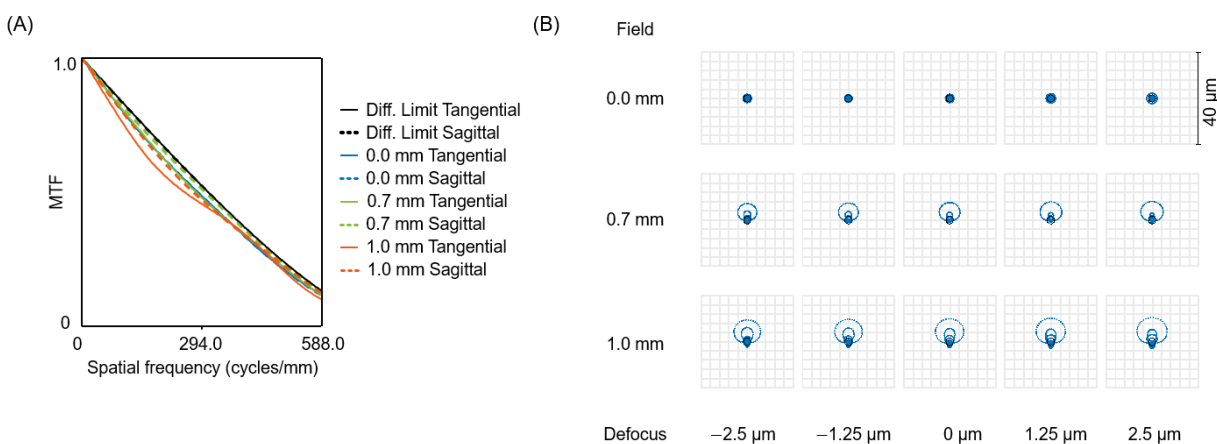


Figure C.1: Custom objective lens performance: (a) MTF vs. spatial frequency. The cutoff frequency is set at the Nyquist frequency determined by the CMOS sensor, 588 cycles/mm; (b) Spot diagram for each field. Black circle: Airy disk.

Table C.3: Diverse Optics tolerance table

Parameter	Error (Precision)
Polymer quality (Nd)	$> \pm 0.001$
Radius	$> \pm 0.1\%$
Diameter (mm)	$> + 0.000 / - 0.025$
Irregularities for 25 mm diameter max (fringes)	> 0.5
Centering (arc min)	> 1

Table C.4: Custom objective lens tolerance yield

Yield	RMS wavefront error
98%	> 0.120
90%	> 0.093
80%	> 0.073
50%	> 0.042
20%	> 0.021
10%	> 0.016
2%	> 0.012

	Type			Nominal			Comment
1	COMP ▾	6	0	3.000000	-3.000000	3.000000	
2	COMP ▾	12	0	5.167467	-3.000000	3.000000	Default compensator on lens separati...
3	TWAV ▾				0.632800		Default test wavelength.
4	TOFF ▾						Lens 2
5	TRAD ▾	3	0	5.099963	-5.000000E-03	5.000000E-03	Power tolerance. Diverse Optics
6	TRAD ▾	6	0	86.8115...	-0.087000	0.087000	
7	TSDI ▾	3		3.789680	-0.025000	0.000000	Semi-diameter
8	TSDI ▾	6		2.922093	-0.025000	0.000000	
9	TIRR ▾	3		0.000000	0.000000	0.160000	Irregularities
10	TIRR ▾	6		0.000000	0.000000	0.125000	Irregularities
11	TIND ▾	3		1.491756	-1.000000E-03	1.000000E-03	Diverse Optics: +/-0.001
12	TUTX ▾	2		0.000000	-0.016700	0.016700	
13	TUTY ▾	2		0.000000	-0.016700	0.016700	
14	TUTX ▾	5		0.000000	-0.016700	0.016700	
15	TUTY ▾	5		0.000000	-0.016700	0.016700	
16	TIND ▾	9		1.491756	-1.000000E-03	1.000000E-03	Default index tolerances.
17	TEDR ▾	8	13	0.000000	0.000000	0.025000	
18	TOFF ▾						
19	TOFF ▾						Lens 1
20	TRAD ▾	9	0	-11.485...	-0.011000	0.011000	Default radius tolerances.
21	TRAD ▾	12	0	4.666463	-4.000000E-03	4.000000E-03	Default radius tolerances.
22	TSDI ▾	9		1.919814	-0.025000	0.000000	Semi-diameter
23	TSDI ▾	12		1.505585	-0.025000	0.000000	
24	TIRR ▾	9		0.000000	0.000000	0.080000	Irregularities
25	TIRR ▾	12		0.000000	0.000000	0.060000	Irregularities
26	TEDR ▾	2	7	0.000000	0.000000	0.025000	
27	TUTX ▾	11		0.000000	-0.016700	0.016700	
28	TUTY ▾	11		0.000000	-0.016700	0.016700	
29	TUTX ▾	8		0.000000	-0.016700	0.016700	
30	TUTY ▾	8		0.000000	-0.016700	0.016700	

Figure C.2: Custom objective lens tolerance analysis setting

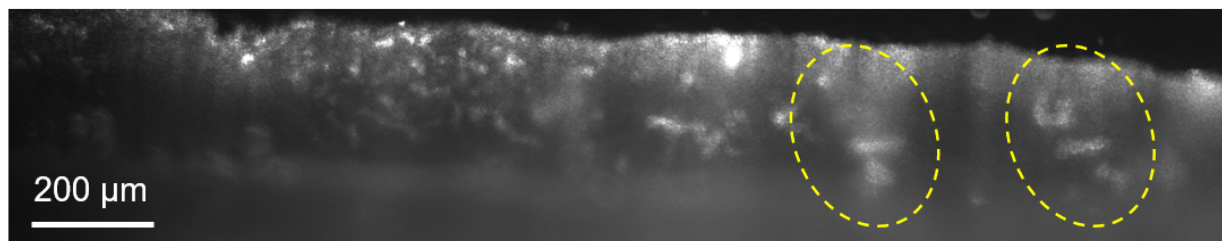


Figure C.3: sLSM images of human finger tissues. Circles: sweat glands with helical pattern.

Appendix D

Other Projects

This section includes the published manuscripts for two other projects I involved in during my PhD program: 1) Deep learning-based denoising in high-speed portable reflectance confocal microscopy, and 2) Handheld cross-polarised microscope for imaging individual pigmented cells in human skin *in vivo*. The abstract of each manuscript is presented below:

(1) Deep learning-based denoising in high-speed portable reflectance confocal microscopy

Portable confocal microscopy (PCM) is a low-cost RCM technique that can visualize cellular details of human skin *in vivo*. When PCM images are acquired with a short exposure time to reduce motion blur and enable real-time 3D imaging, the signal-to-noise ratio (SNR) is decreased significantly, which poses challenges in reliably analyzing cellular features. In this paper, we evaluated deep learning (DL)-based approach for reducing noise in PCM images acquired with a short exposure time. Results from the quantitative and qualitative evaluations showed that the DL-based approach significantly reduced noise presented in input images. The DL-based approach provided better denoising performance than non-DL filtering methods.

(2) Handheld cross-polarised microscope for imaging individual pigmented cells in human skin *in vivo*

We present the development of a simple, handheld cross-polarised microscope (CPM) and demonstration of imaging individual pigmented cells in human skin *in vivo*. In the CPM device, the cross-polarised detection approach is used to reduce the specular reflection from the skin surface and preferentially detect multiply-scattered light. The multiply-scattered light works as back illumination from within the tissue towards the skin surface, and superficial pigment such as intraepidermal melanin absorbs some spectral bands of the multiply-scattered light and cast coloured shadows. Since the light that interacted with the superficial pigment only needs to travel a short distance before it exits the skin surface, microscopic details of the pigment can be preserved. The CPM device uses a water-immersion objective lens with a high numerical aperture to image the microscopic details with minimal spherical aberrations and a small depth of focus. Preliminary results from a pilot study of imaging skin lesions *in vivo* showed that the CPM device could reveal three-dimensional distribution of pigmented cells and intracellular distribution of pigment. Co-registered CPM and reflectance confocal microscopy images showed good correspondence between dark, brown cells in CPM images and bright, melanin-containing cells in reflectance confocal microscopy images.

Deep Learning-Based Denoising in High-Speed Portable Reflectance Confocal Microscopy

Jingwei Zhao, BS,¹ Manu Jain, MD,² Ucalene G. Harris, BS,² Kivanc Kose, PhD ²,
Clara Curiel-Lewandrowski, MD,³ and Dongkyun Kang, PhD ^{1,3,4*}

¹College of Optical Sciences, University of Arizona, Tucson, Arizona 85721

²Dermatology Service, Memorial Sloan Kettering Cancer Center, New York, New York 10021

³University of Arizona Cancer Center, Tucson, Arizona 85721

⁴Department of Biomedical Engineering, University of Arizona, Tucson, Arizona 85721

Background and Objective: Portable confocal microscopy (PCM) is a low-cost reflectance confocal microscopy technique that can visualize cellular details of human skin *in vivo*. When PCM images are acquired with a short exposure time to reduce motion blur and enable real-time 3D imaging, the signal-to-noise ratio (SNR) is decreased significantly, which poses challenges in reliably analyzing cellular features. In this paper, we evaluated deep learning (DL)-based approach for reducing noise in PCM images acquired with a short exposure time.

Study Design/Materials and Methods: Content-aware image restoration (CARE) network was trained with pairs of low-SNR input and high-SNR ground truth PCM images obtained from 309 distinctive regions of interest (ROIs). Low-SNR input images were acquired from human skin *in vivo* at the imaging speed of 180 frames/second. The high-SNR ground truth images were generated by registering 30 low-SNR input images obtained from the same ROI and summing them. The CARE network was trained using the Google Colaboratory Pro platform. The denoising performance of the trained CARE network was quantitatively and qualitatively evaluated by using image pairs from 45 unseen ROIs.

Results: CARE denoising improved the image quality significantly, increasing similarity with the ground truth image by 1.9 times, reducing noise by 2.35 times, and increasing SNR by 7.4 dB. Banding noise, prominent in input images, was significantly reduced in CARE denoised images. CARE denoising provided quantitatively and qualitatively better noise reduction than non-DL filtering methods. Qualitative image assessment by three confocal readers showed that CARE denoised images exhibited negligible noise more often than input images and non-DL filtered images.

Conclusions: Results showed the potential of using a DL-based method for denoising PCM images obtained at a high imaging speed. The DL-based denoising method needs to be further trained and tested for PCM images obtained from disease-suspicious skin lesions. Lasers Surg. Med. © 2021 Wiley Periodicals LLC

Key words: reflectance confocal microscopy (RCM);

portable confocal microscopy (PCM); deep learning (DL); content-aware image restoration (CARE); image denoising

INTRODUCTION

Reflectance confocal microscopy (RCM) is an optical microscopy method that can non-invasively examine cellular details of human skin [1,2]. Through numerous clinical studies, RCM was shown to provide high diagnostic accuracy for the most common skin cancers. Recently, RCM was granted common procedural technology (CPT) reimbursement codes [3]. RCM has also been shown promising in imaging cellular details of other organs, such as oral cavity and esophagus [4,5]. Widespread clinical adoption of RCM, however, has been hampered partly by the high cost of the commercial RCM devices (~\$100,000).

Recently, we have developed low-cost (material cost = ~\$5,000), portable confocal microscopy (PCM) devices [6,7], and demonstrated confocal imaging of human skin *in vivo* [8]. PCM employs a broadband LED source and diffraction gratings to acquire two-dimensional confocal images without laser beam scanning [6]. PCM obviates the need for expensive optoelectrical components used in conventional RCM devices (e.g., high-speed beam scanners, fast data acquisition unit) but uses a consumer-grade CMOS sensor to acquire confocal images.

Conflict of Interest Disclosures: All authors have completed and submitted the ICMJE Form for Disclosure of Potential Conflicts of Interest and have disclosed the following: DK is an inventor of US patent applications (University of Arizona, assignee) on the portable confocal microscopy hardware. The University of Arizona has a technology-licensing agreement with ArgosMD on the portable confocal microscopy hardware. DK has the right to receive royalties as a result of this licensing agreement. DK serves as a scientific advisor to ArgosMD.

*Correspondence to: Dongkyun Kang, PhD, University of Arizona, 1630 E University Blvd, 621, Tucson, AZ 85721.

E-mail: dkkang@email.arizona.edu

Received 11 November 2020; revised 24 February 2021;

Accepted 1 April 2021

Published online 23 April 2021 in Wiley Online Library

(wileyonlinelibrary.com).

DOI 10.1002/lsm.23410

The imaging speed of PCM can be made high since it is primarily determined by the speed of the CMOS sensor rather than by the mechanical bandwidth of beam scanners as in conventional RCM. High imaging speed is desirable for PCM to reduce motion blur and enable real-time 3D imaging. However, PCM images obtained at a high imaging speed are prone to a low signal-to-noise ratio (SNR) since the corresponding short exposure time reduces the signal level.

One possible approach to enable high-speed, high-SNR PCM imaging is to first acquire images with low SNR and then improve SNR computationally. Recently, deep learning (DL)-based methods have been developed to improve SNR in microscopy images. One such DL-based method is content-aware image restoration (CARE) [9]. CARE was previously used for denoising fluorescence microscopy images acquired with a short exposure time and outperformed several commonly used, non-DL filtering methods [10–12]. CARE, however, is a supervised learning method and requires pairs of low-SNR input and high-SNR ground truth images obtained from the same region of interest (ROI). Noise2noise is another DL-based method that does not require high-SNR ground truth images but uses pairs of two different low-SNR images obtained from the same ROI [13]. Noise2void takes this approach one step further to just use a single low-SNR image for each ROI [14]. However, when pairs of low- and high-SNR images are obtainable, supervised learning methods, such as CARE, provide better denoising performance than noise2noise or noise2void [14].

In this paper, we evaluated the feasibility of using the CARE denoising approach on PCM images obtained with a short exposure time. We developed a method for generating pairs of a low-SNR input image and a high-SNR ground truth image of human skin *in vivo*. The CARE network was trained and evaluated quantitatively and qualitatively. Denoising performance of CARE was compared with that of non-DL filtering methods. CARE denoised images were qualitatively evaluated by confocal readers.

MATERIALS AND METHODS

High-Speed PCM Image Data Collection

Details of the PCM device were previously presented [7]. Briefly, the PCM device used an LED (central wavelength

of 820 nm; bandwidth = 40 nm) and a water-immersion objective lens ($\times 40$; numerical aperture = 0.8). Two-dimensional confocal images were captured by a high-speed CMOS sensor (1280×1024 pixels; pixel size = $4.8 \mu\text{m}$). Image data were transferred to a laptop (Surface Book; Microsoft) via a USB 3.0 cable. Illumination power on the tissue was 0.16 mW, and the measured resolution was 1.6 and $6.0 \mu\text{m}$ along the lateral and axial directions, respectively.

Confocal images were collected from normal human skin *in vivo* (Fig. 1). A custom 3D-printed cap was placed on the objective lens and filled with an index-matching gel. A transparent plastic disk (thickness = $250 \mu\text{m}$) was attached to the distal end of the 3D-printed cap. A drop of water was placed on the skin, and the PCM device was gently placed on the skin. Dimensions of the 3D-printed cap were designed in such a way that the PCM imaging plane was located around the dermal-epidermal junction (DEJ) when the PCM device was gently placed on the skin. The imaging depth was adjusted by changing the pressure on the skin.

The exposure time of the CMOS sensor was set as 5.4 milliseconds. Corresponding imaging speed was 180 frames/second, which was the maximum speed of the CMOS sensor when 10-bit digitization was used. One out of every six acquired images was displayed at the rate of 30 frames/second using a custom LabVIEW code. A set of 30 PCM images was acquired from each ROI while the PCM device was held stationary on the skin. Each image set was saved as an AVI file in the Y800 uncompressed grayscale format. A total of 354 image sets were acquired from distinctive ROIs from a single subject with lightly pigmented skin (Fitzpatrick's phototype III). A similar number of image sets were acquired from the three superficial skin layers, 123 sets from the epidermis, 133 from the DEJ, and 98 from the dermis.

Ground Truth Image Generation

Training of the CARE network required numerous pairs of a low-SNR input image and a high-SNR ground truth image. The high-SNR, ground truth image for each ROI was generated by summing 30 low-SNR PCM images obtained from the same ROI. While efforts were made to hold the PCM device stationary on the skin,

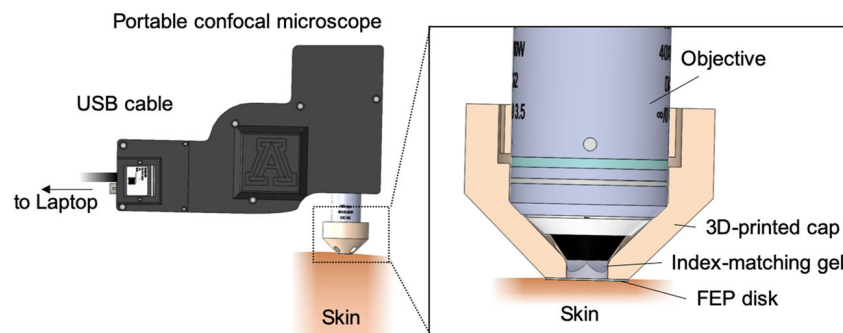


Fig. 1. Schematic of PCM imaging of human skin *in vivo*. PCM, portable confocal microscopy

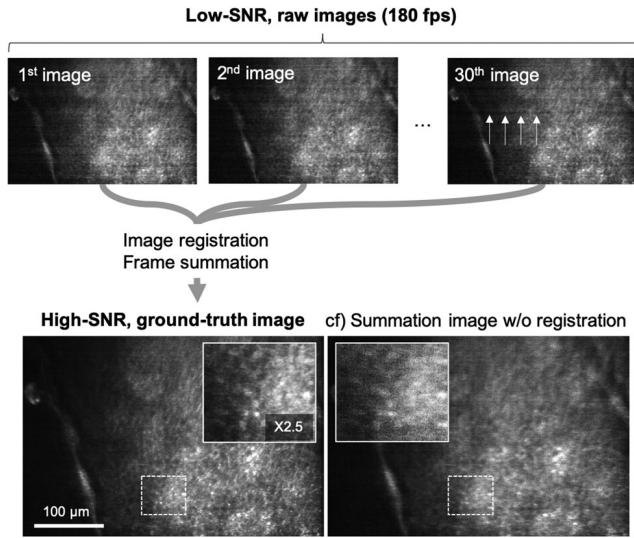


Fig. 2. Schematic of generating the high-SNR, ground truth image. Arrows—banding noise present on the raw image. SNR, signal-to-noise ratio

there still was a microscopic drift of the PCM device. The 30 PCM images were spatially registered by using an intensity-based registration method (imregister function, Matlab). The first image was used as the reference image, and translation was used as the transformation method. The root-mean-square (RMS) value of spatial drifts between 30 low-SNR images was calculated. The spatial drift RMS value ranged from 0.05 to 4.45 μm with an average of 1.22 μm and a standard deviation of 0.73 μm .

Figure 2 shows representative low-SNR PCM images and corresponding high-SNR ground truth images. The low-SNR PCM images exhibited noticeable banding noise

(arrows, top right). Banding noise had a random magnitude and spatial distribution in each low-SNR image, which made it challenging to remove banding noise using a traditional filtering method. In the ground truth image (left bottom), banding noise was significantly reduced. We compared the ground truth image to a summation image without the image registration step (right bottom). While the no-registration, summation image also significantly reduced banding noise, cellular details were not as sharp as those shown in the ground truth image (insets). The low-SNR images after the spatial registration and high-SNR ground truth images were cropped to an image size of 896 \times 600 pixels (430 \times 288 μm), where cellular features were readily observable in ground truth images. All images were saved in the TIFF format without any image compression.

CARE Network Training

We have selected the CARE network for denoising PCM images based on its successful demonstration of denoising fluorescence microscopy images [9] and images obtained by other microscopy modalities [15,16]. The CARE architecture is based on u-Net [17], where symmetric encoding and decoding layers are used in conjunction with skip connections. In CARE, the network predicts intensity probability function for each pixel as a Laplace distribution, and the location parameter of the Laplace distribution is used as the pixel intensity value in the denoised image [9]. Particular CARE network structure used for PCM denoising is shown in Figure 3. The initial number of features was set as 32, encoding depth 3, and convolution kernel size 5 \times 5. We utilized the Google Collaboratory implementation of the CARE network, ZeroCostDL4Mic [18]. Python 3.6 was used for the network training along with the Tensorflow 1.15.2 platform and Keras 2.1.2 library. Pairs of low-SNR input images

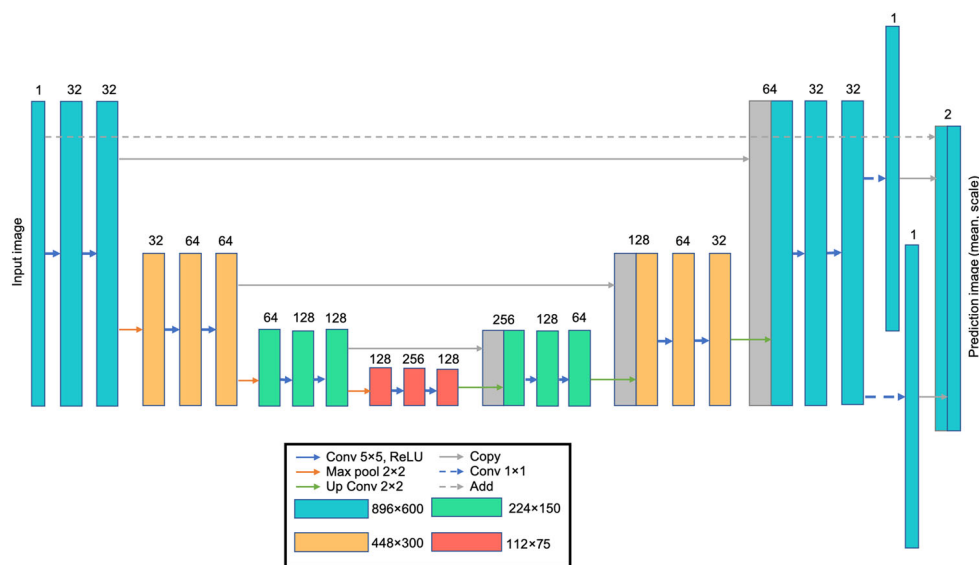


Fig. 3. CARE network structure trained for PCM denoising. CARE, content-aware image restoration; PCM, portable confocal microscopy.

and high-SNR ground truth images from 309 ROIs were used to train the network. Among the 309 ROIs, 108 were from the epidermis, 118 from the DEJ, and 83 from the dermis.

The training condition was set as follows: patch size = 80×80 pixels, number of patches = 77 per image, batch size = 8, number of steps per epoch = 400, number of epochs = 150, and initial learning rate = 0.0004. The learning rate was adjusted with a multiplication factor of 0.5 and patience of 10 epochs. 90% of the training set was used for training, and the remaining 10% was excluded from training and used to calculate the validation loss. The validation set was generated based on random sampling at the beginning of the training. For an exemplary training condition of using one low-SNR image per each of the 309 ROIs, a total of 23,793 image patch pairs were generated, and 21,414 patch pairs were used for training, and 2,379 for validation. Each patch was generated by random cropping of the image and normalized based on the intensity histogram. During normalization, reference percentiles for low and high intensities were randomly selected from uniform distributions of 1 to 3% and 99.5 to 99.9%, respectively. We initially trained the network with a large number of steps per epoch to expose the CARE network to the entire training set during each epoch. However, this approach frequently resulted in overfitting, where the validation loss became significantly larger than the training loss. We iteratively adjusted the number of steps per epoch and found that 400 provided similarly low loss values for the training and validation sets.

In the first set of network training, we trained the network with only one low-SNR image for each ROI, which resulted in 309 image pairs. As mentioned previously, 30 low-SNR images were acquired for each ROI. These 30 images exhibited different noise patterns but shared the same ground truth image. Using all 30 low-SNR images from each ROI might provide better training results than using just one low-SNR image. However, due to the limit on the available memory of the Google Colaboratory Pro platform, 25 GB, up to 10 low-SNR images for each of the 309 ROIs were reliably mountable. In the second set of network training, we used 10 image pairs for each ROI, resulting in 3090 image pairs. The 10 low-SNR images were composed of the first low-SNR image that

was used as the reference image during the image registration and 9 subsequent low-SNR images that were spatially registered to the first low-SNR image. The 10 image pairs shared the same ground truth image. For each of the two training conditions (1 image pair/ROI and 10 image pairs/ROI), we trained 5 models with different random starting weights to evaluate the performance variation between the trained models.

Denoising Performance Evaluation

Denoising performance was evaluated by using image pairs obtained from 45 ROIs that were not used during training or validation. Among the 45 ROIs in the test set, 15 ROIs were from the epidermis, 15 from the DEJ, and 15 from the dermis. Each ROI contained 30 low-SNR input images, among which the first image was used as the reference image, and the remaining 29 images were spatially registered to the first image. One ground truth image was generated by summing the 30 spatially registered images and was used in pair with all 30 spatially registered, low-SNR images. This resulted in a total of 1350 image pairs for the test set. A CARE denoised image was generated for each low-SNR input image. Standard image quality metrics were calculated for the input versus ground truth images and for the CARE denoised vs. ground truth images. Before calculating the image quality metrics, the ground truth image was normalized based on the 0.1% and 99.9% values of the intensity histogram. The input and CARE denoised images were then normalized respectively to produce the least amount of mean squared error (MSE) with the ground truth image. Structural similarity (SSIM) maps were generated [19], and the mean value of each SSIM map (mSSIM) was calculated. Normalized root mean squared error (NRMSE) and peak signal-to-noise ratio (PSNR) were also calculated. For each CARE network model, the three image quality metrics (mSSIM, NRMSE, and PSNR) were evaluated for the 1350 image pairs, and the average value of each quality metric was calculated.

Once the network model with the best denoising performance was determined, the network was also evaluated for denoising images obtained from a subject with darkly pigmented skin (phototype V) and images from the

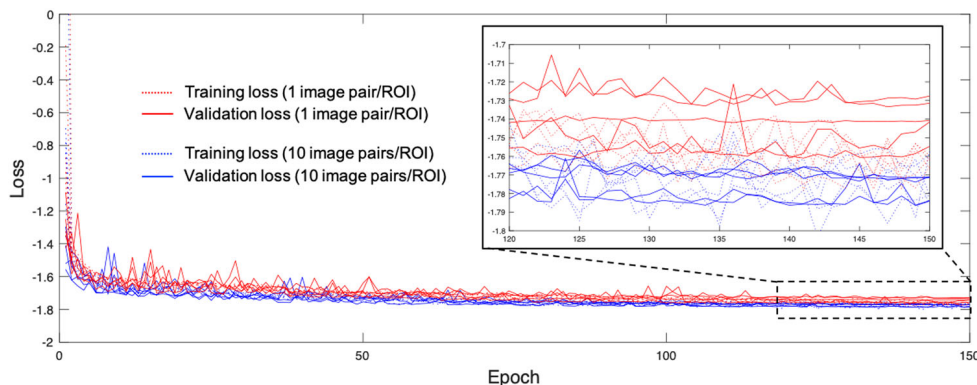


Fig. 4. Training and validation loss curves for 10 different models.

TABLE 1. Training and Test Results of the CARE Training for Denoising PCM Images

	Training condition 1 (1 image pair/ROI)					Training condition 2 (10 image pairs/ROI)				
	1.1	1.2	1.3	1.4	1.5	2.1	2.2	2.3	2.4	2.5
Input	1.1	1.2	1.3	1.4	1.5	2.1	2.2	2.3	2.4	2.5
Training	NA	-1.761	-1.759	-1.766	-1.767	-1.781	-1.785	-1.781	-1.757	-1.759
loss	NA	-1.741	-1.732	-1.755	-1.743	-1.771	-1.772	-1.784	-1.784	-1.770
Validation	NA	47 minutes	2 hours	37 minutes	35 minutes	10 minutes	1 hours	1 hours	1 hours	1 hours
loss	NA	35 minutes	2 minutes	37 minutes	35 minutes	10 minutes	31 minutes	40 minutes	34 minutes	32 minutes
Training	NA	47 minutes	2 hours	37 minutes	35 minutes	10 minutes	1 hours	1 hours	1 hours	1 hours
time	NA	35 minutes	2 minutes	37 minutes	35 minutes	10 minutes	31 minutes	40 minutes	34 minutes	32 minutes
Test	0.377	0.707	0.707	0.707	0.706	0.702	0.700	0.704	0.705	0.698
mSSIM	0.079	0.035	0.035	0.034	0.034	0.034	0.034	0.034	0.034	0.034
NRMSE	22.464	29.656	29.652	29.708	29.698	29.761	29.746	29.851	29.862	29.752
PSNR (dB)										

CARE, content-aware image restoration; PCM, portable confocal microscopy; ROI, region of interest.

lower lip, which exhibited different cellular features from the skin. Thirty distinctive ROIs were imaged for the darkly pigmented skin, and 8 distinctive ROIs for the lower lip. Each ROI contained 30 image pairs, and improvements in the three image quality metrics (mSSIM, NRMSE, and PSNR) were calculated for each image pair.

Comparison With Non-DL Filtering Methods

We compared the CARE denoising performance to some of the widely used, non-DL filtering methods, such as median filter [12], Kuan filter [20], Lee filter [21], Fourier-domain filter, non-local-mean filter [11], and BM3D [10]. The non-DL methods were implemented and evaluated on the Matlab platform with Intel i7-6560u CPU. For each non-DL method, we iteratively adjusted the filtering parameters, and the parameters that provided good denoising results (i.e., large mSSIM, small NRMSE, large PSNR) were determined. In the Fourier-domain filter, frequency components within two narrow rectangular regions were blocked. Blocking regions were centered on the vertical axis with zero horizontal spatial frequency, and were mirror-symmetric to each other around the zero spatial frequency point. Blocked spatial frequency bandwidth along the vertical axis was iteratively optimized to reduce banding noise while minimizing image feature distortion. Low-SNR input images after the spatial registration were used to generate filtered images and calculate the image quality metrics. Denoising performance was quantitatively and qualitatively compared among non-DL methods, and the non-DL method that provided the best denoising performance was identified. Time taken for CARE denoising was measured using the Python platform on a consumer-grade laptop with the GeForce RTX 2070 GPU.

Qualitative Evaluation by Confocal Readers

Finally, denoising performance was qualitatively evaluated by three confocal readers. Two readers had over 5 years of experience of reading confocal images, and one reader less than 1 year of experience. Four categories of images (low-SNR input, CARE denoised, non-DL filtered, high-SNR ground truth) from the 45 ROIs in the test set were evaluated, resulting in a total of 180 images. One image was presented at a time without any information about the image category. The order of image presentation was randomized for both the ROI and image category. The reader was asked to evaluate the cellular features observed and the perceived noise level. For evaluation of cellular features, presence of (i) honeycomb pattern of keratinocytes, (ii) cobblestone pattern of melanocytes or melanin-containing basal cells, (iii) dermal papillae, and/or (iv) collagen was recorded. The features identified in each of the input, CARE denoised, and non-DL filtered images were compared to the features identified in the ground truth image. For evaluation of perceived noise level, three categories were used: (i) severe noise is present, making it challenging to appreciate cellular features, (ii) moderate noise is noticed, but cellular features are still observable, and (iii) negligible noise.

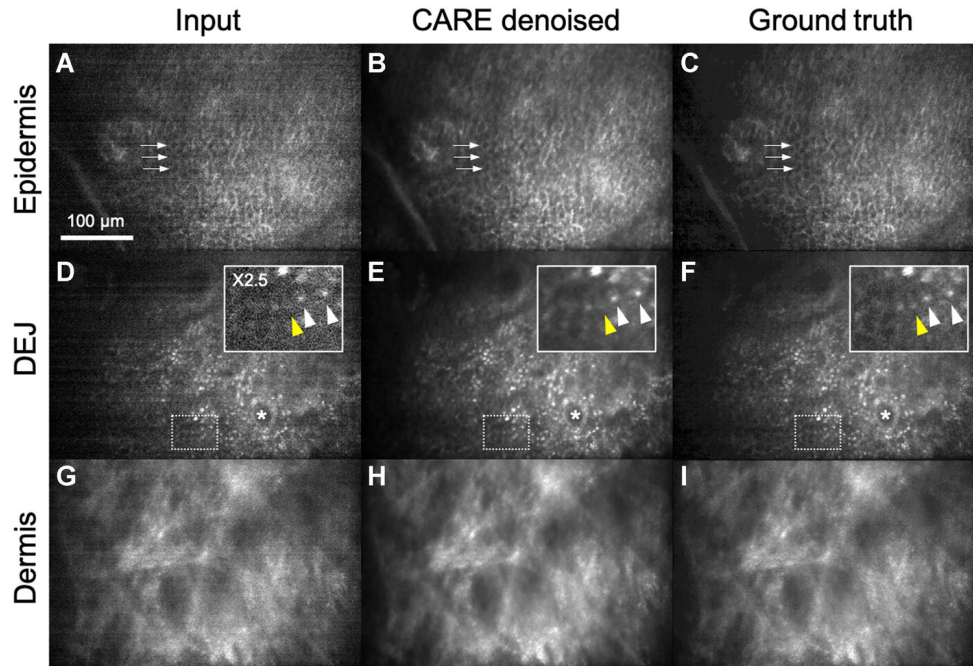


Fig. 5. Representative low-SNR input (A, D, G), CARE denoised (B, E, H), and high-SNR ground truth images (C, F, I). Arrows—keratinocytes; arrowheads—melanocytes or melanin-containing basal cells; asterisks—dermal papillae. CARE, content-aware image restoration; SNR, signal-to-noise ratio

RESULTS

Training Results

The training and validation loss results are summarized in Figure 4 and Table 1. For all models, the training loss (dotted line) and validation loss (solid line) converged to a similar value. The models that were trained with 10 image pairs/ROI (Models 2.1–2.5, blue lines in Fig. 4) generated smaller validation loss values than those by the models trained with 1 image pair/ROI (Models 1.1–1.5,

red lines in Fig. 4). Even though both training conditions used the same number of ROIs, Models 2.1–2.5 were trained with 10 times greater number of noise patterns than Models 1.1–1.5. The increased number of noise patterns used during training might have helped Models 2.1–2.5 perform better on removing previously unseen noise patterns in the validation set. Training time varied greatly, from 35 minutes to 2 hours, depending on the GPU resource available in the Google Colaboratory platform at the time of training.

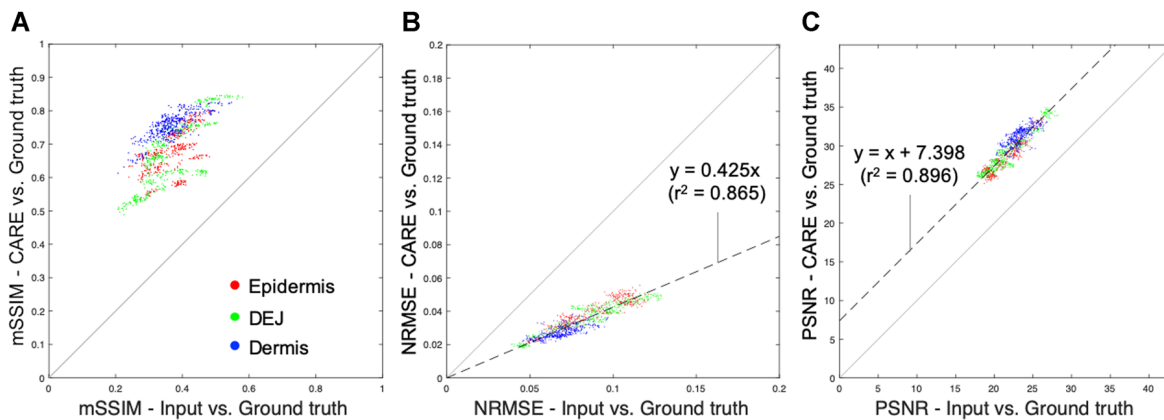


Fig. 6. Comparison of the image quality metrics between the input vs. ground truth pair and CARE denoised versus ground truth pair. (A) mean structural similarity (mSSIM). (B) normalized root mean squared error (NRMSE). (C) peak signal-to-noise ratio (PSNR). CARE, content-aware image restoration

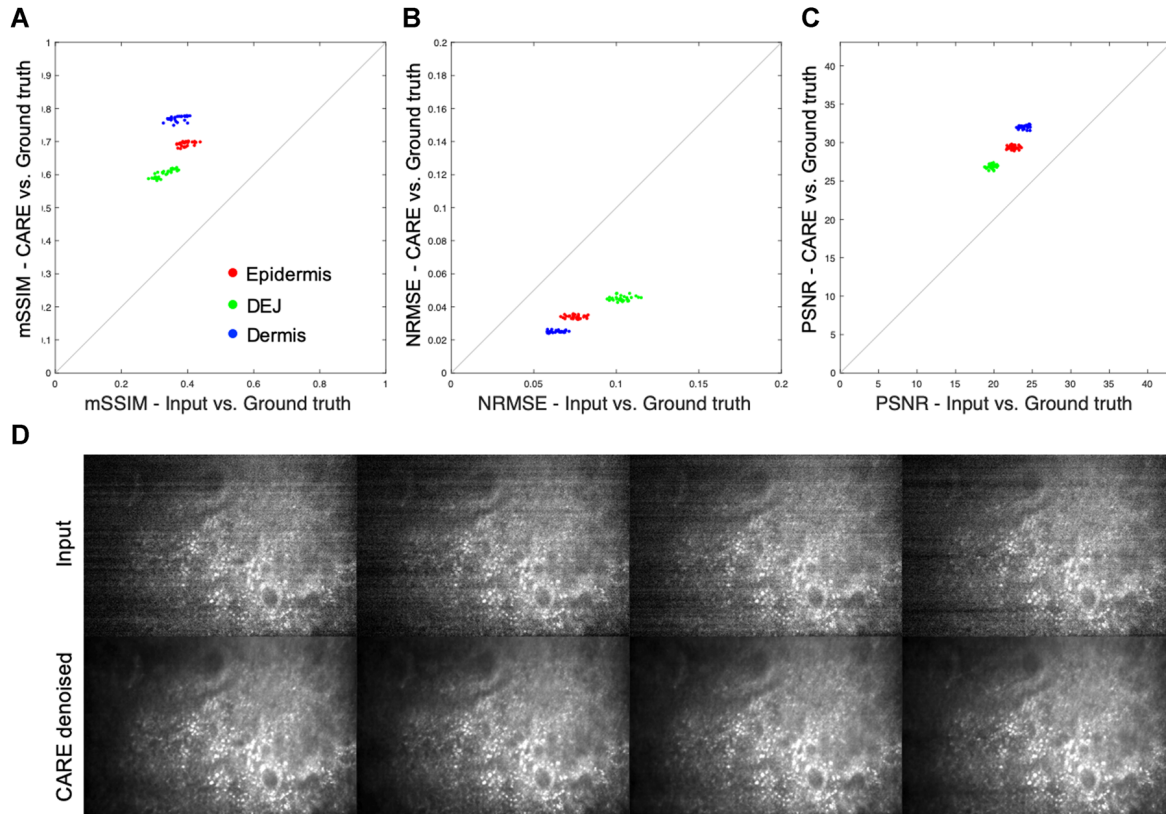


Fig. 7. Intra-ROI variations of the image quality metrics (A, B, C) and representative input and CARE denoised images (D). CARE, content-aware image restoration; ROI, region of interest.

Denoising Performance

Results for evaluating denoising performance are also summarized in Table 1. In addition to the quantitative comparison between models, we qualitatively examined perceived noise in CARE denoised images. In general, models with higher PSNR values provided more reduction of banding noise. Model 2.4 achieved the highest PSNR value, and also generated CARE denoised images with the least amount of perceived banding noise. Therefore, Model 2.4 was chosen for further analysis.

Representative low-SNR input, CARE denoised, and high-SNR ground truth images are shown in Figure 5. The input images (Fig. 5A, D, and G) showed noticeable banding noise. In the CARE denoised images (Fig. 5B, E, and H), banding noise was significantly reduced and was not readily visible. In the epidermis images (Fig. 5A, B, and C), keratinocytes were well visualized with the characteristic honeycomb pattern (arrows). In the CARE denoised image (Fig. 5B), a reduction of salt-and-pepper noise was noticed when compared to the input image (Fig. 5A). In the DEJ images (Fig. 5D, E, and F), melanocytes or melanin-containing basal cells were visualized as bright dots (arrowheads), and dermal papillae were shown as dark openings (asterisks). In dermis images (Fig. 5G, H, and I), the linear structure of the collagen or elastin fiber was well observed in all three images.

Limitations in CARE denoised were also noticed. Cell borders in the CARE denoised image (Fig. 5B) appeared smoother than those shown in the input image (Fig. 5A) and ground truth image (Fig. 5C). When the signal from the melanin was weak in the input image (yellow arrowhead, Fig. 5D), the CARE denoised image (Fig. 5E) had a difficulty in visualizing melanin with as high contrast as the ground truth image (Fig. 5F).

Image quality metrics were compared between the input vs. ground truth pair (horizontal axes in Fig. 6) and the CARE denoised vs. ground truth pair (vertical axes). For all three image quality metrics, the CARE denoised images achieved better performance: higher similarities (Fig. 6A), smaller errors (Fig. 6B), and higher SNR (Fig. 6C). In Figure 6A, CARE denoised mSSIM was increased by 1.9 times when compared to input mSSIM. The mSSIM improvement was higher for the dermis (blue), 2.10 times than for the epidermis (red) and DEJ (green), 1.85 and 1.87, respectively. Input mSSIM was determined in large part by noise in the input image, while CARE denoised mSSIM was affected primarily by residual errors in restoring cellular details. In dermis images, collagen or elastin fibers exhibited less fine details than the cellular structures in the DEJ and epidermis images. Therefore, similarity might have been degraded less in CARE denoised images of the dermis.

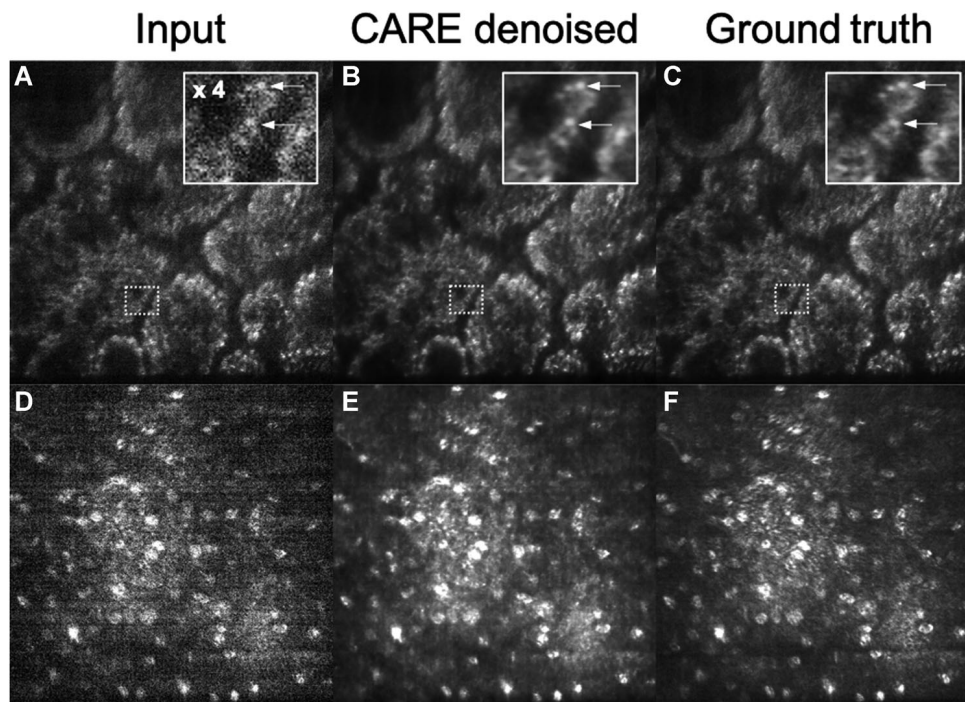


Fig. 8. Representative input, CARE denoised, and ground truth images obtained from the darkly pigmented skin (A–C) and lower lip (D–F). Arrows—high signal regions that correspond to cytoplasmic melanin in pigmented cells. CARE, content-aware image restoration.

In Figure 6B, CARE denoised NRMSE was reduced proportionally to input NRMSE regardless of the skin layer category. The slope of the fitted line in Figure 6B was 0.425, indicating that noise was reduced by 2.35 times in CARE denoised images. In Figure 6C, CARE denoised PSNR was increased from input PSNR by a constant amount, 7.398 dB.

We also examined variations of image quality metrics among 30 low-SNR input images from the same ROI and their corresponding CARE denoised images. Figure 7 shows the input and CARE denoised image quality metrics for a single representative ROI from each of the epidermis, DEJ, and dermis. Each ROI is plotted as 30 dots, showing 30 pairs of the input and CARE denoised metrics. The scattered plot of each color was elongated more along the horizontal axis, indicating that a wide range of the input image quality metric was mapped to a narrower range after CARE denoising. This implies that CARE generates similar

denoising results regardless of the input noise pattern. This trend is also shown in Figure 7D: input images (top row) had different banding noise patterns, but CARE denoised images (bottom row) appeared similar to each other.

Representative input, CARE denoised, and ground truth images of the darkly pigmented skin are shown in Figure 8A–C. Input images of the darkly pigmented skin DEJ (Fig. 8A) had approximately 1.5 times higher signal intensity than DEJ images from the lightly pigmented skin used for the network training, a trend observed in a previous RCM study [22]. Higher-magnification views (insets, Fig. 8A–C) showed that sub-cellular details of the pigmented cell [22], low signal by nucleus at the cell center, and surrounding high signal by cytoplasmic melanin (arrows, Fig. 8A–C) were easier to appreciate in the CARE denoised and ground truth images (Fig. 8B and C) than the input image (Fig. 8A). For 900 image pairs obtained from 30 distinctive ROIs of the darkly pigmented skin, CARE denoising increased mSSIM

TABLE 2. Comparison of the Denoising Performance Between Non-DL Methods

	Input	Median	Kuan	Lee	Fourier-domain	NLM	BM3D	CARE
mSSIM	0.377	0.608	0.607	0.472	0.373	0.472	0.591	0.705
NRMSE	0.079	0.041	0.045	0.063	0.081	0.063	0.0403	0.034
PSNR (dB)	22.464	28.137	27.369	24.735	22.271	24.735	28.337	29.862
Prediction time (seconds)	–	0.026	11.525	0.083	0.096	0.900	30.463	0.121

Following settings were used: Median filter—filter size = 5×5 ; Kuan filter—number of iteration = 1; Lee filter—number of iteration = 1; number of pixels for linear averaging in neighborhood = 5; Fourier-domain filter—blocked frequency bandwidth = 0.02 to 0.2 of the maximum vertical spatial frequency; BM3D—white gaussian with a sigma of 25. CARE, content-aware image restoration; DL, deep learning.

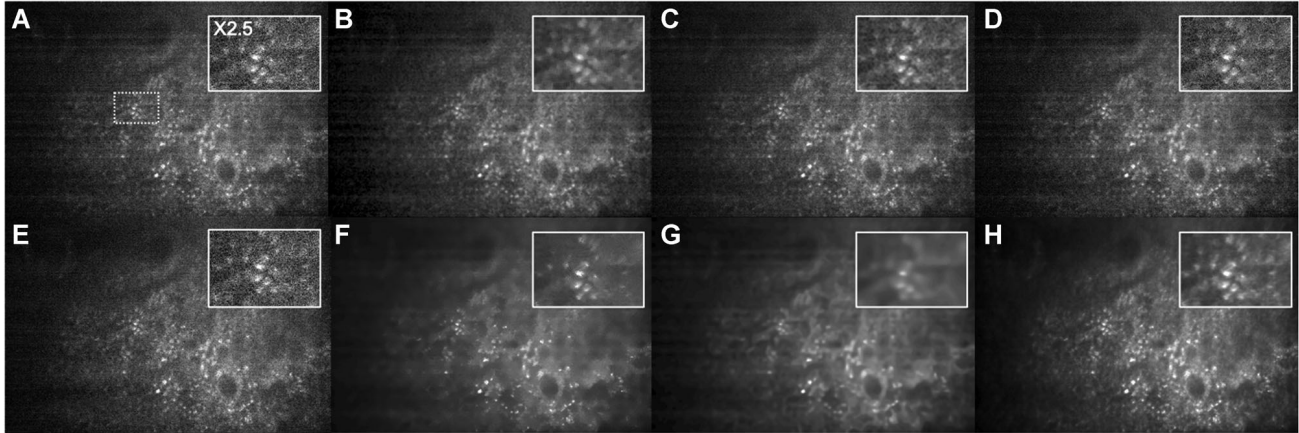


Fig. 9. Comparison of filtered images generated from non-DL denoising methods. (A) Input; (B) median filter; (C) Kuan filter; (D) Lee filter; (E) Fourier-domain filter; (F) non-local-mean filter; (G) BM3D; and (H) CARE. CARE, content-aware image restoration.

by 1.83 times, reduced NRMSE by 2.28 times, and increased PSNR by 7.04 dB. These image quality improvements were similar to those demonstrated for lightly pigmented skin images.

Figure 8D–F shows input, CARE denoised, and ground truth images of the lower lip. Images from the lower lip epithelium had approximately three times lower overall signal intensity than images of the lightly pigmented skin DEJ used for the network training. Reduction of noise is readily noticeable in the CARE denoised and ground truth images (Fig. 8E and F). Epithelial cell nuclei are clearly visualized as numerous bright dots in all three images. For 240 image pairs obtained from 8 distinctive ROIs of

the lower lip, CARE denoising increased mSSIM by 1.82 times, reduced NRMSE by 1.47 times, and increased PSNR by 6.73 dB. While CARE was shown useful in improving images of the lower lip qualitatively and quantitatively, the amount of noise reduction was less than that demonstrated for the skin.

Comparison With Non-DL Filtering Methods

Image quality metrics for the non-DL filtering methods are summarized in Table 2. Among the non-DL methods, BM3D produced the highest PSNR value. However, the BM3D-filtered image (Fig. 9G) showed significant blurring of cellular details. Among the two methods that provided

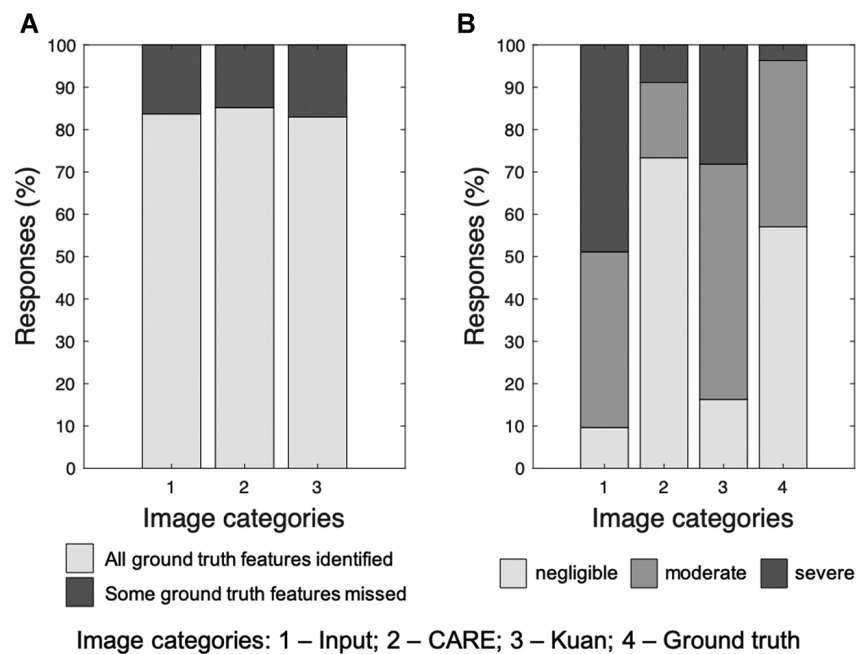


Fig. 10. Results of image quality assessment by human readers. (A) Feature identification results and (B) perceived noise level evaluation results. CARE, content-aware image restoration.

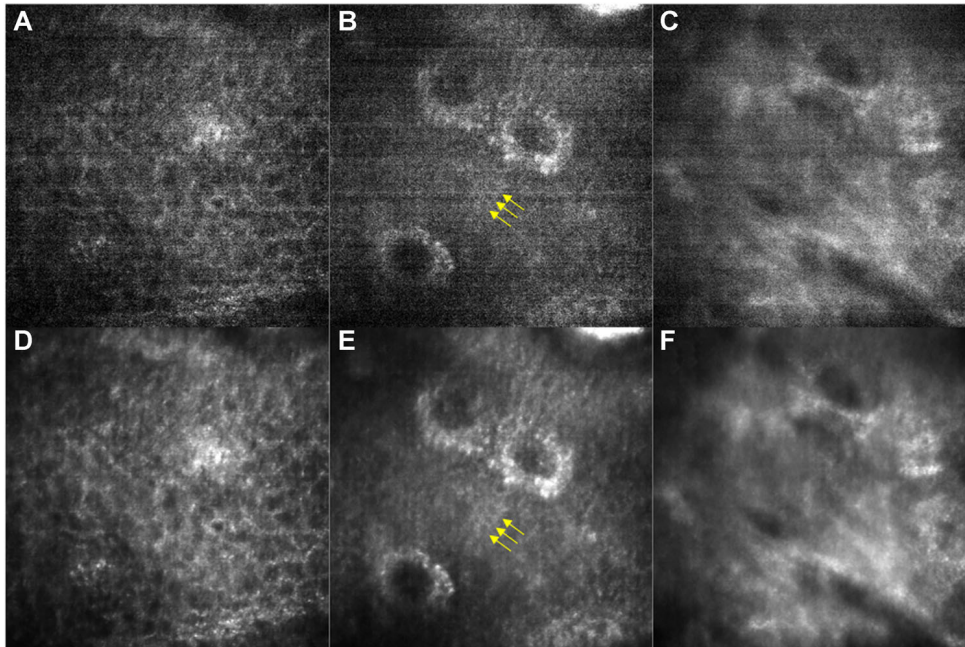


Fig. 11. PCM images obtained while manually changing the imaging depth through the epidermis (A, D), DEJ (B, E), and dermis (C, F). (A, B, C) Raw images and (D, E, F) CARE denoised images. Arrows—keratinocytes. CARE, content-aware image restoration; PCM, portable confocal microscopy.

the next highest PSNR values, Kuan filter produced slightly worse PSNR than the median filter, but the image sharpness was better maintained with the Kuan filter (inset, Fig. 9C) than the median filter (inset, Fig. 9B). Therefore, we used the Kuan filter-generated images during the qualitative assessment by confocal readers. Fourier-domain filter significantly reduced banding noise (Fig. 9E) but did not reduce salt-and-pepper noise noticeably, which resulted in similar image quality metrics as the input images (Table 2). Overall, non-DL methods fell short to simultaneously reduce banding noise and salt-and-pepper noise when compared to CARE (Fig. 9H).

Image Assessment by Confocal Readers

Results from the image quality assessment by confocal readers are summarized in Figure 10. The feature identification results (Fig. 10A) showed no significant difference in correctly identifying all of the cellular features found in the ground truth image: input –84% of the images (95% confidence interval =76-91%); CARE –85% (78-91%); Kuan –83% (76-89%). The perceived noise evaluation results (Fig. 10B) showed that CARE denoised images produced negligible noise more often, 73% (65-81%) of all evaluations, than input and Kuan images, 10% (5-16%) and 16% (11-24%), respectively. The readers also found that the vast majority of the CARE images showed moderate or negligible noise, 91% (85-95%) of the cases. This proportion of moderate or negligible noise images was significantly higher than the proportions for input and Kuan images, 51% (42-60%) and 72% (64-79%), respectively.

CARE Denoising of PCM Video

We tested CARE for denoising PCM videos obtained while changing the imaging depth, mimicking real-time 3D PCM imaging. Two hundred PCM images were obtained at the imaging speed of 180 frames/second (corresponding imaging time =1.1 seconds). Supplemental Video 1 shows the input (left) and CARE denoised (right) images side by side. The CARE denoised images exhibited significantly reduced noise. Even though the device was continuously translated during the video acquisition, each PCM image still visualized cellular details without noticeable image blurring, showing the benefit of using a short exposure time. Certain cellular features, such as small keratinocytes (arrows in Fig. 11B and E) were easier to appreciate in the CARE denoised image. While each CARE denoised image (Fig. 11D–F) did not exhibit noticeable banding noise, variations of the residual banding noise in the CARE denoised images were noticeable in Supplemental Video 1.

CONCLUSIONS

In this paper, we have evaluated the feasibility of using a DL-based method, CARE, for denoising PCM images obtained with a short exposure time. Results from the quantitative and qualitative evaluations showed that CARE denoised significantly reduced noise presented in input images. CARE also reduced noise in images obtained from the darkly pigmented skin and lower lip. The CARE approach provided better denoising performance than non-DL filtering methods. High-speed, high-SNR PCM imaging enabled by CARE is expected to reduce motion blur and increase the image sharpness, especially when images are acquired with a

handheld PCM device. The fast imaging speed can also allow for real-time 3D PCM imaging and imaging of dynamic events, such as blood flow.

Several limitations in CARE denoising were also observed. Time taken for denoising each PCM image with the CARE network and a consumer-grade laptop was 0.12 seconds (Table 2), resulting in a processing rate of 8.3 frames/second. While the current processing rate is significantly lower than the image acquisition rate, 180 frames/second, this rate still allows for the display of CARE-denoised images in near real-time (Supplemental Video 1). Therefore, *in situ* CARE-denoised images can be used to (i) guide image acquisition toward diagnostically important areas and (ii) ensure that raw image data does not have excessive image degradation that is difficult to mitigate with CARE postoperatively. The PCM image data can be stored in real-time without any processing during the imaging session and can later be batch-processed with the CARE network. The data flow rate can be increased by feeding the image data from the system memory to GPU directly, which can subsequently increase the CARE processing rate. We will investigate if modifying the CARE network structure could reduce the processing time while providing sufficient denoising performance, including the use of a smaller number of feature layers.

Cellular features in CARE denoised images appeared smoother than those shown in the input and ground truth images. A similar trend was noticeable from previous CARE work for denoising fluorescence microscopy images [9]. The use of convolution layers during the upsampling process (right half of the CARE network) might have reduced the image sharpness, and the loss function used in CARE might not have been optimal for achieving high image sharpness [23]. Even with the smoother appearance, CARE denoised images did not degrade human readers' capability to identify cellular features compared to the input images (Fig. 10A). However, if future studies find that reduction of sharpness negatively affects the diagnostic capability, we will investigate different approaches for improving the image sharpness, including reducing the convolution kernel size or implementing deconvolutional layers during the upsampling process, and using a different loss function that promotes sparsity.

Another limitation of this work is that the training and test sets were collected from healthy skin and did not include images obtained from disease-suspicious skin lesions. In the future, we will acquire a large dataset of PCM images from various skin lesions using the data acquisition method described in this paper. We will then train the CARE network and evaluate its utility for aiding diagnosis with PCM images. Various metrics will be evaluated for unprocessed PCM images and CARE denoised images, including diagnostic accuracy, the time needed to render a diagnosis, and diagnostic confidence.

ACKNOWLEDGMENTS

The authors thank Dr. Milind Rajadhyaksha (Memorial Sloan Kettering Cancer Center) for helpful

discussions. This research was supported in part by NIH R21TW011222.

REFERENCES

- Milind Rajadhyaksha MG, Esterowitz D, Webb RH, Rox Anderson R. In vivo confocal scanning laser microscopy of human skin: Melanin provides strong contrast. *J Invest Dermatol* 1995;104:946–952.
- Milind Rajadhyaksha SG, Zavislan JM, Rox Anderson R, Webb RH. In vivo confocal scanning laser microscopy of human skin II: Advances in Instrumentation and comparison with histology. *J Invest Dermatol* 1999;113:293–303.
- Rajadhyaksha M, Marghoob A, Rossi A, Halpern AC, Nehal KS. Reflectance confocal microscopy of skin in vivo: From bench to bedside. *Lasers Surg Med* 2017;49(1):7–19.
- Peterson G, Zaroni DK, Ardigo M, Migliacci JC, Patel SG, Rajadhyaksha M. Feasibility of a video-mosaicking approach to extend the field-of-view for reflectance confocal microscopy in the oral cavity in vivo. *Lasers Surg Med* 2019;51(5):439–451.
- Yoo H, Kang D, Katz AJ, et al. Reflectance confocal microscopy for the diagnosis of eosinophilic esophagitis: a pilot study conducted on biopsy specimens. *Gastrointest Endosc* 2011;74(5):992–1000.
- Freeman EE, Semeere A, Osman H, et al. Smartphone confocal microscopy for imaging cellular structures in human skin in vivo. *Biomed Opt Express* 2018;9(4):1906–1915.
- Gong C, Stratton DB, Curriel-Lewandrowski CN, Kang D. Speckle-free, near-infrared portable confocal microscope. *Appl Opt* 2020;59(22):G41–G46.
- Freeman EE, Semeere A, Laker-Oketta M, et al. Feasibility and implementation of portable confocal microscopy for point-of-care diagnosis of cutaneous lesions in a low-resource setting. *J Am Acad Dermatol* 2020;84:499–502.
- Weigert M, Schmidt U, Boothe T, et al. Content-aware image restoration: pushing the limits of fluorescence microscopy. *Nat Methods* 2018;15(12):1090–1097.
- Dabov K, Foi A, Katkovnik V, Egiazarian K. Image denoising with block-matching and 3D filtering. *International Society for Optics and Photonics*. 2006. p 606414.
- Buades A, Coll B, Morel J-M. A non-local algorithm for image denoising. *IEEE*. 2005. pp 60–65.
- Two-Dimensional LIMJ. *Signal and Image Processing*. Englewood Cliffs: Prentice Hall; 1989.
- Lehtinen J, Munkberg J, Hasselgren J, Laine S, Karras T, Aittala M, Aila T. Noise2noise: Learning image restoration without clean data. *arXiv preprint*. 2018: arXiv 180304189.
- Krull A, Buchholz T-O, Jug F. Noise2void-learning denoising from single noisy images. In: *Proceedings of the IEEE/CVF Conference on Computer Vision and Pattern Recognition*. 2019:2129–2137.
- Buchholz T-O, Krull A, Shahidi R, Pigino G, Jékely G, Jug F. Chapter 13—Content-aware image restoration for electron microscopy. In: Müller-Reichert T, Pigino G, editors. *Methods in Cell Biology*. Amsterdam, Netherlands: Elsevier; 2019. 152:277–289.
- Buchholz T-O, Jordan M, Pigino G, Jug F. Cryo-CARE: Content-Aware Image Restoration for Cryo-Transmission Electron Microscopy Data. In: *2019 IEEE 16th International Symposium on Biomedical Imaging (ISBI 2019)*. IEEE; 2019:502–506.
- Ronneberger O, Fischer P, Brox T. U-net: Convolutional Networks for Biomedical Image Segmentation. In: Navab N, Hornegger J, Wells W, Frangi A, eds. *Medical Image Computing and Computer-Assisted Intervention - MICCAI 2015*. Vol 9351. Cham: Springer; 2015. pp 234–241.
- Von Chamier L, Jukkala J, Spahn C, et al. ZeroCostDL4Mic: An open platform to simplify access and use of Deep-Learning in Microscopy. *BioRxiv*. 2020.
- Wang Z, Bovik AC, Sheikh HR, Simoncelli EP. Image quality assessment: from error visibility to structural similarity. *IEEE Trans Image Process* 2004;13(4):600–612.

20. Kuan DT, Sawchuk AA, Strand TC, Chavel P. Adaptive noise smoothing filter for images with signal-dependent noise. *IEEE Trans Pattern Anal Mach Intell* 1985; 2:165–177.
21. Lee J-S. Speckle suppression and analysis for synthetic aperture radar images. *Opt Eng* 1986;25(5):255636.
22. Rajadhyaksha M, Grossman M, Esterowitz D, Webb RH, Anderson RR. In vivo confocal scanning laser microscopy of human skin: Melanin provides strong contrast. *J Invest Dermatol* 1995;104(6):946–952.
23. Zhao H, Gallo O, Frosio I, Kautz J. Loss functions for image restoration with neural networks. *IEEE Trans Comput Imag* 2016;3(1):47–57.

SUPPORTING INFORMATION

Additional supporting information may be found online in the Supporting Information section at the end of the article.
Supporting information.

Handheld cross-polarised microscope for imaging individual pigmented cells in human skin in vivo

Rafael Romero¹ | Jingwei Zhao² | Delaney Stratton³ | Kenneth Marcelino² | Momoka Sugimura² | Alia Nichols² | Salvador Gonzalez⁴ | Manu Jain⁵  | Clara Curiel-Lewandrowski³ | Dongkyun Kang^{1,2} 

¹Department of Biomedical Engineering, University of Arizona, Tucson, Arizona

²College of Optical Sciences, University of Arizona, Tucson, Arizona

³Division of Dermatology, College of Medicine-Tucson, University of Arizona, Tucson, Arizona, United States

⁴Department of Medicine and Medical Specialties, Alcalá University of Madrid, Madrid, Spain

⁵Dermatology Service, Department of Medicine, Memorial Sloan Kettering Cancer Center, New York, New York, United States

Correspondence

Dongkyun Kang, Department of Biomedical Engineering, University of Arizona, 1630 E University Blvd, Tucson, AZ 85721.

Email: dkkang@arizona.edu

Clara Curiel, College of Medicine-Tucson, University of Arizona, 3838 N Campbell Ave, Tucson, AZ 85719.

Email: ccuriel@arizona.edu

Abstract

We present the development of a simple, handheld cross-polarised microscope (CPM) and demonstration of imaging individual pigmented cells in human skin in vivo. In the CPM device, the cross-polarised detection approach is used to reduce the specular reflection from the skin surface and preferentially detect multiply-scattered light. The multiply-scattered light works as back illumination from within the tissue towards the skin surface, and superficial pigment such as intraepidermal melanin absorbs some spectral bands of the multiply-scattered light and cast coloured shadows. Since the light that interacted with the superficial pigment only needs to travel a short distance before it exits the skin surface, microscopic details of the pigment can be preserved. The CPM device uses a water-immersion objective lens with a high numerical aperture to image the microscopic details with minimal spherical aberrations and a small depth of focus. Preliminary results from a pilot study of imaging skin lesions in vivo showed that the CPM device could reveal three-dimensional distribution of pigmented cells and intracellular distribution of pigment. Co-registered CPM and reflectance confocal microscopy images showed good correspondence between dark, brown cells in CPM images and bright, melanin-containing cells in reflectance confocal microscopy images.

KEYWORDS

capillary imaging, cross-polarised microscopy, in vivo microscopy, melanin imaging, skin imaging, three-dimensional microscopy

1 | INTRODUCTION

Dermatoscopy is the standard imaging method that allows for the examination of human skin lesions in vivo.¹ Dermatoscopes provide magnified images of the skin, visualising patterns and structures that cannot be readily seen

with the naked eye.² However, dermatoscopy does not provide sufficient resolution to examine individual pigmented cells due to the relatively low magnification and numerical aperture (NA) of the objective lens.³ If individual pigmented cells could be visualised, it could enhance diagnostic accuracy, indication for skin biopsy, aid monitoring of disease progression, and guide treatment. For example, examination of pigmented cells can show early signs of cytological or architectural changes when monitoring

Rafael Romero, Jingwei Zhao and Delaney Stratton contributed equally to this work and share first authorship.

pigmented lesions, which can provide either reassurance to the patient or the need to perform a skin biopsy.

There are several microscopy techniques that can noninvasively visualise individual pigmented cells. For example, reflectance confocal microscopy (RCM) uses the scattering contrast to visualise certain cellular structures (e.g., cell membrane of keratinocytes, melanin in melanocytes and melanin-containing basal cells).⁴ However, the scattering contrast used in RCM is not specific to melanocytic cells. Nonmelanocytic cells such as Langerhans cells can exhibit similar shape and brightness to melanocytic cells, which can pose challenges in diagnosing certain pigmented lesions.^{5,6,7} High-resolution confocal optical coherence tomography (HR-OCT) is another imaging method capable of imaging cellular structures noninvasively. HR-OCT provides a larger imaging depth than RCM while maintaining high resolution.^{8,9} However, HR-OCT also relies on the scattering contrast, and is likely to have challenges in distinguishing nonmelanocytic, highly scattering cells from melanocytic cells. Two-photon microscopy (TPM) is another method capable of imaging cellular structures noninvasively. In TPM, light from a short-pulse laser is incident onto the skin and excites intrinsic fluorophores (e.g., NADH, melanin) and visualise keratinocytes and melanin-containing cells.^{10,11} Two-photon microscopy, however, may cause thermal damage when imaging melanin-containing cells.¹²

While the aforementioned *in vivo* microscopy technologies have shown promise for aiding diagnosis and treatment of skin diseases, the cost to acquire the devices and overall operability limitations of the equipment makes it challenging to adopt these microscopy technologies in routine dermatology practices. In addition, the scattering contrast provided by RCM and LC-OCT is not specific to pigmented cells. In this paper, we report the development of a simple, handheld cross-polarised microscopy (CPM) device and the demonstration of three-dimensional imaging of individual pigmented cells *in vivo*. The working principle and schematic of the CPM device are described, and results from imaging skin lesions *in vivo* are presented.

2 | MATERIAL AND METHODS

2.1 | Cross-polarised microscopy of individual pigmented cells *in vivo*

The working principle of noninvasively imaging individual pigmented cells using CPM is shown in Figure 1. When light illuminates the skin, some of the illumination photons are multiply-scattered by the tissue and exit the skin surface (Figure 1A). The multiply-scattered photons lose spatial information of the cellular structures they

were scattered by, and therefore cannot be used to visualise cells based on the scattering contrast. However, some of the multiply-scattered photons are spectrally absorbed by superficial pigment such as melanin right before they exit the skin surface (Figure 1A). Since these photons only need to travel a short distance before exiting the skin surface, the microscopic details of the pigment can be preserved. For example, human skin has a scattering coefficient of 11–14 mm⁻¹ at 550 nm.¹³ This range of scattering coefficient corresponds to a mean free path of 71–91 μm. Given that the typical thickness of epidermis is 50–100 μm, microscopic details of intraepidermal pigment can be preserved with minimal scattering. In summary, multiply-scattered photons provide illumination from within the skin tissue, and intraepidermal pigment generates microscopic distribution of spectral absorption, casting coloured shadows in the image. Cross-polarised detection is used to reduce the specular reflection from the skin surface while detecting multiply-scattered, de-polarised photons. This approach of imaging shadows cast by superficial absorbers in skin has been already used in other *in vivo* microscopy approaches such as side dark field microscopy. However, side dark field microscopy has been mainly used for imaging capillaries in oral mucosa and nailfold,¹⁴ and high-resolution imaging of individual pigmented cells in skin has not been reported to our knowledge.

In addition to the absorption contrast generated by the superficial pigment, the imaging system needs to provide a sufficient resolution to visualise cellular details. This requires the use of a high-NA objective lens with a small depth of focus. When the focal plane is located at the same depth as the pigment (depth 1 in Figure 1B), the intensity reduction due to the pigment in the image is confined to a small region (Microscopy image 1 in Figure 1B). When the focal plane is moved deeper into the tissue (depth 2 then to 3 in Figure 1B), the intensity reduction appears in a larger area of the microscopy image but with significantly less strength (Microscopy images 1 and 2 in Figure 1B). Therefore, the effect of the pigment's light absorption is mostly noticeable within a small volume of the tissue.

In high-NA microscopy imaging, the use of an index-matching medium, instead of air, is critical in reducing spherical aberrations when imaging sub-surface cellular details. We simulated wavefront errors when imaging below stratum corneum with 0.8 NA objective lenses with various index media (Figure 2). The thickness of stratum corneum was assumed 20 μm, and the refractive index of 1.51 was used for stratum corneum and 1.34 for the rest of epidermis.¹⁵ The simulation results show that the dry objective lens will experience significant resolution degradation even when imaging an epidermal depth of 35 μm, which is likely to pose challenges in imaging pigmented cells near the base of the epidermis. The simulation results

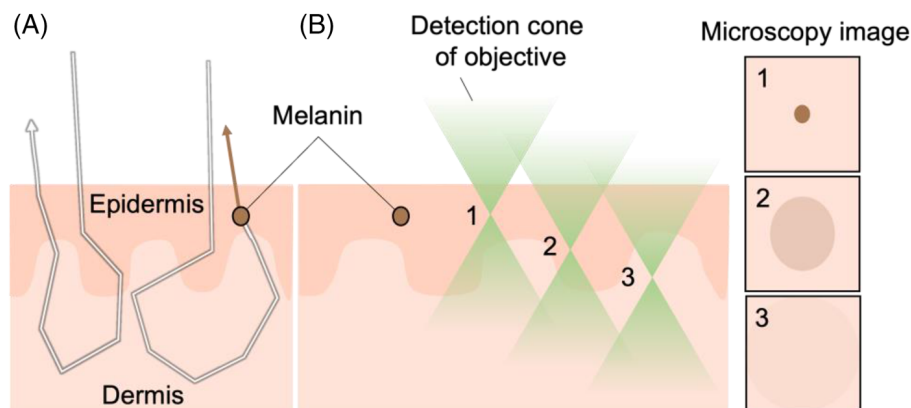


FIGURE 1 Working principle of imaging individual pigmented cells using cross-polarised microscopy. (A) Light path through the skin tissue when a pigment is absent (left) and present (right) and (B) change of the appearance of the pigment on microscopy images as a function of imaging depth.

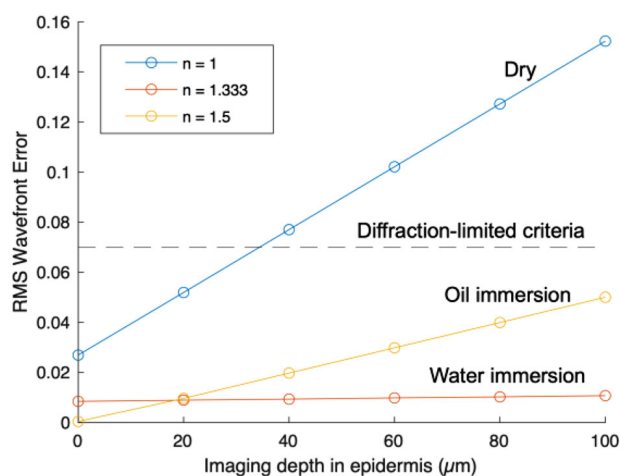


FIGURE 2 Change of imaging performance when imaging inside epidermis with three different immersion conditions (dry, water, oil).

also show that both water-immersion and oil-immersion objective lenses would provide adequate performance throughout the entire epidermis (typical thickness = 50–100 μm). In the handheld CPM device, a water-immersion objective lens was used rather than an oil-immersion objective lens due to the relatively long working distance of the water-immersion objective lens (3.5 mm) and ease of lens cleaning after imaging.

2.2 | Handheld CPM device

In order to evaluate the feasibility of CPM imaging of individual pigmented cells *in vivo*, we have developed a handheld CPM prototype. Figure 3 shows the schematic of the handheld CPM prototype. Light from a white LED (XPGDWT-H1-0000-00HE8-S01, Cree LED; working cur-

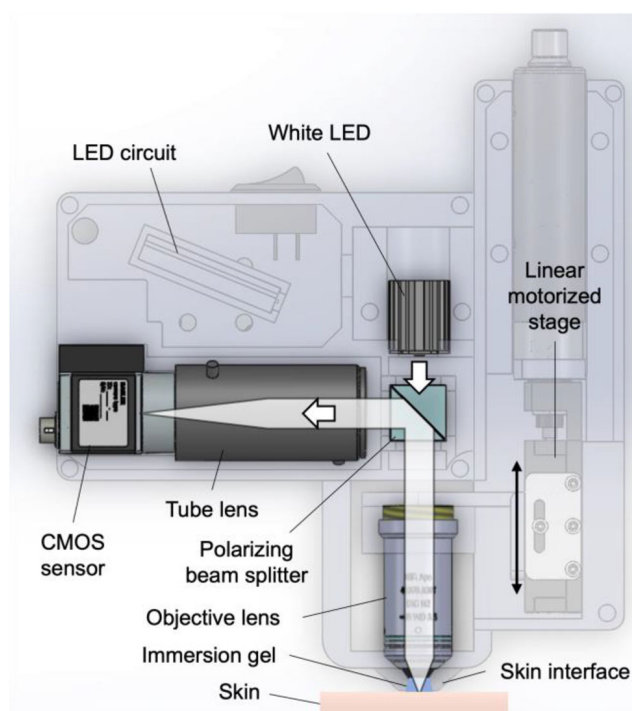


FIGURE 3 Schematic of the handheld CPM prototype.

rent = 1 A; forward voltage = 2.73 V) is incident on a polarising beam splitter, and linearly polarised light (p-polarisation) passes through the polarising beam splitter and illuminates the skin through a high-NA objective lens (N40X-NIR, Nikon; NA = 0.80; water immersion). Light returning from the tissue is captured by the same objective lens. Detection light with a s-polarisation state is reflected by the polarising beam splitter onto the camera lens ($f = 50$ mm) and the colour CMOS sensor (aca4024-29uc, Basler; 4024×3036 pixels; pixel size = 1.85 μm). The objective lens is attached to a motorised stage (T-LA13A, Zaber; travel range = 13 mm; maximum speed = 4 mm/s), which

changes the imaging depth to acquire CPM images at multiple depth levels.

2.3 | Image acquisition and processing

Imaging performance of CPM was evaluated by imaging the United State Air Force (USAF) resolution target and measuring the full-width-half-maximum (FWHM) of the line-spread function. The pilot study of imaging skin lesions in vivo with the CPM device was reviewed and approved by the University of Arizona Internal Review Board. For each skin lesion, wide-field colour images and dermatoscopy images were acquired using a standard dermatoscope (VEOS, Canfield). Next, index-matching gel (GenTeal, Alcon) was applied on the CPM objective lens, and the CPM device was placed on the skin lesion. The skin surface was identified by observing the skin surface folds in CPM images while translating the focal plane of the objective lens. From the skin surface, 50 CPM images were continuously acquired while the imaging depth was translated deeper into the tissue with a step size of 5–6 μm between images. This resulted in the total imaging depth range of 250–300 μm . The image acquisition rate was set as 30 frames/s, and the exposure time was 2–2.5 ms. The time for acquiring a three-dimensional image stack was 1.7 s. One of the CPM-imaged lesions was also imaged by a portable RCM device¹⁶ to compare the cellular features between CPM and RCM.

The CPM images were post-processed by blind deconvolution. The deconvblind function of MATLAB (MathWorks, version = R2020b) was applied on the three-dimensional CPM image stack. A theoretical, three-dimensional point-spread function generated by the ImageJ PSF Generator plugin^{17,18} was used as the initial point-spread function. Various numbers of deconvolution iterations were evaluated for CPM images. For most of the CPM datasets, five to seven iterations of blind deconvolution provided enhanced contrast of pigment while not generating noticeable artefacts.

3 | RESULTS

A photo of the handheld CPM device is shown in Figure 4. The device dimensions were 20.7 cm (W) \times 11.1 cm (D) \times 23.9 cm (H), and the weight was 1.6 kg. Light power on the skin was 2.15 mW. The material cost of the device was ~\$4600. It is noted that the objective lens was the most expensive component, >\$2500. Lateral resolution, the FWHM of the line-spread function, was 0.7 (\pm 0.1) μm for the red channel, 0.7 (\pm 0.1) μm for the green channel and 0.7 (\pm 0.2) μm blue channel. The Bayer filter used in

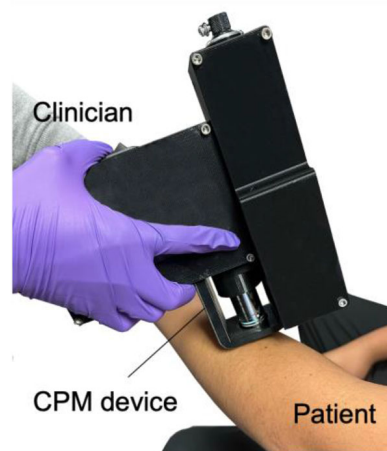


FIGURE 4 Photo of the handheld CPM device.

the colour CMOS sensor led to limitations in the resolution measurements. Based on the magnification between the tissue and CMOS sensor, 10, the pixel size on the tissue was 0.185 μm . In the Bayer filter, the sampling period of each colour channel is twice the pixel size. Therefore, the sampling period on the tissue for each colour channel was 0.37 μm . The minimum resolution measurable with this sampling period is 0.74 μm based on the Nyquist sampling criteria. As a result, the measured resolution was 0.7 μm for all three-colour channels even though the optical resolution was supposed to be better for the blue channel than the red channel.

Figure 5 shows representative dermatoscopy and CPM images of human forearm (sun-exposed side, Fitzpatrick skin phototype III). In the magnified dermatoscopy image (Figure 5B), fluctuation of image brightness is noticeable, but individual pigmented objects are not distinguishable. The CPM images obtained from epidermis (Figure 5C–E) visualise distinctive brown objects (arrows). The distribution of the brown objects changes as the imaging depth changes (Figure 5C–E), indicating that the CPM device has the capability to visualise three-dimensional distribution of these objects. The distribution (present in epidermis but absent in dermis) and colour (brown) of these objects indicate that these objects might be melanin-containing basal cells. Pink tubular structures are also visualised in CPM images (arrowheads in Figure 5), which appear to represent the top of a capillary (Figure 5D) branching into the ascending and descending blood vessels (Figure 5F) and eventually connecting to a larger blood vessel (Figure 5H).

The CPM-imaged region shown in Figure 5 was also imaged by portable RCM. The brown objects in the CPM image (arrows in Figure 6A) appear bright in the spatially registered RCM image (arrows in Figure 6B). Previous studies showed that RCM visualises melanin-containing cells at the dermal-epidermal junction as distinctive bright

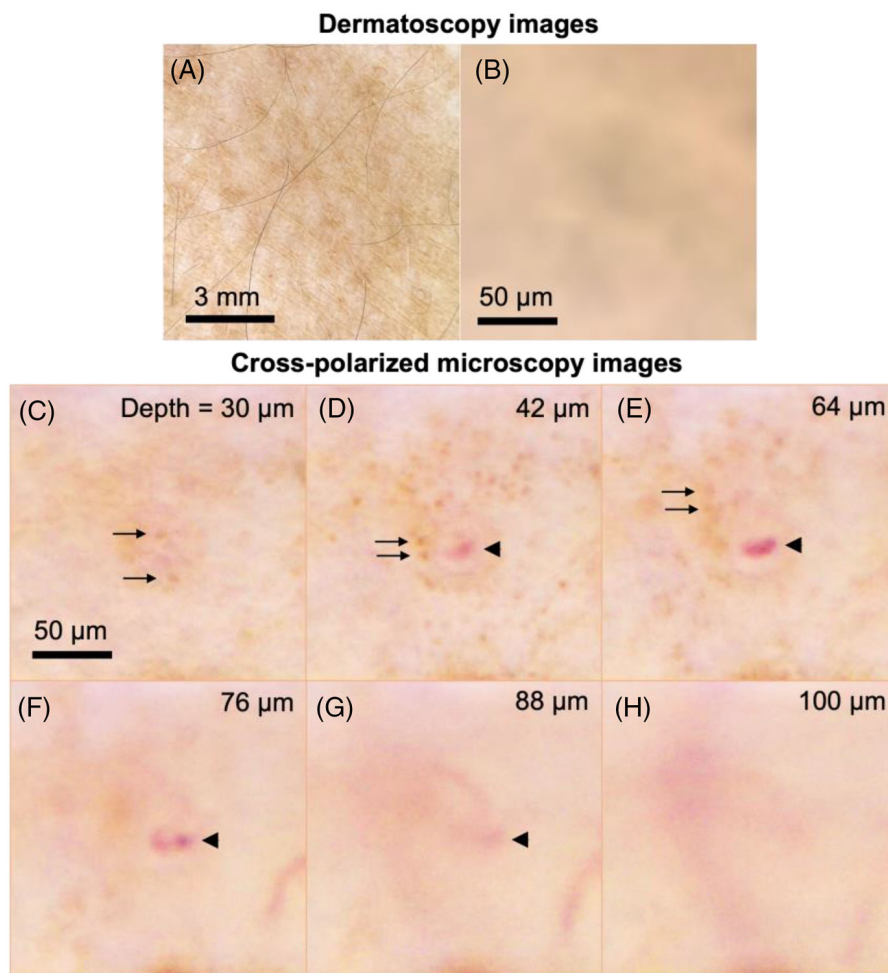


FIGURE 5 Dermatoscopy (A, B) and CPM (C–H) images of human forearm. arrows – melanin-containing cells; arrowheads – capillaries.

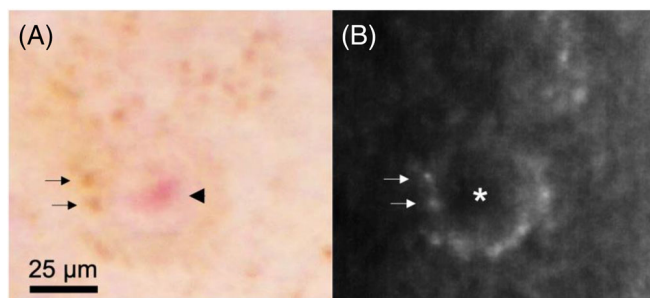


FIGURE 6 Spatially registered CPM (A) and RCM (B) images. arrows – melanin-containing cells; arrowhead – capillary; asterisk – dermal papillae.

objects because of the higher refractive index of melanin than surroundings.⁴ Therefore, these spatially registered CPM and RCM images further support that the brown objects in CPM images are melanin-containing cells. The dermal papillae often appear as a dark opening in RCM images (asterisk in Figure 6B) if no blood cells are present within the imaging plane at the time of image acquisition,

while the capillary inside the dermal papillae is shown pink in the CPM image (arrowhead in Figure 6A).

Representative dermatoscopy and CPM images of a junctional nevus are shown in Figure 7. The magnified view of the dermatoscopy image (Figure 7B) shows the contrast between pigmented and nonpigmented regions, but individual pigmented cells are not clearly distinguished. In CPM images (Figure 7C–E), numerous pigmented cells are readily observed. The change of the cell distribution is also noticed as the imaging depth changes from 20 to 70 μm . In a magnified CPM image (Figure 7F), the cytoplasmic distribution of melanin is well observed: melanin is distributed in cytoplasmic space that resembles a letter c (arrow in Figure 7F), while cell nucleus shows the lack of melanin (arrowhead in Figure 7F).

Dermatoscopy and CPM images of cherry angioma are shown in Figure 8. In the CPM image obtained from the imaging depth of 40 μm (Figure 8D) shows a scattered distribution of melanin-containing cells at the basal layer of epidermis (Fitzpatrick skin phototype III). At a deeper imaging depth of 125 μm (Figure 8E), a network of

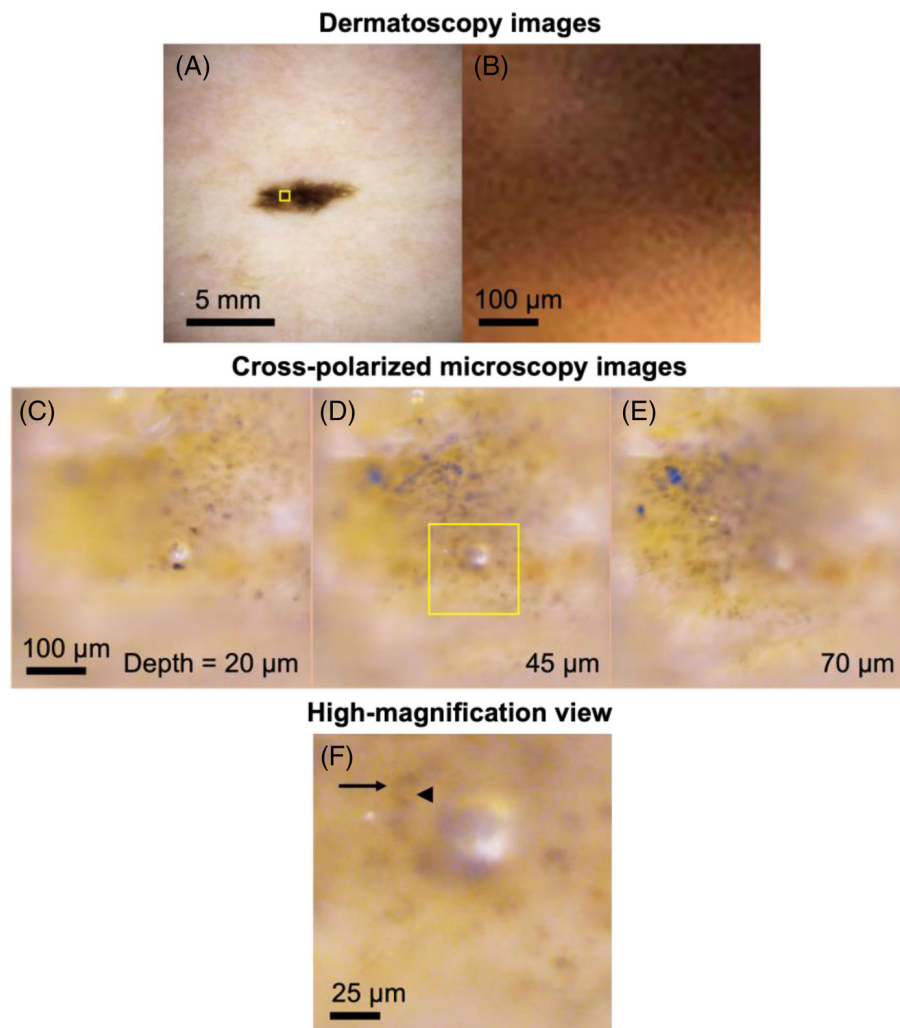


FIGURE 7 Dermatoscopy (A, B) and CPM (C–F) images of a junctional nevus. arrow – cytoplasmic distribution of melanin; arrowhead – cell nucleus devoid of melanin.

capillaries is well visualised. The cross-sectional view of the CPM image data obtained from a dotted line in Figure 8C–E is shown in Figure 8F. In the cross-sectional CPM image, the depth of melanin and capillary is readily measurable.

4 | DISCUSSION

In this paper, we have demonstrated imaging of individual pigmented cells *in vivo* using a handheld CPM device. There were two key factors that made it possible to image individual pigmented cells in skin with standard microscopy rather than sophisticated microscopy techniques such as RCM or TPM. First, the superficial distribution of melanin in human skin generates the absorption contrast with microscopic details that can be detected from above the skin surface. Second, the high-NA, water-immersion objective used in the handheld CPM device provided a small effective detection volume with

minimal spherical aberrations, which made the pigmented cells appear clear. The capability of examining individual pigmented cells with CPM could aid monitoring, guiding, and research of various treatment approaches. Other microscopy techniques with a cellular imaging capability, such as RCM, have been shown to provide a higher specificity than dermatoscopy in diagnosing skin cancers.^{19,20} While we envision that the cellular imaging capability provided by CPM could also help improve the diagnostic specificity, further studies will be needed to establish the sensitivity and specificity of CPM. Additionally, CPM allows for easy measurement of the depth of melanin and capillaries from the cross-sectional view, which could be beneficial in guiding laser therapy of pigmented lesions. Specifically, the information on melanin depth and capillary depth could be used to determine the type of laser (e.g., wavelength, pulse width) and output parameters (e.g., power, treatment duration) that are adequate for treating the pigmented skin layers but do not damage capillaries.²¹

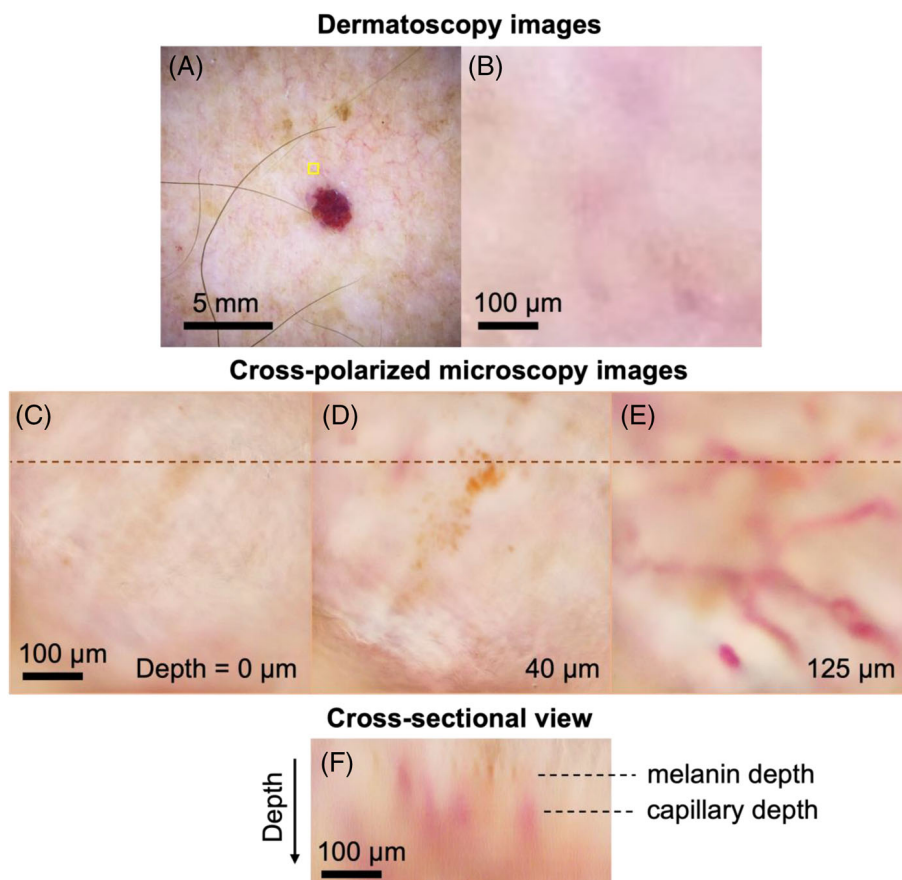


FIGURE 8 Dermatoscopy (A, B) and CPM (C–F) images of cherry angioma. C–E: *en face* CPM images. F: cross-sectional CPM image.

The CPM device only requires three optical elements, an objective lens, polarising beam splitter and tube lens. The simple optics could make the device cost significantly lower and the device structure simpler than those of more sophisticated *in vivo* microscopy approaches. While an off-the-shelf objective lens was used in the current CPM device, a custom, miniature objective lens using freeform lens surfaces can be developed to reduce the lens size and cost.²² The custom miniature objective lens can be used in conjunction with a smartphone camera to collect CPM images. The voice coil motor of the smartphone camera can conduct axial scanning of the focal plane, which opens the possibility of building a compact, smartphone-based CPM device.

Developing a dual-functional device that utilises a polarising and nonpolarising beam splitter may also be another area of interest. Current dermatoscopy techniques have adapted to using both nonpolarised and polarised dermatoscopes. Nonpolarised dermatoscopes are beneficial in visualising superficial features of the skin. Polarised dermatoscopes are better suited for examining deeper structures.²³

One critical limitation of this pilot study was the lack of wide-field imaging capability registered with CPM imaging. The CPM field of view was small, $740\ \mu\text{m} \times 560\ \mu\text{m}$, and

could not visualise the entire lesion. The large diameter of the objective lens (25 mm) made it challenging to place the CPM device at exact target locations identified by naked eye or dermatoscopy. In the future, we will integrate an additional miniature camera that images through the same objective lens as CPM but with a significantly smaller NA and larger field to acquire wide-field dermatoscopy images spatially registered with CPM images, similarly to previous work on integrating dermatoscopy as part of an RCM device.²⁴

Additional microscopic objects were observable other than melanocytic cells and capillaries. For example, a white object was noticed at the centre of Figure 7C, D and F. This could be due to light scattering from a small air bubble trapped between the skin fold and indexing matching gel. Dark blueish objects were noticed in the left-top quadrant of Figure 7E. These could be cells with higher melanin density, but further investigation is needed. A future study of imaging skin lesions to be biopsied and comparing CPM images with corresponding histopathologic images would shed more light on which cellular structure these objects represent.

The CPM device uses the absorption contrast and therefore cannot image nonpigmented cells. Other imaging modalities such as RCM can be combined with CPM

to visualise both pigmented and nonpigmented cells. Recently, low-cost RCM devices have been developed.^{16,25} Both CPM and low-cost RCM devices use consumer-grade CMOS sensors, which can facilitate the integration of the two imaging modalities into a single device. The combined CPM-RCM device could be used to image large areas of the skin lesion either via video mosaicking methods²⁶ or step-and-image methods as conducted in the standard RCM device (Vivascope 1500).²⁷ The CPM-RCM device could be used to image skin lesions with Langerhans cells to evaluate its utility for distinguishing between Langerhans cells and melanocytic cells. In the future, we will develop improved CPM devices with the wide-field imaging capability and/or RCM modality, and evaluate the CPM devices for various clinical and research applications.

ACKNOWLEDGEMENTS

This research was supported by the Asset Development fund provided by the University of Arizona's Tech Launch Arizona.

CONFLICT OF INTEREST STATEMENT

JZ, CC and DK are inventors of the patent application on the CPM technology presented in this paper. The University of Arizona has a technology-licensing agreement with ArgosMD on the portable confocal microscopy technology. DK has the rights to receive royalties as a result of this licensing agreement. DK serves as a scientific advisor to ArgosMD. Conflicts of interest resulting from this interest are being managed by the University of Arizona in accordance with its policies.

ORCID

Manu Jain  <https://orcid.org/0000-0002-6035-0825>

Dongkyun Kang  <https://orcid.org/0000-0001-5063-5387>

REFERENCES

- Wu, X., Marchetti, M. A., & Marghoob, A. A. (2015). Dermoscopy: Not just for dermatologists. *Melanoma Management*, 2, 63–73.
- Wolner, Z. J., Yélamos, O., Liopyris, K., Rogers, T., Marchetti, M. A., & Marghoob, A. A. (2017). Enhancing skin cancer diagnosis with dermoscopy. *Dermatologic Clinics*, 35, 417–437.
- Yélamos, O., Braun, R. P., Liopyris, K., Wolner, Z. J., Kerl, K., Gerami, P., & Marghoob, A. A. (2019). Usefulness of dermoscopy to improve the clinical and histopathologic diagnosis of skin cancers. *Journal of the American Academy of Dermatology*, 80, 365–377.
- Rajadhyaksha, M., Grossman, M., Esterowitz, D., Webb, R. H., & Anderson, R. R. (1995). In vivo confocal scanning laser microscopy of human skin: Melanin provides strong contrast. *Journal of Investigative Dermatology*, 104, 946–952.
- Rajadhyaksha, M., Marghoob, A., Rossi, A., Halpern, A. C., & Nehal, K. S. (2017). Reflectance confocal microscopy of skin in vivo: From bench to bedside. *Lasers in Surgery and Medicine*, 49, 7–19.
- Hashemi, P., Pulitzer, M. P., Scope, A., Kovalyshyn, I., Halpern, A. C., & Marghoob, A. A. (2012). Langerhans cells and melanocytes share similar morphologic features under in vivo reflectance confocal microscopy: A challenge for melanoma diagnosis. *Journal of the American Academy of Dermatology*, 66, 452–462.
- Farabi, B., Rao, B. K., & Jain, M. (2023). Identifying pitfalls for diagnosing pigmented bowen disease on reflectance confocal microscopy: Misleading dendritic cells. *Dermatology Practical & Conceptual*, 13, e2023030.
- Dubois, A., Levecq, O., Azimani, H., Siret, D., Barut, A., Suppa, M., Del Marmol, V., Malveyh, J., Cinotti, E., Rubegni, P., & Perrot, J. L. (2018). Line-field confocal optical coherence tomography for high-resolution noninvasive imaging of skin tumors. *Journal of Biomedical Optics*, 23, 1–9.
- Tsai, M. R., Ho, T. S., Wu, Y. H., & Lu, C. W. (2021). In vivo dual-mode full-field optical coherence tomography for differentiation of types of melanocytic nevi. *Journal of Biomedical Optics*, 26, 020501.
- Balu, M., Mazhar, A., Hayakawa, C. K., Mittal, R., Krasieva, T. B., Konig, K., Venugopalan, V., & Tromberg, B. J. (2013). In vivo multiphoton NADH fluorescence reveals depth-dependent keratinocyte metabolism in human skin. *Biophysical Journal*, 104, 258–267.
- Krasieva, T. B., Stringari, C., Liu, F., Sun, C. H., Kong, Y., Balu, M., Meyskens, F. L., Gratton, E., & Tromberg, B. J. (2013). Two-photon excited fluorescence lifetime imaging and spectroscopy of melanins in vitro and in vivo. *Journal of Biomedical Optics*, 18, 31107.
- Masters, B. R., So, P. T., Buehler, C., Barry, N., Sutin, J. D., Mantulin, W. W., & Gratton, E. (2004). Mitigating thermal mechanical damage potential during two-photon dermal imaging. *Journal of Biomedical Optics*, 9, 1265–1270.
- Kono, T., & Yamada, J. (2019). In vivo measurement of optical properties of human skin for 450–800 nm and 950–1600 nm wavelengths. *International Journal of Thermophysics*, 40, 51.
- Treu, C. M., Lupi, O., Bottino, D. A., & Bouskela, E. (2011). Sidestream dark field imaging: The evolution of real-time visualization of cutaneous microcirculation and its potential application in dermatology. *Archives of Dermatological Research*, 303, 69–78.
- Tearney, G. J., Brezinski, M. E., Southern, J. F., Bouma, B. E., Hee, M. R., & Fujimoto, J. G. (1995). Determination of the refractive index of highly scattering human tissue by optical coherence tomography. *Optics Letters*, 20, 2258.
- Gong, C., Stratton, D. B., Curiel-Lewandrowski, C. N., & Kang, D. (2020). Speckle-free, near-infrared portable confocal microscope. *Applied Optics*, 59, G41–G46.
- Kirshner, H., Aguet, F., Sage, D., & Unser, M. (2013). 3-D PSF fitting for fluorescence microscopy: Implementation and localization application. *Journal of Microscopy*, 249, 13–25.
- Griffa, A., Garin, N., & Sage, D. (2010). Comparison of deconvolution software in 3D microscopy: A user point of view—Part 1. *Imaging & Microscopy*, 12, 43–45.
- Guitera, P., Pellacani, G., Longo, C., Seidenari, S., Avramidis, M., & Menzies, S. W. (2009). In vivo reflectance confocal microscopy

- enhances secondary evaluation of melanocytic lesions. *Journal of Investigative Dermatology*, 129, 131–138.
20. Stevenson, A. D., Mickan, S., Mallett, S., & Ayya, M. (2013). Systematic review of diagnostic accuracy of reflectance confocal microscopy for melanoma diagnosis in patients with clinically equivocal skin lesions. *Dermatology Practical and Conceptual*, 3, 19–27.
 21. Halasinski, P., Lubarska, M., Lubarski, K., & Jalowska, M. (2023). Lasers' Q-switched treatment in skin and subcutaneous lesions – Review. *Postepy Dermatologii Alergologii*, 40, 181–186.
 22. Kang, D., Carruth, R. W., Kim, M., Schlachter, S. C., Shishkov, M., Woods, K., Tabatabaei, N., Wu, T., & Tearney, G. J. (2013). Endoscopic probe optics for spectrally encoded confocal microscopy. *Biomedical Optics Express*, 4, 1925–1936.
 23. Pan, Y., Gareau, D. S., Scope, A., Rajadhyaksha, M., Mullani, N. A., & Marghoob, A. A. (2008). Polarized and nonpolarized dermoscopy: The explanation for the observed differences. *Archives of Dermatology*, 144, 828–829.
 24. Dickensheets, D. L., Kreitinger, S., Peterson, G., Heger, M., & Rajadhyaksha, M. (2017). Wide-field imaging combined with confocal microscopy using a miniature f/5 camera integrated within a high NA objective lens. *Optics Letters*, 42, 1241–1244.
 25. Freeman, E. E., Semeere, A., Osman, H., Peterson, G., Rajadhyaksha, M., Gonzalez, S., Martin, J. N., Anderson, R. R., Tearney, G. J., & Kang, D. (2018). Smartphone confocal microscopy for imaging cellular structures in human skin in vivo. *Biomedical Optics Express*, 9, 1906–1915.
 26. Kose, K., Cordova, M., Duffy, M., Flores, E. S., Brooks, D. H., & Rajadhyaksha, M. (2014). Video-mosaicing of reflectance confocal images for examination of extended areas of skin in vivo. *British Journal of Dermatology*, 171, 1239–1241.
 27. Hofmann-Wellenhof, R., Hofmann-Wellenhof, R., Pellacani, G., Malvehy, J., Soyer, H. P., & SpringerLink (2012). *Reflectance confocal microscopy for skin diseases*. Springer Berlin Heidelberg: Imprint: Springer.

How to cite this article: Romero, R., Zhao, J., Stratton, D., Marcelino, K., Sugimura, M., Nichols, A., Gonzalez, S., Jain, M., Curiel-Lewandrowski, C., & Kang, D. (2023). Handheld cross-polarised microscope for imaging individual pigmented cells in human skin in vivo. *Journal of Microscopy*, 292, 47–55. <https://doi.org/10.1111/jmi.13225>

REFERENCES

- [1] National Cancer Institute. *Cancer Stat Facts: Anal Cancer*. Accessed on 26 March 2024. 2023. URL: <https://seer.cancer.gov/statfacts/html/anus.html>.
- [2] C. Lin, S. Franceschi, and G.M. Clifford. “Human papillomavirus types from infection to cancer in the anus, according to sex and HIV status: A systematic review and meta-analysis”. In: *Lancet Infectious Diseases* 18 (2018), pp. 198–206. DOI: 10.1016/S1473-3099(17)30653-9.
- [3] D. A. Machalek et al. “Anal human papillomavirus infection and associated neoplastic lesions in men who have sex with men: A systematic review and meta-analysis”. In: *Lancet Oncology* 13 (2012), pp. 487–500. DOI: 10.1016/S1470-2045(12)70080-3.
- [4] A.E. Grulich et al. “Incidence of cancers in people with HIV/AIDS compared with immunosuppressed transplant recipients: A meta-analysis”. In: *Lancet* 370 (2007), pp. 59–67. DOI: 10.1016/S0140-6736(07)61050-2.
- [5] T.A. Gondal et al. “Anal Cancer: The Past, Present and Future”. In: *Curr Oncol* 30.3 (2023), pp. 3232–3250. DOI: 10.3390/curroncol30030246.
- [6] M.J. Silverberg et al. “Risk of anal cancer in HIV-infected and HIV-uninfected individuals in North America”. In: *Clin Infect Dis* 54.7 (2012), pp. 1026–1034. DOI: 10.1093/cid/cir1014.

- [7] J.M. Palefsky et al. “Treatment of anal high-grade squamous intraepithelial lesions to prevent anal cancer”. In: *New England Journal of Medicine* 386.24 (2022), pp. 2273–2282.
- [8] T. Cuming and M. Nathan. “Anal cancer screening: Techniques and guidelines”. In: *Seminars in Colon and Rectal Surgery* 28.2 (2017), pp. 69–74. ISSN: 1043-1489. DOI: 10.1053/j.scrs.2017.04.003. URL: <https://doi.org/10.1053/j.scrs.2017.04.003>.
- [9] C.E. Pineda et al. “High-Resolution Anoscopy Targeted Surgical Destruction of Anal High-Grade Squamous Intraepithelial Lesions: A Ten-Year Experience”. In: *Diseases of the Colon & Rectum* 51.6 (2008), pp. 829–837. DOI: 10.1007/s10350-008-9233-4.
- [10] L. F. Barroso et al. “Anal Cancer Screening and Prevention: Summary of Evidence Reviewed for the 2021 Centers for Disease Control and Prevention Sexually Transmitted Infection Guidelines”. In: *Clinical Infectious Diseases* 74.Issue Supplement₂ (2022), S179–S192. DOI: 10.1093/cid/ciac044. URL: <https://doi.org/10.1093/cid/ciac044>.
- [11] W.A. Wells et al. “In Vivo and Ex Vivo Microscopy: Moving Toward the Integration of Optical Imaging Technologies Into Pathology Practice”. In: *Arch Pathol Lab Med* 143.3 (2019), pp. 288–298. DOI: 10.5858/arpa.2018-0298-RA.
- [12] M. Tavakoli, P. Hossain, and R.A. Malik. “Clinical applications of corneal confocal microscopy”. In: *Clin Ophthalmol* 2.2 (2008), pp. 435–445. DOI: 10.2147/opth.s1490.
- [13] S. González et al. “Changing paradigms in dermatology: confocal microscopy in clinical and surgical dermatology”. In: *Clinics in Dermatology* 21 (5 2003), pp. 359–369. ISSN: 0738-081X. DOI: 10.1016/j.clindermatol.2003.08.007.

- [14] R. Kiesslich et al. “Confocal laser endomicroscopy”. In: *Gastrointest Endosc Clin N Am* 15.4 (2005), pp. 715–731. DOI: 10.1016/j.giec.2005.08.010.
- [15] J. Ding et al. “Optical coherence tomography for the early detection of colorectal dysplasia and cancer: validation in a murine model”. In: *Quant Imaging Med Surg* 11.1 (2021), pp. 371–379. DOI: 10.21037/qims-20-13.
- [16] W. Drexler and J. Fujimoto. “State-of-the-art retinal optical coherence tomography”. In: *Progress in Retinal and Eye Research* 27 (2008), pp. 45–88. DOI: 10.1016/j.preteyeres.2007.07.005.
- [17] E. Cinotti et al. “Quantification of capillary blood cell flow using reflectance confocal microscopy”. In: *Skin Research and Technology* 20.3 (2014), pp. 373–378. DOI: 10.1111/srt.12128.
- [18] L. E. Meyer et al. “In vivo confocal scanning laser microscopy: comparison of the reflectance and fluorescence mode by imaging human skin”. In: *Journal of Biomedical Optics* 11.4 (2006), pp. 1–7. DOI: 10.1117/1.2337294.
- [19] G. Peterson et al. “Feasibility of a Video-Mosaicking Approach to Extend the Field-of-View For Reflectance Confocal Microscopy in the Oral Cavity In Vivo”. In: *Lasers in Surgery and Medicine* 51.5 (2019), pp. 439–451. DOI: 10.1002/lsm.23090.
- [20] J. Welzel. “Optical coherence tomography in dermatology: a review”. In: *Skin Research and Technology* 7.1 (2001), pp. 1–9. DOI: 10.1034/j.1600-0846.2001.007001001.x.
- [21] R. A. Leitgeb. “En face optical coherence tomography: a technology review [Invited]”. In: *Biomedical Optics Express* 10.5 (2019), pp. 2177–2201.

- [22] L. Liu et al. “Imaging the subcellular structure of human coronary atherosclerosis using micro-optical coherence tomography”. In: *Nature Medicine* 17.8 (2011), pp. 1010–1014.
- [23] A. Dubois et al. “Line-field confocal optical coherence tomography for high-resolution noninvasive imaging of skin tumors”. In: *Journal of Biomedical Optics* 23.10 (2018), pp. 1–9.
- [24] R. M. Power and J. Huisken. “A guide to light-sheet fluorescence microscopy for multiscale imaging”. In: *Nature Methods* 14.4 (2017), pp. 360–373.
- [25] J. M. Girkin and M. T. Carvalho. “The light-sheet microscopy revolution”. In: *Journal of Optics* 20.5 (2018), p. 053002.
- [26] C. D. Nguyen et al. “Scattering-Based Light-Sheet Microscopy for Rapid Cellular Imaging of Fresh Tissue”. In: *Lasers in Surgery and Medicine* 53.6 (2021), pp. 872–879.
- [27] American Cancer Society. *If You Have Anal Cancer*. Accessed on 26 March 2024. 2020. URL: [https://www.cancer.org/cancer/types/anal-cancer/about/what-is-anal-cancer.html#:~:text=Most%20\(nearly%209%20out%20of,deeper%20layers%20of%20the%20lining..](https://www.cancer.org/cancer/types/anal-cancer/about/what-is-anal-cancer.html#:~:text=Most%20(nearly%209%20out%20of,deeper%20layers%20of%20the%20lining..)
- [28] Radiology Assistant. *Anal Cancer Staging by Maas, M. and Lambregts D*. Accessed on 26 March 2024. URL: <https://radiologyassistant.nl/abdomen/anal-cancer-2/anal>.
- [29] Massarat Zutshi, ed. *Anorectal Disease: Contemporary Management*. 1st ed. Springer Cham, 2016, pp. XVI, 314. ISBN: 978-3-319-23147-1. DOI: 10.1007/978-3-319-23147-1. URL: <https://doi.org/10.1007/978-3-319-23147-1>.

- [30] R.J. Hillman. *Digital anal rectal examination (DARE) for anal cancer prevention*. Accessed on 26 March 2024. 2020. URL: <https://www.hpvworld.com/articles/digital-anal-rectal-examination-dare-for-anal-cancer-prevention/>.
- [31] Jenny McCloskey. “Human Papillomavirus Infection of the Anal Canal and its Relation to Anal Disease”. In: 2012. URL: <https://api.semanticscholar.org/CorpusID:80416765>.
- [32] Alice M. Schofield et al. “A prospective study of anal cancer screening in HIV-positive and negative MSM”. In: *AIDS* 30.9 (2016), pp. 1375–1383. DOI: 10.1097/QAD.0000000000001045.
- [33] N Jay et al. “Colposcopic Characteristics and Lugol’s Staining Differentiate Anal High-Grade and Low-Grade Squamous Intraepithelial Lesions During High Resolution Anoscopy”. In: *Papillomavirus Research* 1 (2015). Epub 2015 Jul 3, pp. 101–108. DOI: 10.1016/j.pvr.2015.06.004.
- [34] JY Zheng et al. “Presence of pink-color sign within 1 min after iodine staining has high diagnostic accordance rate for esophageal high-grade intraepithelial neoplasia/invasive cancer”. In: *Saudi Journal of Gastroenterology* 25.2 (2019), pp. 113–118. DOI: 10.4103/sjg.SJG_274_18.
- [35] Cleveland Clinic. *Anoscopy*. Accessed on 26 March 2024. URL: <https://my.clevelandclinic.org/health/treatments/24993-anoscopy>.
- [36] W. C. Warger, C. A. Di Marzio, and M. Rajyadhaksha. “Confocal Microscopy”. In: *Handbook of Biomedical Optics*. Ed. by D. A. Boas, C. Pitris, and N. Ramanujam. Taylor & Francis Group, 2011, pp. 517–542.

- [37] T Collier et al. “Real-time reflectance confocal microscopy: comparison of two-dimensional images and three-dimensional image stacks for detection of cervical precancer”. In: *Journal of biomedical optics* 12.2 (2007), pp. 024021–7.
- [38] F Sheikhzadeh et al. “Quantification of confocal fluorescence microscopy for the detection of cervical intraepithelial neoplasia”. In: *Biomedical engineering online* 14.1 (2015), p. 96.
- [39] Kwan-Bin Sung et al. “Fiber optic confocal reflectance microscopy: a new real-time technique to view nuclear morphology in cervical squamous epithelium in vivo”. In: *Optics Express* 11.24 (2003), p. 3171.
- [40] NKT Photonics. *Optical Coherence Tomography, OCT*. Accessed on 26 March 2024. URL: <https://www.nktphotonics.com/applications/bio-imaging-and-microscopy/optical-coherence-tomography-oct/>.
- [41] JF Bille, ed. *High Resolution Imaging in Microscopy and Ophthalmology: New Frontiers in Biomedical Optics*. Cham, Switzerland: Springer, 2019. URL: <https://link.springer.com/book/10.1007/978-3-030-16638-0>.
- [42] Biwei Yin et al. “Extended depth of focus for coherence-based cellular imaging”. In: *Optica* 4 (2017), pp. 959–965.
- [43] A. Dubois et al. “Line-field confocal optical coherence tomography for high-resolution noninvasive imaging of skin tumors”. In: *J Biomed Opt* 23.10 (2018), pp. 1–9. DOI: 10.1117/1.JBO.23.10.106007.

- [44] B. Yin, Z. Piao, K. Nishimiya, et al. “3D cellular-resolution imaging in arteries using few-mode interferometry”. In: *Light: Science & Applications* 8 (2019), p. 104. DOI: 10.1038/s41377-019-0211-5. URL: <https://doi.org/10.1038/s41377-019-0211-5>.
- [45] H. Jia, F. Abtahian, A. Aguirre, et al. “In Vivo Diagnosis of Plaque Erosion and Calcified Nodule in Patients With Acute Coronary Syndrome by Intravascular Optical Coherence Tomography”. In: *Journal of the American College of Cardiology* 62.19 (2013), pp. 1748–1758. DOI: 10.1016/j.jacc.2013.05.071. URL: <https://doi.org/10.1016/j.jacc.2013.05.071>.
- [46] V. X. D. Yang et al. “High speed, wide velocity dynamic range Doppler optical coherence tomography (Part III): in vivo endoscopic imaging of blood flow in the rat and human gastrointestinal tracts”. In: *Optics Express* 11.19 (2003), pp. 2416–2424. URL: <https://www.opticsexpress.org/abstract.cfm?URI=oe-11-19-2416>.
- [47] Brett Bouma et al. “High-resolution imaging of the human esophagus and stomach in vivo using optical coherence tomography”. In: *Gastrointestinal Endoscopy* 51 (2000), pp. 467–474. DOI: 10.1016/S0016-5107(00)70449-4.
- [48] M. V. Jr Sivak et al. “High-resolution endoscopic imaging of the GI tract using optical coherence tomography”. In: *Gastrointestinal Endoscopy* 51.4 (2000), pp. 474–479. DOI: 10.1016/S0016-5107(00)70450-0.
- [49] M. Tsuboi et al. “Optical coherence tomography in the diagnosis of bronchial lesions”. In: *Lung Cancer* 49.3 (2005), pp. 387–394. DOI: 10.1016/j.lungcan.2005.04.007.

- [50] M. T. Bus et al. “Volumetric in vivo visualization of upper urinary tract tumors using optical coherence tomography: a pilot study”. In: *Journal of Urology* 190.6 (2013), pp. 2236–2242. DOI: 10.1016/j.juro.2013.06.017.
- [51] Z. Wang et al. “In vivo bladder imaging with microelectromechanical-systems-based endoscopic spectral domain optical coherence tomography”. In: *Journal of Biomedical Optics* 12.3 (2007), p. 034009. DOI: 10.1117/1.2750294.
- [52] A. M. Sergeev et al. “In vivo endoscopic OCT imaging of precancer and cancer states of human mucosa”. In: *Optics Express* 1 (1997), pp. 432–440.
- [53] C. Ren, X. Zeng, Z. Shi, et al. “Multi-center clinical study using optical coherence tomography for evaluation of cervical lesions in-vivo”. In: *Scientific Reports* 11 (2021), p. 7507. DOI: 10.1038/s41598-021-86711-3. URL: <https://doi.org/10.1038/s41598-021-86711-3>.
- [54] J.K.S. Gallwas et al. “Optical coherence tomography for the diagnosis of cervical intraepithelial neoplasia”. In: *Lasers in Surgery and Medicine* 43 (2011), pp. 206–212. DOI: 10.1002/lsm.21030. URL: <https://doi.org/10.1002/lsm.21030>.
- [55] Yutao Ma et al. “Computer-Aided Diagnosis of Label-Free 3-D Optical Coherence Microscopy Images of Human Cervical Tissue”. In: *IEEE Transactions on Biomedical Engineering* 66.9 (2019), pp. 2447–2456. DOI: 10.1109/TBME.2018.2890167.
- [56] H. Siedentopf and R. Zsigmondy. “Über Sichtbarmachung und Größenbestimmung ultramikroskopischer Teilchen, mit besonderer Anwendung auf Goldrubingläser”. In: *Annalen der Physik* 315 (1902), pp. 1–39.

- [57] A. H. Voie, D. H. Burns, and F. A. Spelman. “Orthogonal-plane fluorescence optical sectioning: three dimensional imaging of macroscopic biological specimens”. In: *Journal of Microscopy* 170 (1993), pp. 229–236.
- [58] J. Huisken et al. “Optical sectioning deep inside live embryos by selective plane illumination microscopy”. In: *Science* 305 (2004), pp. 1007–1009.
- [59] P. A. Santi. “Light Sheet Fluorescence Microscopy: A Review”. In: *Journal of Histochemistry & Cytochemistry* 59.2 (2011), pp. 129–138. DOI: 10.1369/0022155410394857.
- [60] E. G. Reynaud and P. Tomancak. “Meeting report: First light sheet based fluorescence microscopy workshop”. In: *Biotechnology Journal* 5 (2010), pp. 798–804.
- [61] Strobl F. Chang B. J. et al. Stelzer E. H. K. “Light sheet fluorescence microscopy”. In: *Nature Reviews Methods Primers* 1 (2021), p. 73. DOI: 10.1038/s43586-021-00069-4. URL: <https://doi.org/10.1038/s43586-021-00069-4>.
- [62] S. Wolf, W. Supatto, G. Debrégeas, et al. “Whole-brain functional imaging with two-photon light-sheet microscopy”. In: *Nature Methods* 12 (2015), pp. 379–380. DOI: 10.1038/nmeth.3371. URL: <https://doi.org/10.1038/nmeth.3371>.
- [63] Vincent Maioli et al. “Fast in vivo multiphoton light-sheet microscopy with optimal pulse frequency”. In: *Biomedical Optics Express* 11 (2020), pp. 6012–6026.
- [64] Niall Hanrahan et al. “Second Harmonic Generation Light Sheet Microscopy (SHG-LSM): A new tool for label-free 3D bioimaging”. In: Oct. 2020, p. 17. DOI: 10.1117/12.2585210.

- [65] Ishan Barman, Khay Ming Tan, and Gajendra Pratap Singh. “Optical sectioning using single-plane-illumination Raman imaging”. In: *Journal of Raman Spectroscopy* 41.10 (2010), pp. 1099–1101.
- [66] Yusuke Oshima et al. “Light sheet-excited spontaneous Raman imaging of a living fish by optical sectioning in a wide field Raman microscope”. In: *Optics Express* 20.15 (2012), pp. 16195–16204.
- [67] Z. Yang et al. “Light sheet tomography (LST) for in situ imaging of plant roots”. In: *Optics Express* 21 (2013), pp. 16239–16247. DOI: 10.1364/OE.21.016239.
- [68] D. Di Battista et al. “Enhanced Light Sheet Elastic Scattering Microscopy by Using a Supercontinuum Laser”. In: *Methods and Protocols* 2.3 (2019).
- [69] Sandro Heuke et al. “Spatial frequency modulated imaging in coherent anti-Stokes Raman microscopy”. In: *Optica* 7 (2020), pp. 417–424.
- [70] Paul Ebersbach et al. “Chemical fingerprinting of single glandular trichomes of *Cannabis sativa* by Coherent anti-Stokes Raman scattering (CARS) microscopy”. In: *BMC Plant Biology* 18 (Nov. 2018). DOI: 10.1186/s12870-018-1481-4.
- [71] M. Lin et al. “Light-sheet-based 2D light scattering cytometry for label-free characterization of senescent cells”. In: *Biomedical Optics Express* 7.12 (2016), pp. 5170–5181.
- [72] Omar E. Olarte et al. “Light-sheet microscopy: a tutorial”. In: *Advances in Optics and Photonics* 10 (2018), pp. 111–179.

- [73] A.K. Glaser, K.W. Bishop, L.A. Barner, et al. “A hybrid open-top light-sheet microscope for versatile multi-scale imaging of cleared tissues”. In: *Nature Methods* 19 (2022), pp. 613–619. DOI: 10.1038/s41592-022-01468-5.
- [74] M. Bouchard, V. Voleti, C. Mendes, et al. “Swept confocally-aligned planar excitation (SCAPE) microscopy for high-speed volumetric imaging of behaving organisms”. In: *Nature Photonics* 9 (2015), pp. 113–119. DOI: 10.1038/nphoton.2014.323.
- [75] Firebird Optics. *All About Cylindrical Lenses*. Accessed on 26 March 2024. 2023. URL: <https://www.firebirdoptics.com/blog/all-about-cylindrical-lenses>.
- [76] P. J. Keller and E. H. Stelzer. “Quantitative in vivo imaging of entire embryos with digital scanned laser light sheet fluorescence microscopy”. In: *Current Opinion in Neurobiology* 18 (2008), pp. 624–632.
- [77] Jerome Mertz and Jinhyun Kim. “Scanning light-sheet microscopy in the whole mouse brain with HiLo background rejection”. In: *Journal of Biomedical Optics* 15.1 (2010), p. 016027. DOI: 10.1117/1.3324890. URL: <https://doi.org/10.1117/1.3324890>.
- [78] S. Takanezawa, T. Saitou, and T. Imamura. “Wide field light-sheet microscopy with lens-axicon controlled two-photon Bessel beam illumination”. In: *Nature Communications* 12 (2021), p. 2979. DOI: 10.1038/s41467-021-23249-y.
- [79] The University of Western Australia Optical Biomedical Engineering Laboratory. *Beam Shaping*. Accessed on 26 March 2024. URL: <https://obel.ee.uwa.edu.au/research/techniques/beam-shaping/>.

- [80] Panu Hildén and Andriy Shevchenko. “Extended depth of field of an imaging system with an annular aperture”. In: *Optics Express* 31 (2023), pp. 11102–11115. DOI: 10.1364/OE.484290. URL: <https://doi.org/10.1364/OE.484290>.
- [81] M Kruczkowski et al. “Predictions of cervical cancer identification by photonic method combined with machine learning”. In: *Sci Rep* 12.1 (2022), p. 3762. DOI: 10.1038/s41598-022-07723-1.
- [82] Ryan McGorty, Dan Xie, and Bo Huang. “High-NA open-top selective-plane illumination microscopy for biological imaging”. In: *Opt. Express* 25 (2017), pp. 17798–17810.
- [83] D.J. Lockwood. In: *Encyclopedia of Color Science and Technology*. Ed. by M.R. Luo. New York, NY: Springer, 2016. Chap. Rayleigh and Mie Scattering. DOI: 10.1007/978-1-4419-8071-7_218.
- [84] Hyper Physics. Accessed on 26 March 2024. URL: <http://hyperphysics.phy-astr.gsu.edu/hbase/atmos/blusky.html>.
- [85] S. L. Jacques. “Optical properties of biological tissues: a review”. In: *Phys. Med. Biol.* 58.11 (2013), R37–R61.
- [86] Niklas Rottmayer, Claudia Redenbach, and Florian O. Fahrbach. “Efficient stripe artefact removal by a variational method: application to light-sheet microscopy, FIB-SEM and remote sensing images”. In: *bioRxiv* (2024). Preprint. DOI: 10.1101/2024.02.02.578531.

- [87] K. Greger, J. Swoger, and E. H. K. Stelzer. “Basic building units and properties of a fluorescence single plane illumination microscope”. In: *Rev. Sci. Instrum.* 78 (2007), p. 023705.
- [88] P. Ricci et al. “Removing striping artifacts in light-sheet fluorescence microscopy: a review”. In: *Prog Biophys Mol Biol* 168 (2022). Epub 2021 Jul 15, pp. 52–65. DOI: 10.1016/j.pbiomolbio.2021.07.003.
- [89] O. E. Olarte et al. “Image formation by linear and nonlinear digital scanned light-sheet fluorescence microscopy with Gaussian and Bessel beam profiles”. In: *Biomed. Opt. Express* 3 (2012), pp. 1492–1505.
- [90] M.A. Taylor et al. “Diffuse lightsheet microscopy for stripe-free calcium imaging of neural populations”. In: *J. Biophot.* 11 (2018), pp. 1–9. DOI: 10.1002/jbio.201800088.
- [91] J. Huisken and D. Y. R. Stainier. “Even fluorescence excitation by multidirectional selective plane illumination microscopy (mSPIM)”. In: *Opt. Lett.* 32 (2007), pp. 2608–2610.
- [92] C Gong et al. “Speckle-free, near-infrared portable confocal microscope”. In: *Appl Opt* 59.22 (2020), G41–G46. DOI: 10.1364/AO.392004.
- [93] O Liba, M Lew, E SoRelle, et al. “Speckle-modulating optical coherence tomography in living mice and humans”. In: *Nat Commun* 8 (2017), p. 15845. DOI: 10.1038/ncomms15845.
- [94] D. Di Battista et al. “Enhanced Light Sheet Elastic Scattering Microscopy by Using a Supercontinuum Laser”. In: *Methods and Protocols* 2 (2019), p. 57. DOI: 10.3390/mps2030057. URL: <https://doi.org/10.3390/mps2030057>.

- [95] Wikipedia. *Speckle (interference)*. Accessed on 26 March 2024. URL: [https://en.wikipedia.org/wiki/Speckle_\(interference\)](https://en.wikipedia.org/wiki/Speckle_(interference)).
- [96] Joseph W. Goodman. *Speckle Phenomena in Optics: Theory and Applications, Second Edition*. 2020. ISBN: 9781510631489. DOI: 10.1117/3.2548484. URL: <https://doi.org/10.1117/3.2548484>.
- [97] B Redding, M A Choma, and H Cao. “Speckle-free laser imaging using random laser illumination”. In: *Nat. Photonics* 6.6 (2012), pp. 355–359.
- [98] D S Mehta et al. “Laser speckle reduction by multimode optical fiber bundle with combined temporal, spatial, and angular diversity”. In: *Appl. Opt.* 51.12 (2012), pp. 1894–1904.
- [99] S An et al. “Speckle suppression in laser display using several partially coherent beams”. In: *Opt. Express* 17.1 (2009), pp. 92–103.
- [100] Sintec Optronics. *Laser Speckle Reducer*. Accessed on 26 March 2024. URL: <https://www.sintec.sg/optics/524.html>.
- [101] T-T-K Tran et al. “Speckle reduction in laser projection displays through angle and wavelength diversity”. In: *Appl. Opt.* 55.6 (2016), pp. 1267–1274.
- [102] Y. Fujimaki and H. Taniguchi. “Reduction of speckle contrast in multimode fibers using piezoelectric vibrator”. In: *Proc. SPIE*. Vol. 8960. SPIE. 2014, 89601S.
- [103] K. S. Nehal, D. Gareau, and M. Rajadhyaksha. “Skin imaging with reflectance confocal microscopy”. In: *Seminars in Cutaneous Medicine and Surgery* 27.1 (2008), pp. 37–43.

- [104] Y. Wang et al. “Optimal wavelength for ultrahigh-resolution optical coherence tomography”. In: *Opt. Express* 11.12 (2003), pp. 1411–1417.
- [105] Y. Zhang and H. Gross. “Systematic design of microscope objectives. Part I: System review and analysis”. In: *Adv. Opt. Technol.* 8.5 (2019), pp. 313–347.
- [106] Jingwei Zhao et al. “Investigation of different wavelengths for scattering-based light sheet microscopy”. In: *Biomedical Optics Express* 13 (2022), pp. 3882–3892. DOI: 10.1364/BOE.459823. URL: <https://doi.org/10.1364/BOE.459823>.
- [107] Richard Cole, Tushare Jinadasa, and Claire Brown. “Measuring and interpreting point spread functions to determine confocal microscope resolution and ensure quality control”. In: *Nature protocols* 6 (Nov. 2011), pp. 1929–41. DOI: 10.1038/nprot.2011.407.
- [108] Ali Shahin, Wesam Bachir, and Moustafa El-Daher. “Optical investigation of bovine grey and white matters in visible and near-infrared ranges”. In: *Polish Journal of Medical Physics And Engineering* 27 (Mar. 2021), p. 8. DOI: 10.2478/pjmpe-2021-0012.
- [109] M Srinivasan, D Sedmak, and S Jewell. “Effect of fixatives and tissue processing on the content and integrity of nucleic acids”. In: *American Journal of Pathology* 161.6 (2002), pp. 1961–1971. DOI: 10.1016/S0002-9440(10)64472-0.
- [110] M Abe et al. “The changes in crosslink contents in tissue after formalin fixation”. In: *Analytical Biochemistry* 318.1 (2003), pp. 118–123. DOI: 10.1016/S0003-2697(03)00194-5.
- [111] Brooke Liang et al. “Scattering-Based Light Sheet Microscopy Imaging of HPV-Associated Squamous Lesions of the Anal Canal: A Proof-of-Principle Study”. In:

- Modern Pathology* (2024), p. 100493. ISSN: 0893-3952. DOI: 10.1016/j.modpat.2024.100493. URL: <https://doi.org/10.1016/j.modpat.2024.100493>.
- [112] J. Zhao et al. “Speckle and Shadow Artifacts Reduction in Scattering-Based Light Sheet Microscopy”. In: *Biophotonics Congress: Optics in the Life Sciences 2023 (OMA, NTM, BODA, OMP, BRAIN), Technical Digest Series*. Optica Publishing Group. 2023, DTu2A.3.
- [113] B. Liang et al. *Scattering-Based Light Sheet Microscopy Imaging of Fresh Anoscopic Biopsy Specimens: A Prospective Descriptive Study Characterizing Anal Lesions*. International Anal Neoplasia Society 2023 Scientific Meeting. 2023.
- [114] Kripa B. Patel et al. “High-speed light-sheet microscopy for the in-situ acquisition of volumetric histological images of living tissue”. In: *Nature Biomedical Engineering* 6 (2022), pp. 569–583. DOI: 10.1038/s41551-022-00849-7. URL: <https://doi.org/10.1038/s41551-022-00849-7>.
- [115] C.J. Engelbrecht, F. Voigt, and F. Helmchen. “Miniaturized selective plane illumination microscopy for high-contrast in vivo fluorescence imaging”. In: *Optics Letters* 35.9 (2010), pp. 1413–1415. DOI: 10.1364/OL.35.001413.
- [116] Pablo Roldán-Varona et al. “Selective plane illumination optical endomicroscopy with polymer imaging fibers”. In: *APL Photonics* 8.1 (2023), p. 016103. DOI: 10.1063/5.0130486. URL: <https://doi.org/10.1063/5.0130486>.